POLITECNICO DI MILANO
Facolta di Ingegneria dei Sistemi
Dipartimento di Fisica

Tesi di Laurea in

Ingegneria Fisica

Systematic investigation into the influence of growth conditions on InAs/GaAs quantum dot densities and sizes for intermediate band solar cell application

Relatore
Prof. Giovanni Isella

Candidato
Stefano Vitelli

Matricola: 719607

Anno Accademico 2009/2010

To my lovely family
Virgilio, Graziella and Luca
to my friend Filippo P.
and to my darling Valeria

Abstract

The influence of the conditions during growth of InAs/GaAs quantum-dot structures on GaAs(001) by molecular-beam epitaxy was investigated systematically with respect to achieving high quantum dot densities, homogeneity and narrow sizes distribution. These are requirements for obtaining the necessary intermediate band in intermediate band solar cells. The growth temperature, InAs deposit, As flux, growth rate and III/V flux ratio were varied. Atomic force microscopy and a modular program for SPM data analysis were used to study the morphological properties of the QDs. The effect of several operations during image processing was analysed and a suitable routine was defined. The optimal temperature for the growth was found to be 480°C although 420°C was sufficient to induce 2D-3D transition. Varying the InAs thickness, a self-limiting size effect was detected at 2.2 ML, while increasing As-flux to 6x10^{-6} Torr led to big clasters formation. Finally, low growth rate (0.1-0.5 ML/s) was necessary to keep good homogeneity and the optimal III/V flux ratio was found to be in the range 1/10 - 1/5.

Sommario

La presente tesi si focalizza sullo studio di punti quantisti InAs/GaAs su substrato GaAs(001) per applicazioni su celle solari a banda intermedia. Un'alta densitá di punti quantistici, una buona omogeneitá e una distribuzione stretta di dimensioni laterali e altezze sono requisiti necessari per ottenere la banda intermedia in questa specifica applicazione. I campioni sono cresciuti per mezzo di epitassia da fasci molecolari, variando sistematicamente i parametri di crescita quali temperatura, quantitá di InAs depositato, flusso di As, velocitá di crescita e rapporto III/V di flussi. Lo scopo di questo studio é analizzare l'influenza di questi parametri su densitá, distribuzioni di dimensioni e omogeneitá dei punti quantistici.

I profili 3D della superficie dei campioni sono estratti tramite microscopia a forza atomica; successivamente le informazioni sono estrapolate dalle immagini per mezzo di uno specifico programma di analisi dopo aver valutato l'effetto di diverse correzioni durante l'image processing e dopo aver definito un'opportuna routine.

É stato dimostrato che la temperatura ottimale di crescita é 480°C, sebbene 420°C siano sufficienti per indurre la transizione 2D-3D. Variando lo spessore di InAs, a 2.2 ML é stato notato un effetto auto-limitante per quanto riguarda le dimensioni, mentre aumentando il flusso di As fino a 6x10^{-6} Torr si induce la coalescenza di piú punti quantistici. Infine, basse velocitá di crescita (0.1-0.5 ML/s) sono necessarie per mantenere una buona omogeneitá e il rapporto ottimale III/V é nell'intervallo 1/10-1/5.

Estratto in italiano

In questo studio viene analizzata l'influenza dei parametri di crescita epitassiale sulle proprietá morfologiche di punti quantistici InAs/GaAs cresciuti su substrato GaAs(001), per applicazioni su celle solari a banda intermedia (IBSC).

Nel capitolo 1, sono presentate le tre generazioni fotovoltaiche.
Alla prima generazione appartengono tutte le celle solari a singola giunzione basate sul silicio, sviluppate sulla base di strutture e processi relativamente semplici. Quando questa tecnologia é maturata, i costi del prodotto finito sono stati dominati dai costi delle materie prime (wafer di silicio e incapsulanti). Durante gli scorsi 20 anni si é assistito ad un cambiamento verso la seconda generazione o tecnologia dei film sottili. Questa tecnologia offre la possibilitá di ridurre i costi dei materiali eliminando il wafer di silicio, rendendo praticamente ogni semiconduttore sufficientemente economico. Inoltre, un altro vantaggio riguarda il fatto di poter aumentare l'unitá produttiva di 100 volte. Al momento 5 differenti tecnologie sono giunte allo stadio di sviluppo commerciale:

- Lega idrogenata di silicio amorfo
- Silicio policristallino
- Composti policristallini: calcopirati
- Diossido di titanio nanocristallino
- Tellurio di cadmio

Col passare del tempo, peró, i costi saranno progressivamente dominati da quelli dei materiali costituenti. Per poter progredire ulteriormente, l'efficienza di conversione dovrá essere aumentata sostanzialmente. Le performance delle celle solari potrebbero essere accresciute di 2-3 volte se fossero utilizzati differenti concetti per produrre la terza generazione. Per ora, quelli studiati sono:

- Celle tandem
- Generazione multipla di coppie e-h per fotone
- Celle *hot carriers*
- Celle con multibanda e impuritá
- Celle termofotovoltaiche e termofotoniche

Nel capitolo 2, viene presentata la fisica delle celle solari a banda intermedia (IBSC). Una IBSC é un'apparecchiatura fotovoltaica capace di superare l'efficienza limite di una cella solare a gap singola, sfruttando le proprietá elettriche e ottiche di un materiale a banda intermedia (IB). Questo tipo di materiale prende il nome dall'esistenza di una banda elettronica extra situata nel mezzo del bandgap. L'IB divide il bandgap in due intervalli di energia proibiti. Quando viene assorbita la luce in questa IB , oltra alla convenzionale transizione elettronica dalla banda di valenza (VB) alla banda di conduzione (CB), vi sono altre due transizioni possibili: dalla VB alla IB e dalla IB alla CB. Questo principio quindi, permette di utilizzare un maggiore spettro della radiazione solare per la conversione, assorbendo fotoni a frequenze che sarebbero perdute in una cella solare convenzionale.
Al momento ci sono tre differenti approcci per produrre una IBSC:

- Sintesi diretta di un materiale con IB
- L'approccio nanoporoso
- Implementazione per mezzo di punti quantistici (QD-IBSC)

Quest'ultima tecnica é stata utilizzata nel nostro studio.
Per poter capire come é possibile ottenere una IB, basti pensare alle proprietá quantistiche di questa nanostruttura. Essa presenta livelli energetici discreti simili a quelli di un atomo. Per questo motivo i punti quantistici sono anche chiamati *atomi artificiali*. Posizionando le nanostrutture in array 3D ordinati, le funzioni d'onda possono sovrapporsi e dare luogo ad uno splitting simile a quello che si ha nei cristalli costituiti da atomi convenzionali. Cosí facendo é possibile generare la banda intermedia richiesta per mezzo di questi superreticoli.
Esistono alcune considerazioni pratiche riguardo l'implementazione delle QD-IBSC:

- Il raggio delle nanostrutture dovrebbe essere dell'ordine dei 3.9 nm. In linea di principio tale dimensione potrebbe essere raggiungibile utilizzando il metodo di crescita Stranki-Krastanov per mezzo dell' MBE
- La densitá dei punti quantistici dovrebbe essere la piú elevata possibile
- Le nanostrutture dovrebbero essere le piú identiche possibili

É quindi importante riuscire a controllare queste caratteristiche delle nanostrutture.

Nel capitolo 3 si é provveduto a descrivere i principali processi fisici coinvolti durante la crescita di punti quantistici InAs/GaAs per mezzo di MBE secondo la tecnica Stanski-Krastanov (S-K). La descrizione segue le varie fasi del processo di formazione delle nanostrutture, dalla fase 2D fino alla copertura (*capping*).
Il metodo S-K é uno dei metodi piú usati per la formazione di punti quantistici sfruttando il mismatch reticolare di due semiconduttori ($a_{GaAs} < a_{InAs}$). Dopo aver raggiunto uno spessore critico di deposizione (fase 2D), l'energia di compressione accumulata dall'InAs viene rilassata creando spontaneamente isole 3D (transizione 2D-3D). L'eterostruttura cosí formata consiste di GaAs, uno strato iniziale 2D pseudomorfico di InAs chiamato *wetting layer* (WL) e di nanostrutture InAs. Successivamente, poiché i punti quantistici

per essere utilizzabili e protetti nell'IBSC devono essere integrati in una matrice, il processo epitassiale continua depositando ulteriore materiale (*capping*).
Il metodo S-K applicato a InAs/GaAs non segue, peró, precisamente questo schema ma ci sono caratteristiche che differiscono dalla crescita convenzionale, come, per esempio, le seguenti:

- Il WL 2D é un composto ternario InGaAs con una precisa composizione al momento della transizione
- La transizione 2D-3D avviene in un intervallo di 0.2 ML depositati di InAs, attraverso l'improvvisa nucleazione di $10^{10} - 10^{11}$ cm^{-2} punti quantistici coerenti
- I punti quantistici InAs includono anche del Ga nella loro base. Il quantitativo dipende dalle condizioni di crescita
- Il volume totale dei punti quantistici é altamente superiore alla quantitá di materiale depositato durante la loro formazione

Altri dettagli dell'eteroepitassia InAs/GaAs riguardano aspetti termodinamici e cinetici, come la segregazione superficiale di In, lo scambio In-Ga e l'erosione del WL.

Nel capitolo 4 sono presentati i dettagli sperimentali.
Numerosi campioni sono stati cresciuti in MBE, variando sistematicamente i parametri di crescita epitassiale quali temperatura, velocitá, flusso di As, spessore di InAs e rapporto III/V dei flussi.
Un reticolo 2D di punti quantistici é stato integrato nella struttura, mentre un altro cresciuto alle stesse condizioni é stato depositato sulla superficie senza copertura, per poter essere destinato ad analisi di microscopio.
I campioni sono stati analizzati tramite microscopia a forza atomica e i dati estrapolati utilizzando Gwyddion 2.13, un programma open-source e free-source.
Lo scopo consiste nel riuscire ad avere pieno controllo delle dimensioni, densitá e omogeneitá delle nanostrutture, modificando opportunamente i parametri di crescita epitassiale.

Nel capitolo 5 viene data una breve descrizione di Gwyddion, vengono discusse le principali sorgenti di errore e vengono presentate differenti routine per l'*image processing*. Alla luce di queste discussioni, una routine finale viene definita, con la quale le immagini AFM di tutti i campioni sono poi state elaborate.
Gwyddion é un programma modulare per analisi di immagini da SPM, e quindi anche da AFM. Le informazioni da estrarre sono:

- Densitá di punti quantistici
- Diametro medio dei punti quantistici
- Altezza media dei punti quantistici

- FWHM della distribuzione dei diametri
- FWHM della distribuzione delle altezze

Per prima cosa sono state definite le piú comuni sorgenti di errore nell'immagine, le quali correzioni sono:

- Correzione di linee orizzontali
- Correzione di graffi orizzontali
- Rimozione del background polinomiale
- Ricostruzione della superficie (deconvoluzione)
- Filtro passa basso

In base a queste operazioni sono state sviluppate 8 routine diverse, il confronto delle quali dava informazioni circa l'effetto di ogni singola correzione. Si é assunto che le prime due operazioni della lista non avessero un effetto significativo sui risultati finali. I risultati sono stati i seguenti:

- Rimozione del background polinomiale: riduce le altezze e i diametri dei punti quantistici se non sono esclusi da questa operazione tramite delle maschere protettive. Nel caso siano esclusi, il grado del polinomio da sottrarre non influenza i risultati.
- Deconvoluzione: contribuisce a ridurre l'altezza media e a restringere la sua distribuzione, mentre il diametro medio aumenta e la sua distribuzione si allarga
- Filtro passa basso: porta ad una riduzione sia delle altezze medie che dei diametri medi, lasciando, peró, inalterate le FWHM

In base a questi risultati é stato possibile quantificare l'errore stimato per densitá, diametri medi e altezze medie in 3.5%, 7.5% e 4.5% rispettivamente. Inoltre la routine finale é stata definita.

Nel capitolo 6, vengono presentati e discussi i risultati dello studio.
I punti quantistici non sono visibili nell'intervallo di temperatura 360°C-400°C. La temperaura piú bassa alla quale é avvenuta la transizione 2D-3D corrisponde a 420°C, per le condizioni di crescita utilizzate. Aumentando la temperatura fino a 480°C si nota una diminuzione della densitá e un aumento delle dimensioni medie delle nanostrutture, sebbene le distribuzioni si restringano. Il risultato é in accordo con il modello S-K di crescita auto-limitante, il quale predice un aumento del volume delle isole aumentando la temperatura e quindi il coefficiente di diffusione superficiale dell'In.
Aumentando da 2 ML a 2.2 ML il quantitativo di InAs depositato si giunge ad un effetto auto-limitante delle dimensioni. Lo strain raggiunge un valore limite che attiva il distacco degli atomi periferici del punto quantistico, riducendo le dimensioni medie dei punti. In piú, il flusso netto di corrente che allontana gli atomi distaccati da nanostrutture giá formate, induce la formazione di nuove isole coerenti, aumentandone quindi la densitá. Un ulteriore aumento di InAs depositato (2.4 ML) causa una strain talmente elevato da rompere le condizioni che inducevano l'effetto auto-limitante. La tensione, a questo punto, viene rilassata formando grandi agglomerati e aumentando la dimensione media delle strutture. A farne le spese é anche il WL che diminuisce in spessore a causa di processi

di erosione.
A bassi flussi di As la lunghezza di migrazione degli adatomi di In aumenta. Essi possono, quindi, raggiungere molto punti quantistici, ma saranno preferenzialmente assorbiti da isole piccole, limitandone le dimensioni e la distribuzione. Aumentando invece il flusso di As invece, la lunghezza di diffusione diminuisce, e quindi anche la probabilitá degli adatomi di essere assorbiti da piccole strutture, risultando in una dimensione media maggiore e una maggiore dispersione. In piú si induce la formazione di grandi agglomerati che degradano l'omogeneitá.
Ad un alto rapporto III/V di flussi, cosí come ad un basso rapporto, l'omogeneitá sembra compromessa a causa della formazione di grandi agglomerati. Il campione cresciuto con rapporto pari a 3, peró, deve essere escluso dalla serie perché i processi fisici coinvolti nella formazione di punti quantistici quando il flusso di In é maggiore del flusso di As sono diversi da quelli del metodo S-K. Aumentando il rapporto aumenta la densitá esi riducono le dimensioni medie, restringendo anche le distribuzioni. Questo é dovuto al fatto che aumentando il rapporto In:As aumenta la lunghezza di migrazione dell'In e questo permette al WL di avere una distribuzione di strain piú uniforme che porta ad una distribuzione di isole piú uniforme.
Infine, aumentando la velocitá di crescita, la densitá aumenta mentre le dimensioni medie diminuiscono. Il coefficiente di variazione dei diametri non é influenzato da ció, mentre per le altezze aumenta.
Quindi, in definitiva, le migliori condizioni di crescita epitassiale per applicazioni su celle solari a banda intermedia sono: 480°C, 2 ML InAs depositato, flusso d'As $0.5\text{x}10^{-6}$ Torr, 0.09 ML/s velocitá di crescita, che porta ad un rapporto III/V di 1/9.

Contents

Preface

This Master Thesis is the written result of my studies carried out at the Norwegian University of Science and Technology (NTNU) in Trondheim, Norway, in pursuance of the double degree program (T.I.M.E.). This Thesis is part of the requirements to achieve the MSc in Electronics Engineering at NTNU and the MSc in Physics Engineering at Politecnico di Milano (home institution).

The supervisor has been Bjørn-Ove Fimland (Department of Electronics and Telecommunications, NTNU) and the co-supervisor Turid Worren Reenaas (Department of Physics, NTNU), while, regarding Politecnico di Milano, the supervisor has been prof. Giovanni Isella.

I would like to thank all of them for having accepted me for this project and for their devotion to research. Sedsel Fretheim Thomassen and Maryam Gholami Mayani deserve a special thank for their unbelievable contribution, helpful assistance and for having grown the samples used in this study.

A special thank goes also to Francesco Puleio, Chris Katsavos and Alessandra Palumbo for having shared with me part of these amazing two years in Trondheim.

Finally, thanks to my lovely Valeria that, although the distance has kept away from me, has been the closest person every single minute.

Introduction

Edmond Becquerel first observed the photovoltaic (PV) effect in a liquid-solid interface in 1839, while W. G. Adams and R. E. Day in London carried out the first experiments with a solid-state photovoltaic cell based on selenium in 1876 [1]. However, the theory behind solar cells has its origins from some of the most important scientific developments of the 20th century [2]. The German scientist, Max Plank, began the century engrossed in the problem of trying to explain the nature of light emitted by hot bodies, such as the sun. He had to make assumption about energy being restricted to discrete levels to match theory and observations. This stimulated Albert Einstein, in 1905, to postulate that light was made of small ”particles”, later called photons, each with a tiny amount of energy that depends on photon’s colour. Einstein’s radical suggestion led to the formulation and development of quantum mechanics, culminating in 1926 in Edwing Schrödinger’s wave equation. Wilson solved this equation for material in solid form in 1930. William Shockley worked out the theory of the devices formed from junctions between ”positive” and ”negative” regions (p-n junctions) in 1949 and soon used this theory to design the first practical transistors. The semiconductor revolution of the 1950s followed, which also resulted in the first efficient solar cells in 1954.

Most solar cells presently on the market are based on silicon wafers, the so-called *first generation* technology. As this technology has matured, costs have become increasingly dominated by material costs, mostly those of the silicon wafer, the strengthened low-iron glass cover sheet, and those of other encapsulants. This trend is expected to continue as the photovoltaic industry continues to mature.

For the past 20 years, a switch to a *second generation* of thin-film technology has seemed imminent. Regardless of semiconductor, thin-films offer prospects for a major reduction in material costs by eliminating the silicon wafer. Thin films also offer other advantages, particularly the increase in the unit of manufacturing from a silicon wafer (~ 100 cm^2) to a glass sheet (~ 1 m^2), about 100 times larger [3]. As thin-film second generation technology matures, costs again progressively will become dominated by those of the constituent materials, in this case, the top cover sheet and other encapsulants required to maintain a 30-year operating life.

To progress further, conversion efficiency needs to be increased substantially. The Carnot limit on the conversion of sunlight to electricity is 95% as opposed to the theoretical upper limit of 33% for a standard solar cell. This suggests the performance of solar cells could be improved 2-3 times if different concepts were used to produce a *third generation* of high performance, low-cost photovoltaic product.

This study focuses on the Intermediate Band Solar Cell (IBSC), a novel photovoltaic

device belonging to the third generation that exploits some unique features of the quantum dots (QDs) in order to increase the overall efficiency. To be useful for this purpose, the sizes and density of the QDs need to match some requirements. It is, therefore, necessary to fully control the process of growth of the QDs.
The main focus of the study is to analyse the effect of the growth parameters on the sizes and density of QDs grown by Molecular Beam Epitaxy (MBE).

Chapter 1

First, second and third generation photovoltaics

In this chapter a brief review of the three generations photovoltaic is given. Section 1.1 focuses on the first generation, section 1.2 on the second generation while section 1.3 on the third generation.

1.1 First generation

The first efficient solar cells were created in 1954 at Bell Telephone Laboratories by Daryl Chapin, Gerald Pearson and Calvin Fuller [4]. They were a silicon-based photocells with p-n junctions characterized by an efficiency of about 6% while the first practical use of silicon solar arrays took place not on the Earth but in near-Earth space: in 1958, satellites supplied with such arrays were launched, the Soviet *Sputnik-3* and the American *Vanguard-1*.

In addition to the "classical" semiconductor materials, germanium ans silicon, materials from the III-V family group were synthesized. One such material, indium antimonide, was first reported by researchers at the Physico-Technical Institute (PTI) in 1950. Also at the PTI, at the beginning of 1960s, the first solar photocells with a p-n junction based on another III-V material, gallium arsenide (GaAs), were fabricated. Being second in efficiency ($\sim 3\%$) only to silicon photocells, GaAs cells were, neverthless, capable of operating even after being significantly heated [1].

The practical introduction of III-V materials opened a new page both in semiconductor science and in electronics. In particular, such properties of GaAs as the comparatively wide forbidden gap, the small effective masses of charge carriers, the sharp edge of optical absorption, the effective radiative recombination of carriers due to the direct band structure as well as the high electron mobility all contributed to the formation of a new field of semiconductor techniques, optoelectronics. Combining different III-V materials in heterojunctions, one could expect an essential improvement in the parameters of existing semiconductor devices and the creation of new ones.

One of the results of the study of heterojunctions was the practical realization of a wide-gap window for cells. Defectless heterojunctions using p-AlGaAs (wide-gap window) and (p-n)GaAs (photoactive region) were successfully formed; hence, ensuring ideal conditions for the photogeneration of electron-hole pairs and their collection by the p-n junction. The efficiency of such heteroface solar cells for the first time exceeded the efficiency of silicon cells. Since the photocells with a GaAs photoactive region appeared to be more radiation-resistant, they quickly found an application in space techniques, in spite of their essentially higher costs compared with silicon cells. Silicon and GaAs, to a large extent, satisfy the conditions of "ideal" semiconductor material. If one compares these materials from the point of view of their suitability for the fabrication of a solar cell with one p-n junction, then the limiting possible efficiencies of photovoltaic conversion appear to be almost similar, being close to the absolute maximum value for a single-junction photocell. It is clear that the indubitable advantages of silicon are its wide naturale abundance, non-toxicity and relatively low price. All these factors and the intensive development of the industrial production of semiconductor devices for use in the electronic industry have determined an extremely important role for silicon photocells in the formation of solar photovoltaics. Current PV production is dominated by single-junction solar cells based on silicon wafers including single crystal and multi-crystalline silicon. The majority of these types of single-junction is based on a screen printing-based device similar to that shown in Fig. 1.1.

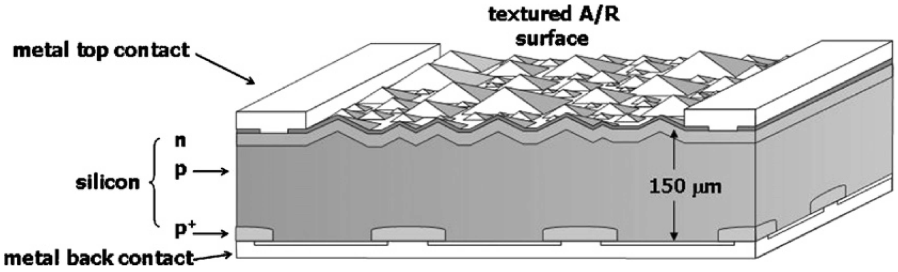

Figure 1.1: Schematic of a single-crystal solar cell [5].

Until the middle of the 1980s, both silicon and GaAs solar photocells were developed on the basis of relatively simple structures and simple technologies. For silicon photocells, a planar structure with a shallow p-n junction formed by the diffusion technique was used. Technological experience on the diffusion of impurities and wafer treatment from the fabrication of conventional silicon-based diodes and transistors was adopted. For fabricating heteroface AlGaAs/GaAs solar cells, as in growing wide-gap AlGaAs windows, it was necessary to apply epitaxial techniques. A comparatively simple liquid-phase epitaxy technique developed earlier for the fabrication of the first-generation heterolaser structures was adopted. In the case of heterophotocells, it was necessary to grow only one wide-gap p-AlGaAs layer, while the p-n junction was obtained by diffusing a p-type impurity from the melt into the n-GaAs base material.

1.2 Second generation

From the middle of the 1980s, "high technologies" began to penetrate into the semiconductor solar photovoltaics sphere. Complicated structures for silicon-based photocells, which enabled both optical and recombination losses to be decreased, were proposed. In addition, an effort to improve the quality of the base material was undertaken. The realization of such structures appeared to be possible due to the application of multi-stage technological processing well mastered by that time in the production of silicon-based integrated circuits. These efforts resulted in a steep rise in the photovoltaic conversion efficiency of silicon photocells. The efficiency demonstrated by the laboratory cells closely approached the theoretical limit.

In the thin-film approach, a thin layer of the photovoltaically active material is deposited onto a supporting substrate or superstrate. This not only greatly reduces the semiconductor material content of the finished product, it also allows for higher throughput commercial production since the module, instead of the individual cell, becomes the standard unit of production. Since the thickness of the semiconductor material required may only be of the order of 1 μm, almost any semiconductor is inexpensive enough to be a candidate for use in the cell (silicon is one of the few that is cheap enough to be used as a self-supporting wafer-based cell).

Many semiconductors have been investigated, with five thin-film technologies now the focus of commercial development [6].

1.2.1 Hydrogenated alloy of amorphous silicon

Thin films of amorphous silicon are produced using the CVD (chemical vapour deposition) of gases containing silane (SiH_4), usually ”PECVD” or ”hot wire CVD”. The layers may be deposited onto both rigid substrates (e.g. glass) and onto flexible substrates (e.g. thin metallic sheets and plastics), allowing for continuous production and diversity of use. The material that is used in solar cells is actually hydrogenated amorphous silicon, aSi:H, an alloy of silicon and hydrogen (5-20 atomic % hydrogen), in which the hydrogen plays the important role of passivating the dangling bonds that result from the random arrangement of the silicon atoms. The hydrogenated amorphous silicon is found to have a direct optical energy bandgap of 1.7 eV and an optical absorption coefficient $\alpha > 10^5$ cm^{-1} for photons with energies greater than the energy bandgap. This means that only a few microns of material are needed to absorb most of the incident light, reducing materials usage and hence cost [7].

Although the initial efficiency of the cells made in the laboratory can be >12%, commercial modules when exposed to sunlight over a period of months degrade to an efficiency of approximately 4-5%. It is, however, possible to absorb the solar spectrum more efficiently and to improve cell stability by using multiple p-i-n structures with different energy bandgap i-layers to produce ”double junction” or ”triple junction” structures.

1.2.2 Polycrystalline silicon

Silicon is a weak absorber of sunlight compared to some compound semiconductors and even to hydrogenated amorphous silicon. Early attempts to develop thin-film solar cells based on the polycrystalline silicon did not give encouraging results since the silicon layers had to be quite thick to absorb most of the available light.

However, in early 1980s, understanding of how effectively a semiconductor can trap weakly absorbed light into its volume greatly increased. Due to the optical properties of semiconductors, particularly their high refractive index, cells can trap light very effectively if the light direction is randomised, such as by striking a rough surface, once it is inside the cell. Optically a cell can appear about 50 times thicker than its actual thickness if this occurs. Such ”light trapping” removes the weak absorption disadvantage of silicon.

1.2.3 Polycrystalline compounds: chalcopyrites

The chalcopyrites are compounds based on the use of elements from groups I, III and VI of the periodic table and include copper indium diselenide ($CuInSe_2$) copper gallium indium diselenide ($CuGa_{1-x}In_xSe_2$) and copper indium disulphide ($CuInS_2$). As with amorphous silicon and cadmium telluride these materials have direct energy bandgaps and high optical absorption coefficients for photons with energies greater than the energy bandgap making it possible for a few microns of absorber layer material to absorb most of the incident light and reducing the need for a long minority carrier diffusion length [7].

1.2.4 Nanocrystalline titanium dioxide

An alternative to the all solid state solar cell is the use of a photoelectrochemical cell. To date the most successful cells of this type are the dye sensitised cells developed by Gratzel and co-workers, which are now commonly referred to as *Gratzel cells.* With this device (Fig. 1.2) the top electrode is made by screen printing a layer of TiO_2 onto fluorine doped SnO_2 coated glass and a dye applied to the TiO_2. The surface of the TiO_2 is very rough to increase the surface area and to improve light absorption. The dye usually consists of a transition metal complex based on ruthenium or osmonium. The bottom counter electrode is made by screen printing a thin layer of pyrolithic platinum onto fluorine doped SnO_2 coated glass. The device is completed by adding a suitable electrolyte (usually an iodine based solution) between the electrodes and sealing the edges to prevent escape of the electrolyte. A detailed study of long term stability of these devices has been made and the efficiency confirmed to be 8.2% efficient for a cell area of 2.36 cm^2 and 4.7% for a submodule of area 141.4 cm^2. An efficiency of 11% has also been reported for a 0.25 cm^2 area device [7]. Although such cells are in principle cheap to produce it is not yet clear where and how well they will compete with conventional cell technologies.

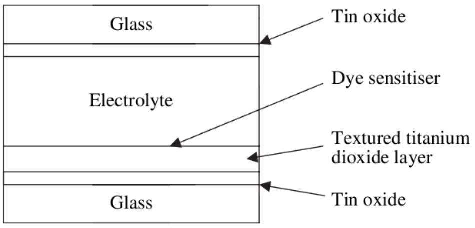

Figure 1.2: Schematic cross-sectional view of a Gratzel electrochemical cell using an iodine ion based electrolyte and dye sensitised TiO_2 electrode to absorb the light [7].

1.2.5 Cadmium telluride

Since the 1960s, CdTe has been a candidate PV material, first for space, and now the leading terrestrial product. Having a nearly ideal bandgap for a single-junction solar cell, efficient CdTe cells (Fig. 1.3) have been fabricated by a variety of potentially scalable and low-cost processes, including physical deposition, spraying, screen printing/sintering, and electrodeposition. Inherent to most cell processing is a $CdCl_2$ chemical treatment, either liquid or a currently preferred dry vapor process.

Although there are concerns, perceptions, and misconceptions about the environmental, safety, and health effect of the Cd in this device, extensive studies indicate that all safety issues can be handled with modest investments in cost, recycling of the materials and modules, and tracking of deployed product [8].

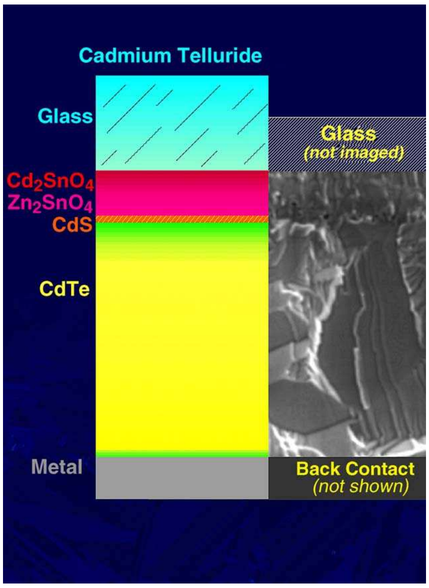

Figure 1.3: Representative cross-section of a cadmium telluride thin-film solar cell, including electron micrograph of this region [9].

1.3 Third generation

Third generation approaches to PVs aim to decrease costs to well below the \$1/W level of second generation PVs to \$0.5/W, potentially to \$0.2/W or better, by significantly increasing efficiencies but maintaining the economic and environmental cost advantages of thin-film deposition techniques [10].

1.3.1 Efficiency losses in a standard cell

Loss processes in a standard single-junction cell are indicated in Fig. 1.4, showing the energy of the electrons in the cell as a function of position across it. Photons in sunlight excite electrons from the valence band across the forbidden gap to the conduction band.

A key fundamental loss process is process 1, whereby the photoexcited electron-hole pair quickly loses any energy it may have in excess of the bandgap. A low energy red photon is just as effective in terms of outcomes as a much higher energy blue photon. This loss process alone limits conversion efficiency of a cell to about 44% [11].

Another important loss process is process 4, recombination of the photoexcited electron-hole pairs. This loss can be kept to a minimum by using a semiconductor material with appropriate properties, especially high lifetimes for the photogenerated carriers. This can be ensured by eliminating all unnecessary defects.

When open-circuited, the voltage of the ideal cell builds up so that the number of above bandgap photons emitted as part of this voltage-enhanced radiation balances the number in the incoming sunlight. At voltages below open-circuit, the number of emitted photons is less, the difference between incoming and outgoing photons being made up by electrons flowing through cell terminals.

In this way, Shockley and Queisser were able to show that the performance of standard cell was limited to 31% efficiency for an optimal cell with a bandgap of 1.3eV [12]. This is lower than the figure of 44% previously mentioned since the output voltage of the cell is less than the bandgap potential, with the difference accounted for by the voltage drops at the contact and junction (loss processes 2 and 3 in Fig. 1.4).

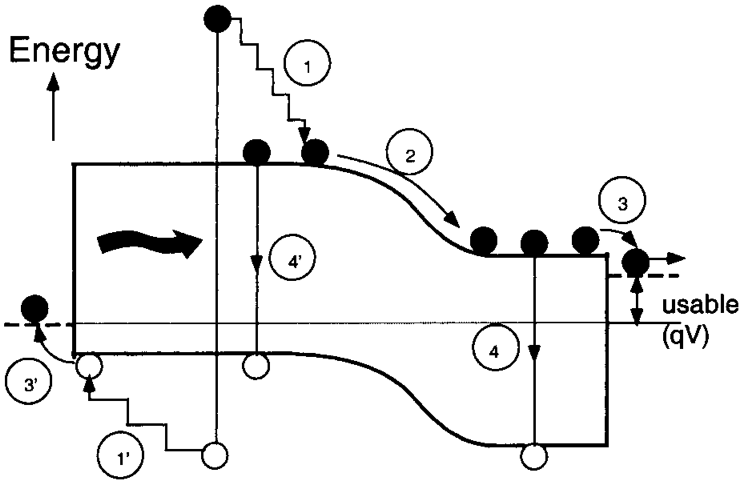

Figure 1.4: Loss processes in a standard solar cell: (1) thermalisation loss; (2) and (3) junction and contact voltage loss; (4) recombination loss [11].

1.3.2 Tandem cells

The key loss process 1 in Fig. 1.4 can be largely eliminated if the energy of the absorbed photon is just a little higher than the bandgap of the cell material. This leads to the concept of tandem cell, where multiple cells are used with different bandgaps, each cell converting a narrow range of photon energies close to its bandgap as shown in Fig. 1.5(a). Fortunately, just stacking the cells with the highest bandgap cell uppermost as shown in Fig. 1.5(b) automatically achieves the desired filtering. Limiting tandem cell performance is quite good even with a relatively small number of cells in the stack, increasing from the single cell direct sunlight efficiency of 40.8 to 55.9, 63.8 and 68.8% as the number of

independently operated cells increases to 2, 3 and 4, respectively [13].
Tandem cells are already in commercial production for two distinctly different technologies.
Double and triple junction cells based on the GaInP/GaAs/Ge system have been developed for use on spacecraft with terrestrial sunlight conversion efficiences approaching 30% with slightly higher values under concentrated sunlight. Quadruple junction devices with efficiencies approaching 40% are presently under development for such use.
Tandem cells are also used to improve the performance and reliability of terrestrial amorphous silicon cells with stabilised total-area efficiences up to 12% confirmed for triple junction cells based on the Si:Ge:H alloy system. Modules with efficiencies in the 6-7% range are available commercially incorporating double and triple junction devices [11].

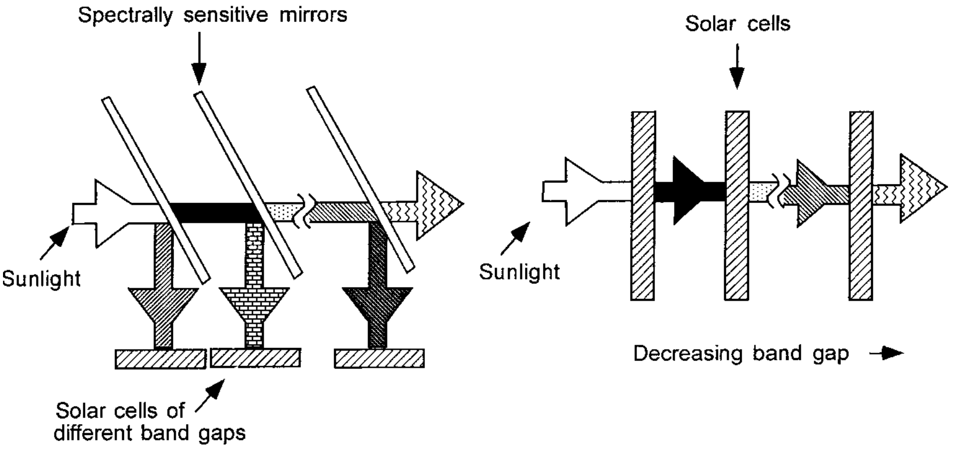

(a) (b)

Figure 1.5: Tandem cell concept: (a) spectrum splitting; (b) cell stacking [11].

1.3.3 Multiple electron-hole pairs per photon

If, instead of giving up their excess energy as heat, the high-energy electron-hole pair used it to create additional pairs as allowed by energy conservation, higher efficiency would be possible. The limiting efficiency for an idealised cell capable of taking full advantage of this impact ionisation effect is calculated as 85% for a cell of bandgap approaching zero [14].
In reality, the measured effect in any material to date is so weak so as to be able to produce negligible improvement in device performance [3].
Recently, it has been discovered that this process can be much more efficient in quatum dots (the high-energy photon has to be at least twice the bandgap energy, Fig. 1.6) [10]. The exact mechanisms involved are not yet entirely clear, but they are related to the reduced requirement for conservation of crystal momentum in the small spatial volume of a quantum dot. There is a great deal of experimental evidence showing production of up to seven electron-hole pairs for the absorption of a high energy photon.
A device based on this approach requires a means of allowing the multiple electron-hole pairs to be separated, transported, and collected in a bulk structure.

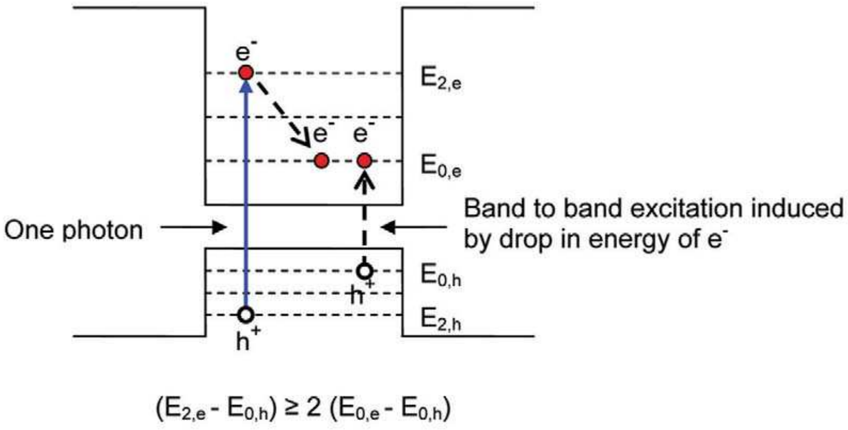

Figure 1.6: Multiple carrier generation in quantum dots: a high-energy photon is absorbed at a high energy level in the quantum dot, which then decays into two or more electron-hole pairs at the first confined energy level. Energy is conserved but momentum conservation is relaxed [10].

1.3.4 Hot carriers cells

Another option for increasing efficiencies is to allow absorption of a wide range of photon energies, but then to collect the photogenerated carriers before they have a chance to thermalize (see process 1 in Fig. 1.4). A hot-carrier solar cell is just such a device that offers the possibility of very high efficiencies (the limiting efficiency is 65% for unconcentrated illumination) but with a structure that could be conceptually simple compared with other very high efficiency PV devices.
The concept underlying hot carrier solar cells is to slow the rate of photoexcited carrier cooling, which is caused by phonon interaction in the lattice, to allow time for carriers to be collected while they are still at elevated energies. This allows higher voltages to be achieved by the cell. In addition to an absorber material that slows the rate of carrier relaxation, a hot carrier cell must allow extraction of carriers from the device through contacts that accept only a very narrow range of energies (selective energy contacts), as shown in Fig. 1.7.

1.3.5 Multiband and impurity photovoltaic cells

Standard cells rely on excitations between the valence and conduction band of a semiconductor. In 1997 Luque and Martí [15] have shown efficiency advantages if a third band, nominally an impurity band, is included in the analysis. This band can absorb photons with sub-bandgap energies, in parallel with the normal operation of a single-bandgap cell leading to a limiting efficiency of 63.1%. These additional sub-bandgap absorber can either exist as a discrete energy level in an impurity PV (IPV) cell, or as a continuous band of levels nonetheless isolated from the conduction and valence bands, the intermediate band solar cell (IBSC) shown in Fig. 1.8.

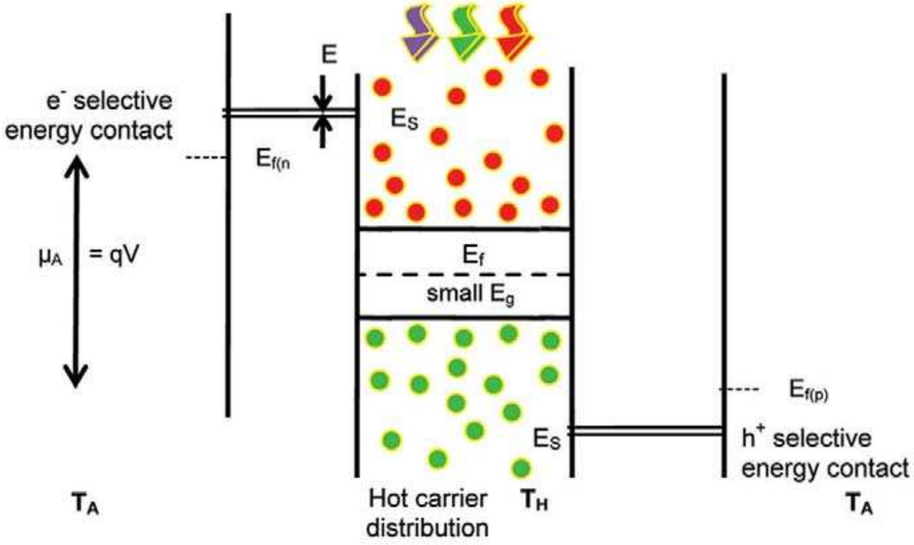

Figure 1.7: Band diagram of the hot carrier cell that requires slowed carrier cooling inthe absorption and collection of carriers through selective energy contacts [10].

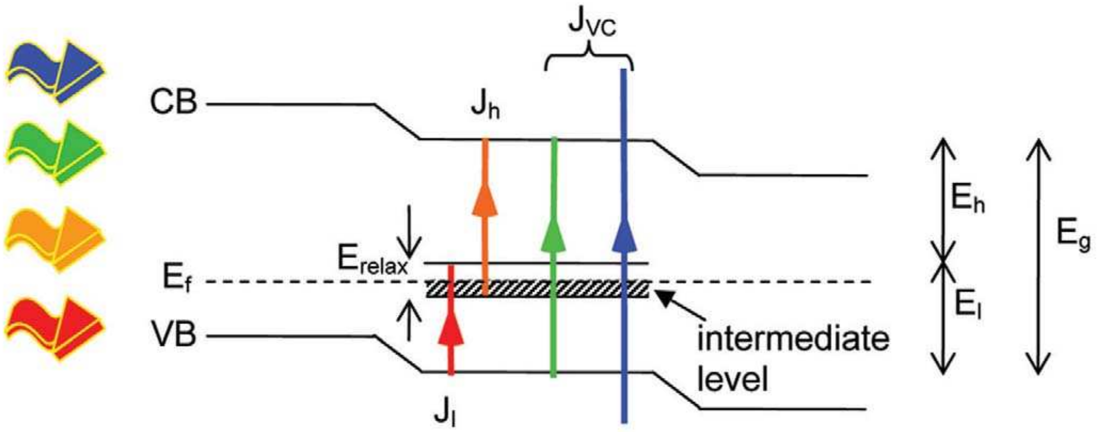

Figure 1.8: Three-band solar cell [10].

1.3.6 Thermophotovoltaic and thermophotonic devices

Thermophotovoltaics is a well-established branch of photovoltaics where the light from a heated body other than the sun is used as the illuminating source. This source may be an element heated to high temperature, such as by using a gas burner. High efficiency is possible in this case for two reasons. One is that the light source may emit a narrower bandwidth of light than the sun; a second reason is that energy from the cell, such as that reflected or emitted as light, can be recycled to the source, increasing overall efficiency.
A recent development of this approach has been called *thermophotonics*. Fig. 1.9 shows the basic arrangement, which is nearly symmetrical. Two idealised diodes acting as solar cells/light emitters face each other and are connected by a load. Heat is supplied to one to heat it hotter than the other and heat is extracted from the other to maintain it at a cooler temperature. The devices are optically coupled but thermally isolated. The combination is able to convert heat supplied to the hotter device to electricity in the load with an efficiency approaching the Carnot efficiency, in principle [11].

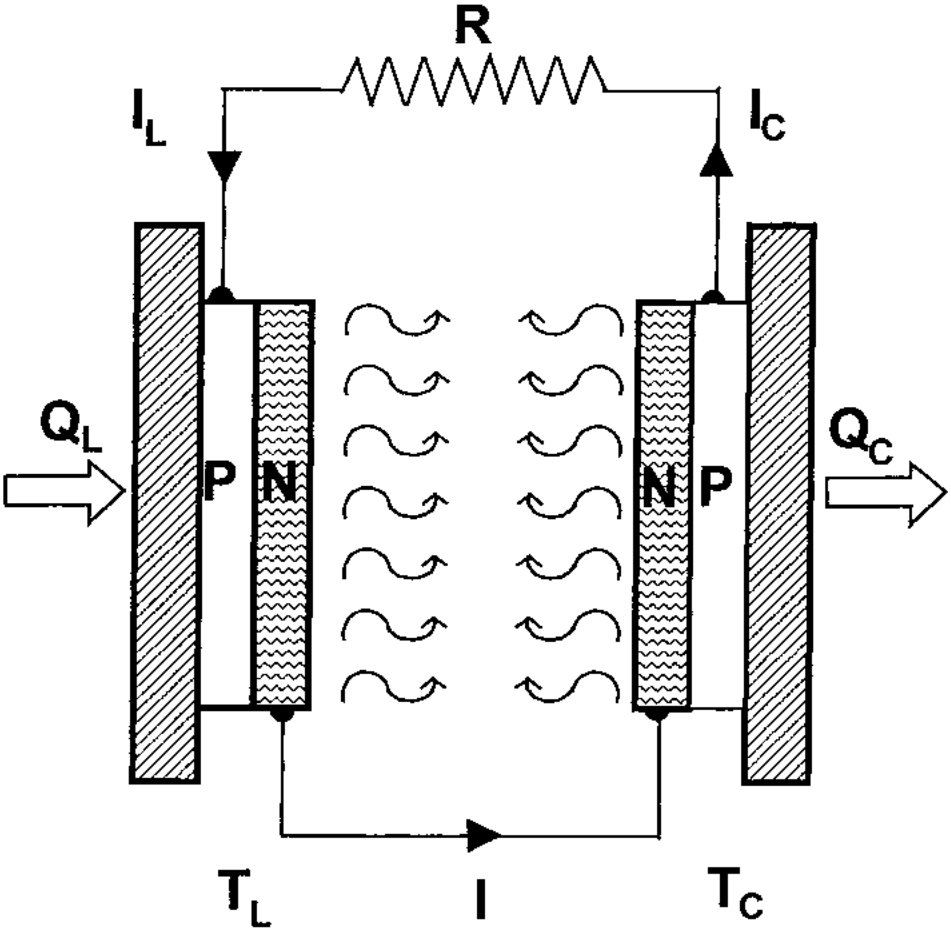

Figure 1.9: Thermophotonic conversion [11].

Chapter 2

Intermediate band solar cell

In this chapter the physics of intermediate band solar cell (IBSC) is presented. In section 2.1 and 2.2 an introduction and some preliminary concepts are given. In section 2.3 a model for IBSC is shown while in section 2.4 the implementation of the cell by means of quantum dots (QD-IBSC) is pointed out. Finally, in section 2.5 some practical considerations concerning this implementation are discussed.

2.1 Introduction

An intermediate band solar cell (IBSC) is a photovoltaic device conceived to exceed the limiting efficiency of single-gap solar cells thanks to the exploitation of the electrical and optical properties of intermediate-band (IB) material. This type of material takes its name from the existence of an extra electronic band located in between what in ordinary semiconductors constitutes its bandgap E_G. The IB divides the bandgap E_G into two forbidden energy intervals (sub-bandgaps), E_L and E_H as drawn in Fig. 2.1(left). For reasons that will become clearer shortly, it will also be required for this IB to be half-filled with electrons.

When light in this IB is absorbed, it has the potential to cause electronic transitions from the valence band (VB) to the IB, from the IB to the conduction band (CB) and, as in conventional semiconductors, also from the VB to the CB. These transitions are labelled as generation processes g_{IV}, g_{CI} and g_{CV} , respectively, in Fig. 2.1(right). The inverse or recombination processes are also labelled r_{IV}, r_{CI} and r_{CV}, respectively.

The absorption of photons takes the IB material out of equilibrium and causes the electron occupation probability in each of the band to be described by Fermi-Dirac statistics with its own quasi-Fermi level. The temperature that corresponds to this statistic will be the lattice temperature, T_C, and the quasi-Fermi level will be E_{FC}, E_{FV} and E_{FI} depending on the band we are referring to (CB, VB or IB).

We admit three different quasi-Fermi levels exist, one for each of the bands, because we assume that the carrier recombination lifetimes between bands are much longer than the carrier relaxation times within the bands. In particular, for proper IBSC operation, the quasi-Fermi level related to the IB, E_{FI}, will be considered clamped at its equilibrium position. The conditions for this hypothesis to hold are related to the excitation level and

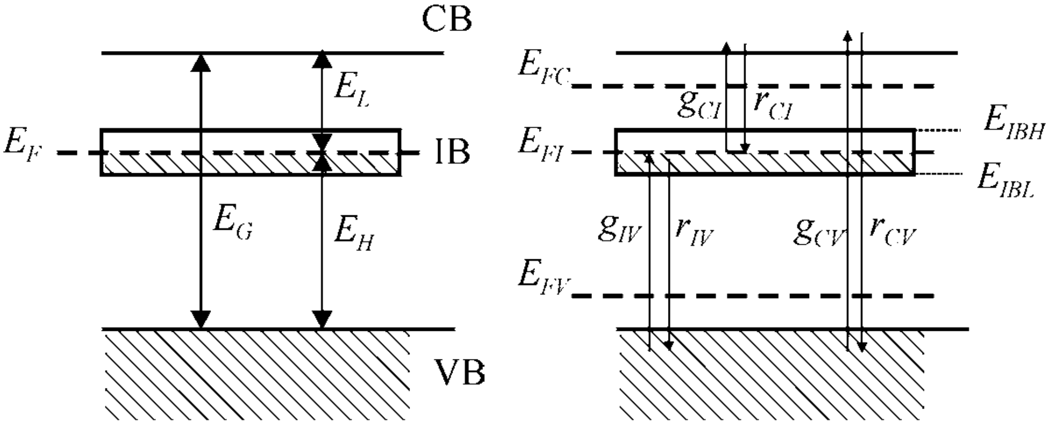

Figure 2.1: Representation of the simplified band structure of an intermediate-band material (left) in equilibrium, with the IB half-filled with electrons and (right) out of equilibrium. In the latter case, the different generation and recombination processes involved between bands are also shown as well as the quasi-Fermi levels corresponding to each of the bands. The hatched regions indicate energy states predominantly filled with electrons [1].

the density of states in the IB.

When compared with conventional single-gap solar cells, an IBSC bases its superior potential, from one side, on its capability for absorbing and converting into electricity below-bandgap photons and, from the other, on its potential for doing so without voltage loss. Both factors, current and voltage, are important.

2.2 Preliminary concepts and definitions

The IBSC is manufactured by sandwiching the IB material between two ordinary single-gap semiconductors, called emitters, of n- and p-type. The simplified band diagram of this structure, both in equilibrium and when biased, is plotted in Fig. 2.2. Ideally, the gap of the semiconductor that constitutes the emitters should be higher than the total gap of the IB material to provide a good contact selectivity for electrons and holes. This selectivity means that the p-emitter should only allow holes to go through and the n-emitter, only electrons. The emitters will be assumed not to play any optical role in the idealized model but their existence will be essential to enable a high output voltage to be obtained from the cell. In this respect, the electron's quasi-Fermi level in the emitter fixes the electron's quasi-Fermi level in the CB of the IB material, E_{FC}, and the hole's quasi-Fermi level in the p-emitter fixes the hole's quasi-Fermi level at the VB of the IB material E_{FV}. The cell output voltage is determined by the split between these two levels:

$$eV = E_{FC} - E_{FV} \tag{2.1}$$

The emitters also serve the purpose of isolating the IB from the external contacts so that no current is extracted from the IB. This isolation is what allows the effective splitting of the quasi-Fermi levels between the CB and the IB and between the VB and the IB and, therefore, according to Eq. 2.1, the possibility of extracting a high output voltage from

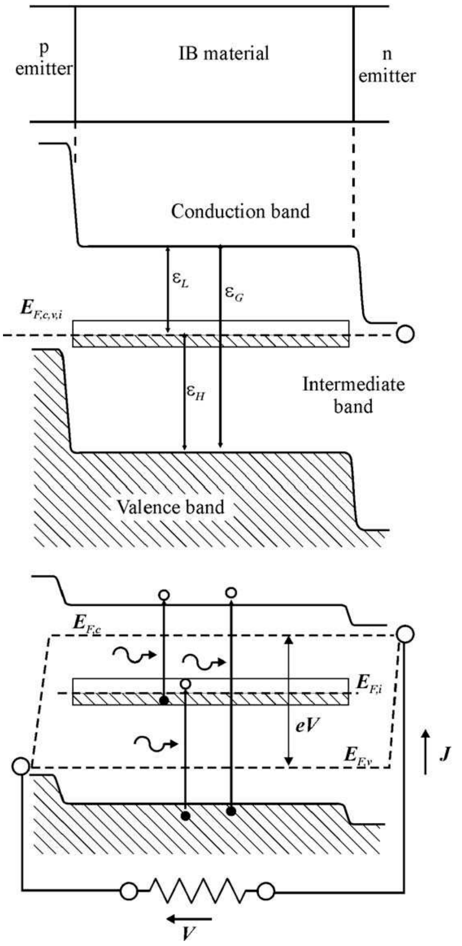

Figure 2.2: From top to bottom. Basic structure of an intermediate band solar cell. Simplified bandgap diagram in equilibrium. Simplified bandgap diagram under illumination and forward bias [16].

the cell.

Different absorption coefficients associated with each of the absorption processes that can take place in the IB material can be defined. These coefficients are labelled α_{IV}, α_{CI} and α_{CV} so as to describe the strength of the absorption of photons that cause electron transition from the VB to the IB, from the IB to the CB and from the VB to the CB, respectively. Aiming for the maximum efficiency, these processes have to be reversible, which requires, from one side, that the recombination to be exclusively radiative in nature and, from the other, that the absorption coefficients do not overlap in energy. That the absorption coefficients do not overlap in energy means that for a given photon energy, E, only one of the three absorption coefficients is non-zero or, in other words, that only one of the transitions described is possible. Hence, we shall assume that

$$\alpha_{CI} \neq 0 \qquad \text{if } E_L < E < E_H \tag{2.2}$$

$$\alpha_{IV} \neq 0 \qquad \text{if } E_H < E < E_G \tag{2.3}$$

$$\alpha_{CV} \neq 0 \qquad \text{if } E_G < E. \tag{2.4}$$

Now it is also understood why the Fermi level has been fixed within the IB. It is both to provide enough empty states in the IB to accomodate the electrons pumped from the VB and also to supply enough electrons to be pumped to the CB. In non-equilibrium conditions, this Fermi level turns into three quasi-Fermi levels for describing the concentration of electrons in the three bands. Moreover, the quasi-Fermi level in the IB is assumed to be clamped at its equilibrium position when the cell becomes excited. This is in order to prevent the IB from becoming fully filled or emptied of electrons, which would change the absorption properties of the material as a function of the biasing.

The absorption-recombination processes can be symbolically represented by the following chemical reactions:

$$h\nu_{CI} \leftrightarrow e_C + h_I \tag{2.5}$$
$$h\nu_{IV} \leftrightarrow e_I + h_V \tag{2.6}$$
$$h\nu_{CV} \leftrightarrow e_C + h_V \tag{2.7}$$

Equalling the chemical potential of the elements involved in Eq. 2.5, 2.6 and 2.7, we state that

$$\mu_{CI} = E_{FC} - E_{FI} \tag{2.8}$$
$$\mu_{IV} = E_{FI} - E_{FV} \tag{2.9}$$
$$\mu_{CV} = E_{FC} - E_{FV} \tag{2.10}$$

where μ_{XY} is the chemical potential of the photons that are in equilibrium with the creation and annihilation of electron-hole pairs between band X and Y. The spectral density of these photons is given by $b(\epsilon, \mu_{XY}, T_C)$ where

$$b(\epsilon, \mu, T) = \frac{2}{h^3 c^2} \frac{\epsilon^2}{\exp \frac{\epsilon - \mu}{kT} - 1} \tag{2.11}$$

In Eq. 2.11, ϵ is the photon energy and T the temperature. The parameters h, c and k have their usual meaning: Planck's constant, speed of light in vacuum and Boltzmann constant respectively.

There is a limitation to the quasi-Fermi level split that can be tolerated and is related to the IB width. If the upper and lower energy levels of the IB are designed by E_{IBH} and E_{IBL}, then we must have $\mu_{CI} < E_C - E_{IBH}$ and $\mu_{IV} < E_{IBL} - E_V$, where E_C and E_V are the energy limits of the CB and VB respectively, otherwise stimulated emission would take place. For maximum sunlight concentration (46050 suns), it has been estimated [1] that this bandwidth limit is in the range of 100 meV while, for 1 sun operation, this limit enlarges up to 700 meV. Conversely, there is a potential limitation for the narrowness of the IB bandwidth. It is known that as a band narrows, the carrier mobility tends to decrease. However, because no current is extracted from the IB, no carrier transport in the IB is required either as long as we keep in the model idealizations that assume that the generation and recombination processes are not dependent on position all over the IB

material.
With respect to Eq. 2.11, it will be useful to define the following auxiliary functions:

$$N_S(\epsilon_L, \epsilon_H) = \pi \int_{\epsilon_L}^{\epsilon_H} b(\epsilon, 0, T_S) d\epsilon \tag{2.12}$$

$$N(\epsilon_L, \epsilon_H, \mu_{XY}, T) = \pi \int_{\epsilon_L}^{\epsilon_H} b(\epsilon, \mu_{XY}, T) d\epsilon \tag{2.13}$$

The purpose of Eq. 2.12 is to enable the number of photons that a solar cell absorbs, when the photon spectral density is assumed to be that of a black body at temperature T_S and the maximum concentration is used. Similarly Eq. 2.13 is intended to be a tool to describe the number of photons emitted from the cell.

2.3 Intermediate band solar cell: model

In the ideal model [15], the IBSC is considered to operate in its radiative limit. In addition, ideal photon selectivity is considered so that a photon with energy E can only be absorbed by a unique type of transition. Complete photon absorption is assumed (absorptivity equal to unity).
The electron current density, J_C extracted from the n^+ contact can be obtained from using detailed balance arguments with respect to the conduction band. Hence, this current is stated to be given as the difference between the number of photons from the sun that are absorbed per unit area causing transition ending in he CB (J_{LC}/e), and those photons that are emitted outside of the cell ($J_{OC}(V)/e$) and originated in recombination mechanisms that started in the CB. For this purpose, the sun will be taken as a black body at $T_S = 6000K$, and the cell at a temperature $T_C = 300K$ and a maximum light concentration will be assumed. Therefore, in mathematical terms, we write

$$J_C = J_{LC} - J_{OC}(V) \tag{2.14}$$

where

$$J_{LC} = eN_S(E_G, \infty) + eN_S(E_L, E_H) \tag{2.15}$$

$$J_{OC}(V) = eN(E_G, \infty, eV, T_C) + eN(E_L, E_H, \mu_{CI}, T_C) \tag{2.16}$$

Similarly, the hole current density J_V, extracted from the VB is given by:

$$J_V = J_{LV} - J_{OV}(V) \tag{2.17}$$

where

$$
\begin{aligned}
J_{LV} &= eN_S(E_G,\infty) + eN_S(E_H,E_G) \qquad (2.18) \\
J_{OV}(V) &= eN(E_G,\infty,eV,T_C) + eN(E_H,E_G,eV-\mu_{CI},T_C) \qquad (2.19)
\end{aligned}
$$

The current density-voltage (J-V) characteristic of the IBSC is obtained by solving simultaneously the set of equations:

$$
\begin{aligned}
J &= J_C = J_V \qquad (2.20) \\
eV &= \mu_{CV} = \mu_{CI} + \mu_{IV} \qquad (2.21)
\end{aligned}
$$

Eq. 2.14 and 2.17 can be represented in equivalent circuit form by the circuit shown in Fig. 2.3, where the voltage between nodes X and Y corresponds to the quasi-Fermi level split μ_{XY}.

The efficiency of the IBSC, as a function of the gaps E_L and E_G (or E_H), is then trivially obtained by maximizing the output power from the cell, $P = J(V)V$, and dividing the result by the imput power, $P_{in} = \sigma T_S^4$. In a further optimization process, E_G can be optimized as a function of E_L. The results are shown in Fig. 2.4. The maximum efficiency is $E_L = 0.71$eV and $E_H = 1.24$eV (i.e. $E_G = 1.95$eV). This limiting efficiency is superior to that of single-gap solar cells (40.7%) and that of two solar cells connected in series (55.4%) as also shown in Fig. 2.4.

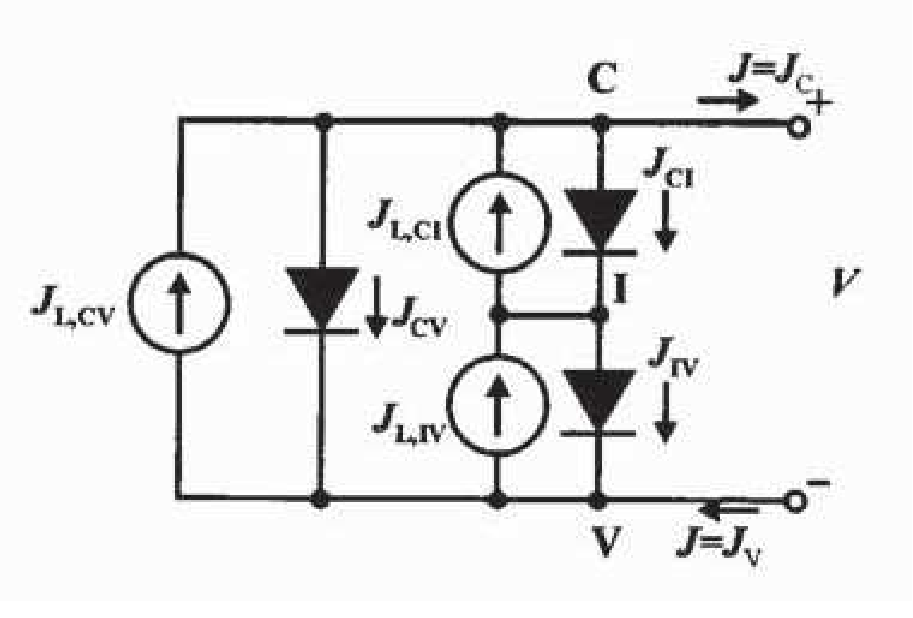

Figure 2.3: Equivalent circuit for an ideal IBSC. Under normal conditions (non-degeneracy), the currents J_{XY} follow the Shockley's diode equation quite accurately [17].

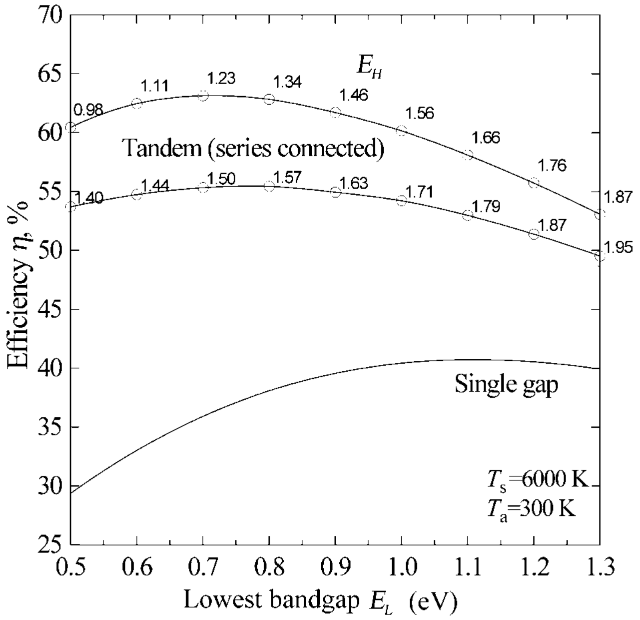

Figure 2.4: Maximum efficiency of the IBSC as a function of the lowest of the bandgaps E_L and for the optimum bandgap E_H. The limiting efficiency of single-gap solar cells and of a tandem of two solar cells connected in series is also shown for comparative purposes. In the tandem case, the figures on the curve label the optimum value of the highest of the bandgaps involved [1].

2.4 The quantum-dot intermediate band solar cell

At present three different approaches are being carried out to manufacture an IBSC [18]: (1) The direct synthesis of a material with an IB; (2) the so-called highly nanoporous approach; and (3) its implementation by means of quantum dots (QDs), that is, the so-called QD-IBSC.

2.4.1 Review of QD theory

The reduction in dimensionality produced by a confinement of electrons and holes in a material leads to a dramatic change in their behaviour.

The simplest QD geometry is a cuboid quantum dot surrounded by infinite barriers (e.g Ref. [19]), as shown in Fig. 2.5. The general three-dimensional time-independent Schrödinger equation for constant effective mass is:

$$-\frac{\hbar^2}{2m^*}\nabla^2\psi\left(x,y,z\right)+V\left(x,y,z\right)\psi\left(x,y,z\right)=E_{x,y,z}\psi\left(x,y,z\right) \tag{2.22}$$

Within the quantum dot the potential is zero, while outside the dot it is infinite; thus in the latter case the wave function is zero. Hence, the Schrödinger equation is only defined inside the box. The system allows the motions to be decoupled:

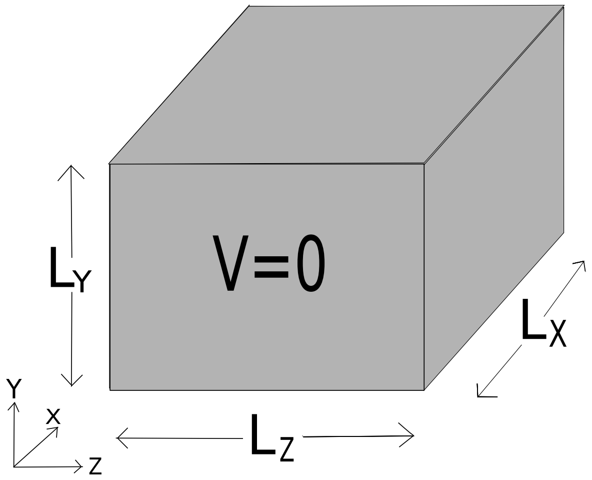

Figure 2.5: Schematic illustration of a quantum box with side L_x, L_y and L_z.

$$\psi\left(x,y,z\right)=\psi\left(x\right)\psi\left(y\right)\psi\left(z\right) \tag{2.23}$$

and then, dividing both members of Eq. 2.22 by $\psi\left(x\right)\psi\left(y\right)\psi\left(z\right)$:

$$-\frac{\hbar^2}{2m^*}\frac{1}{\psi\left(x\right)}\frac{\partial^2\psi\left(x\right)}{\partial x^2}-\frac{\hbar^2}{2m^*}\frac{1}{\psi\left(y\right)}\frac{\partial^2\psi\left(y\right)}{\partial y^2}-\frac{\hbar^2}{2m^*}\frac{1}{\psi\left(z\right)}\frac{\partial^2\psi\left(z\right)}{\partial z^2}=E_{x,y,z} \tag{2.24}$$

In Eq. 2.24, the left member is formed by a sum of three functions with different variables, and the result has to be equal to a constant eigenvalue. Hence, it is possible to associate the individual kinetic energy terms with separate energy components, by writing $E_{x,y,z}=E_x+E_y+E_z$, then:

$$\begin{cases} -\frac{\hbar^2}{2m^*}\frac{\partial^2\psi(x)}{\partial x^2}=E_x\psi\left(x\right) \\ \\ -\frac{\hbar^2}{2m^*}\frac{\partial^2\psi(y)}{\partial y^2}=E_y\psi\left(y\right) \\ \\ -\frac{\hbar^2}{2m^*}\frac{\partial^2\psi(z)}{\partial z^2}=E_z\psi\left(z\right) \end{cases} \tag{2.25}$$

Given that the potential outside the wire is infinite, then the standard boundary condition of continuity in the wave function implies that $\psi\left(x\right)$, $\psi\left(y\right)$ and $\psi\left(z\right)$ are zero at the edges of the box.

Given the origin in a corner and the box dimensions L_x, L_y and L_z, then the solutions follow as:

$$\begin{cases} \psi\left(x\right)=\sqrt{\frac{2}{L_x}}\sin\left(\frac{\pi n_x x}{L_x}\right) \\ \\ \psi\left(y\right)=\sqrt{\frac{2}{L_y}}\sin\left(\frac{\pi n_y y}{L_y}\right) \\ \\ \psi\left(z\right)=\sqrt{\frac{2}{L_z}}\sin\left(\frac{\pi n_z z}{L_z}\right) \end{cases} \tag{2.26}$$

which give the components of energy as:

$$\begin{cases} E_x = \frac{\hbar^2 \pi^2 n_x^2}{2m^* L_x^2} \\ \\ E_y = \frac{\hbar^2 \pi^2 n_y^2}{2m^* L_y^2} \\ \\ E_z = \frac{\hbar^2 \pi^2 n_z^2}{2m^* L_z^2} \end{cases} \tag{2.27}$$

Thus, the global wavefunction $\psi(x, y, z)$ and the total energy due to confinement $E_{x,y,z}$, are:

$$\begin{cases} \psi(x, y, z) = \frac{2\sqrt{2}}{\sqrt{L_x L_y L_z}} \sin\left(\frac{\pi n_x x}{L_x}\right) \sin\left(\frac{\pi n_y y}{L_y}\right) \sin\left(\frac{\pi n_z z}{L_z}\right) \\ \\ E_{x,y,z} = \frac{\hbar^2 \pi^2}{2m^*} \left(\frac{n_x^2}{L_x^2} + \frac{n_y^2}{L_y^2} + \frac{n_z^2}{L_z^2}\right) \end{cases} \tag{2.28}$$

It has to be noted that, differently from a bulk material, in a QD the charges are confined due to the well and the energy levels are discrete. The confined states are therefore described by the 3 principal quantum numbers n_x, n_y and n_z. In Fig. 2.6 the four lowest energy confined states in the yz plane are shown.

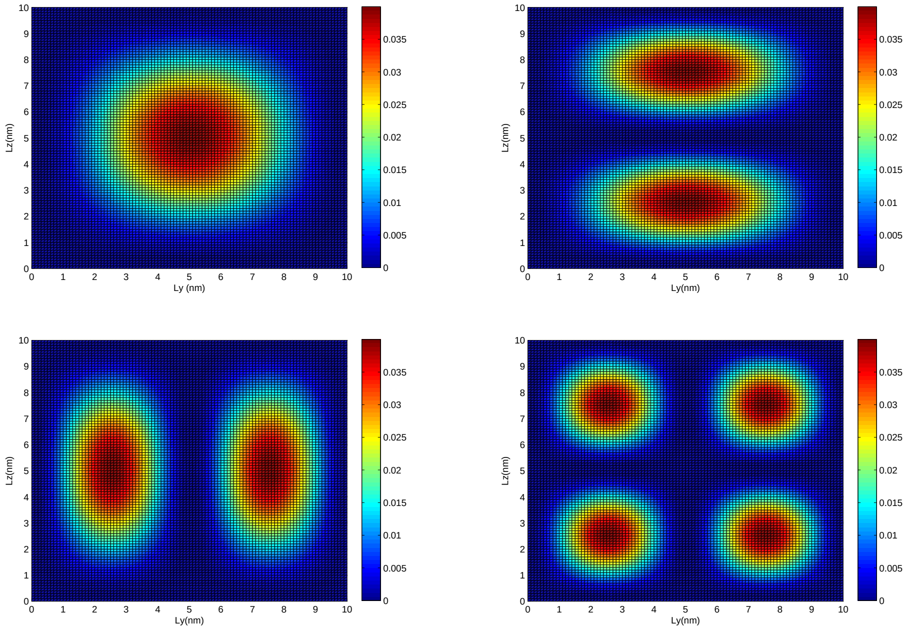

Figure 2.6: The charge density of the four lowest energy confined states within an infinitely deep quantum dot in the yz plane; (top left) $n_y = 1$, $n_z = 1$; (top right) $n_y = 1$, $n_z = 2$; (bottom left) $n_y = 2$, $n_z = 1$; (bottom right) $n_y = 2$, $n_z = 2$. The box has dimension 10nm x 10nm x 10nm.

At this point, the hypothesis of infinitely deep QD can be relaxed and a slightly different

system can be analysed.
Assume to have QD surrounded by a finite potential well. Eq. 2.28 are no longer exact eigenfunctions and eigenvalues of Schrödinger's equation for the problem. The boundary conditions have to be changed from the quantum box with infinite potential barrier to a more realistic QD with a finite well. This implies the wavefunction not to be zero at the boundary and a finite charge density appears outside the dot. Nevertheless, Eq. 2.28 can be considered a good approximation for the lower energy states if the height of the barrier is sufficiently high. A picture of a one dimensional well is shown in Fig. 2.7; as n_x incresases to more than 3, the energy becomes higher than V_0; the related charges do not experience the barrier anymore and they are free to move along the x-axis (the wavefunctions are not localized anymore).
The similarities between the energy levels in a QD and those in an atom have led to the alternative definition of *artificial atom* for these 0-dimensional quantum structures.

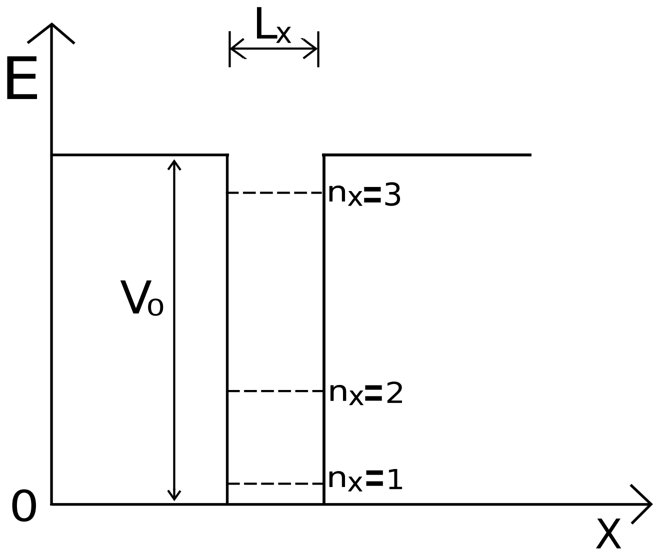

Figure 2.7: Energy levels of a QD surrounded by a potential V_0. The x direction and the lower 3 energy levels are shown.

2.4.2 From discrete levels to bands

When quantum nanostructures, such as QDs, are arranged in super-lattice arrays, minibands will be produced. In such structures, the QDs play a role similar to that of atoms in real crystal. Tomić *et al.* [20] have presented a theoretical study on the electronic structure of a QD array made by InAs/GaAs.
The calculation were based on a 8-band **k·p** Hamiltonian. In the model periodic 3D array, each QD was a truncated pyramid with a base length of $b = 12$ nm and height $h = 6$ nm, on top of a one monolayer wetting layer (Fig. 2.8). The periodicity of the array was controlled by the dimensions of the embedding box. In the x and y directions they kept periodicity constant $L_x = L_y = 20$ nm, while the periodicity along z-axes was changed in the range from 1 to 10 nm.

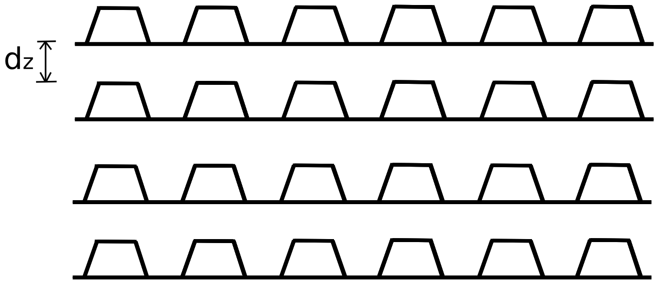

Figure 2.8: Schematic illustration of the periodic array of QD used by Tomić *et al.* [20].

In Fig. 2.9 the variation of the first three mini-bands with the period d_z, is shown. It can be noticed that when the vertical distance between the QDs is large enough, the bands collapse in levels that correspond to the discrete level of an isolate QD. As the distance becomes smaller, the quantum coupling between the dots comes into play and their wavefunctions strongly overlap, leading to the formation of minibands.
An array of dots, periodically spaced, would then lead to the required IB for the IBSC.

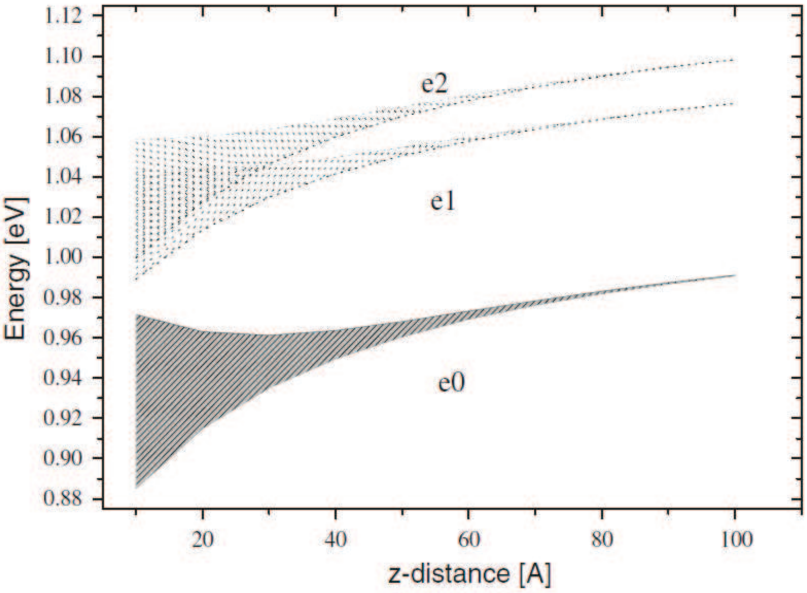

Figure 2.9: Variation of the first three minibands width in the CB with the vertical spacing of the QDs. [20].

2.5 Considerations for the implementation of the QD-IBSC

Several practical considerations concerning the implementation of the IBSC by means of the QD approach deserve to be discussed. Among them, maybe the first one is related to the size of the dots.
The appropriate size for the dots to provide the required quantum confinement depends on their geometry and on the materials being used. Considering the potential use of the

III-V semiconductors for manufacturing the array, assuming spherical dots and using the effective mass approximation, it has been estimated [1] that the radius of the dots should be in the range of 39 Å. In principle, such dot sizes are achievable by using MBE self-assembly growth techniques such as the Stranski-Krastanov mode, as discussed in chapter 3.

Another topic of interest is the density of the dots (number of the dots per unit volume). In this respect, several aspects point to the fact that this should be as high as possible with some limitations briefly discussed later.

In theory, although the dots are very well spaced, the IB structure would still hold as long as the dots are identical and located in a perfect periodic scheme. However, as the dots become more and more spaced, there is more risk for a minimal perturbation in the periodicity causing the electron wavefunctions to transit from being delocalized (as would be the case when they form part of a proper band structure) to being localized. This is the case in which the IB has lost its band structure to return to coming a mere collection of energy levels. Therefore, from this perspective, the density of dots should be as high as possible.

A benefit derived from a high density of dots is simply related to the increment in the strength of absorption of light by the dots. If the density of dots is very low, light absorption by the dots will be weak and, in order to compensate for it, the use of a high volume of QD material or, alternatively, the use of light trapping techniques, is necessary.

Another benefit derived from a high dot density is related to the clamping of the IB quasi-Fermi level at its equilibrium position. In order for this clamping to occur, the density of states in the IB has to be sufficiently high. The specific number depends on the injection level at which the cell is planned to be operated. When using QDs, the density of states is given by twice the density of dots (if dots with one confined level are manufactured), the factor two arising from taking the electron spin degeneracy into account. In this respect, it has been determined that a density of dots in the order of $10^{17} cm^{-3}$ would be necessary to clamp the quasi-Fermi level within kT for cell operation in the range of 1000 suns [1].

A third advantage comes from the fact that as the dots become more closely spaced, the IB broadens. This fact tends to increase carrier mobility in the IB and, although this mobility is not required in an idealized structure in which the IB would be uniformly excited by the generation-recombination mechanisms, it could be required, in practise, to facilitate carrier redistribution through the IB from the places where they are more intensely generated to the regions where they are more intensely recombined.

There is, however a limit to this IB broadening, the most obvious of which being to prevent the IB from mixing with the CB or VB. Another limit comes from the prevention of the appearance of stimulated emission effects. In spite of this, it seems that the centres of the dots could be safely located at a distance of 100 Å[21] without any of these problems appearing.

Chapter 3

Growth of InAs/GaAs quantum dots by MBE

In this chapter the growth of InAs/GaAs QDs by MBE is discussed. In section 3.1 the Stranski-Krastanov growth mode is presented. Afterwards, the physics behind the process is pointed out: in section 3.2 the first step of deposition is shown (2D phase), while in section 3.3 the 2D-3D transition is explained (formation of QDs). Finally, in section 3.4 the capping process is examined.

3.1 Stranski-Krastanov growth mode

One of the most widespread method for QD fabrication involves molecular beam epitaxy (MBE) of lattice-mismatched semiconductors. Initially, growth proceeds in a layer-by-layer fashion but after a critical thickness the increasing strain between the layers makes it energetically favourable for the strain to be relieved by formation of 3D islands (Fig. 3.1). This is the Stranski-Krastanov (SK) growth mode.
Growth of InAs on GaAs follows the SK model although precise details are still the subject of debate. There is a mismatch of around 7.2% between the lattice constant of InAs (6.058 Å) and GaAs (5.653 Å) and the initial 2D pseudomorphic layer known as the wetting layer (WL) persists until a critical InAs thickness (depending on growth conditions) is reached. At the critical thickness, 3D islands form and the island density increases very rapidly over a small coverage interval. The transition from 2D to 3D growth can be clearly seen during MBE growth of InAs/GaAs layers using reflection high-energy electron diffraction (RHEED). The 3D island density quickly reaches saturation and further deposition causes existing islands to ripen to an equilibrium size, and the initially broad island size distribution narrows significantly.
The size of fully mature (coherent) islands depends on growth conditions but will tipically be 3-10 nm in height and have a base diameter of a few tens of nm. Under certain growth conditions a bimodal size distribution with two distinct families of QDs may be obtained. As more InAs is deposited, QDs will eventually coalesce and dislocate. Once dislocation has occurred, elastic strain is relieved and the dislocated islands will grow rapidly in comparison with coherent islands [22].

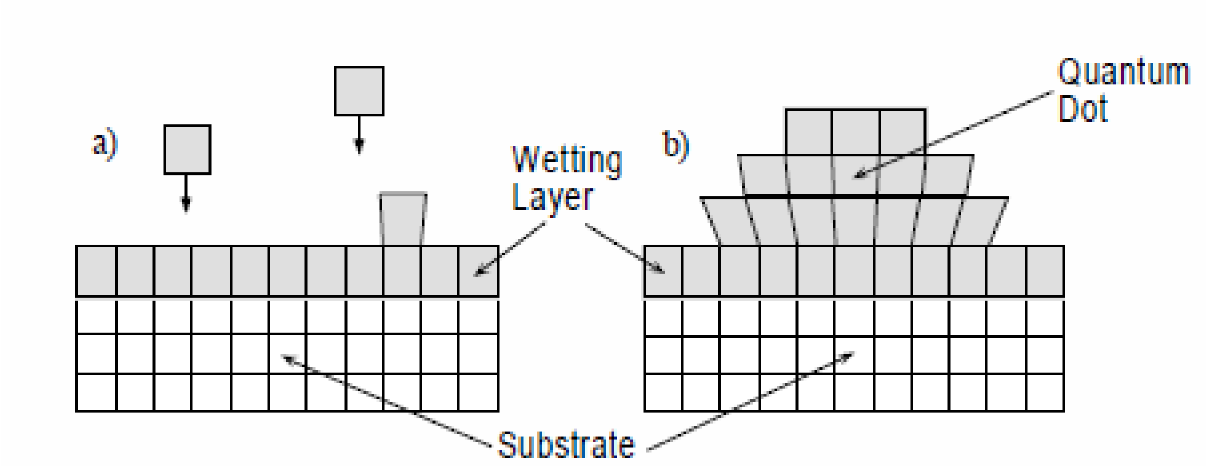

Figure 3.1: Schematic illustration of Stranski-Krastanov growth; a) strained wetting layer, b) formation of a quantum dot.

Although heteroepitaxy of InAs/GaAs(001) is of SK type, such a transition has a more complex evolution from its initial stage. Specific issues, which differ from the conventional SK growth are, for instance, the following [23]:

(i) the 2D WL is an InGaAs alloy having a precise composition at the transition [24];

(ii) the 2D to 3D transition, at the critical thickness, occours within 0.2 ML of InAs deposition, by the sudden nucleation of $10^{10} - 10^{11}$ cm^{-2} QDs which are coherent and strained;

(iii) InAs QDs include some Ga at their bases, whose amount depends on growth conditions;

(iv) the nucleated 3D volume is far larger than that being deposited in the narrow coverage range where nucleation is completed.

Other details of InAs/GaAs heteroepitaxy concern thermodynamic and kinetic aspects of the growth, such as the dependence of the critical thickness on substrate temperature and In flux.

3.2 The 2D phase: wetting layer and critical thickness

During the deposition process of InAs on GaAs substrate, the InAs-GaAs interface is not merely abrupt and the first monolayer deposited is far from being pure InAs. *Surface segregation*[1] and In-Ga exchange affect the composition of the growth film.

Cullis *et al* [24] propose a model (called WCNH) for the SK growth of strained semiconductor heterostructures which focuses on the WL composition and, in particular, on the strain dependence of the critical thickness, in $In_xGa_{1-x}As/GaAs$ systems, as a consequence on In segregation in the WL. The model considers exchange of the group-III species between the top two layers during growth so that the surface layer exhibits a very substantial deviation from the deposition flux concentration. If a relatively diluite (x=0.25) alloy is deposited, Fig. 3.2 shows the way in which the In concentration is predicted by the theory to evolve within the growing flat layer. It is evident that segregation of In to the surface enhances the In concentration in the surface monolayer rapidly above that of the deposition flux so that, for only ~ 1 nm of layer growth, the surface In concentration is already above 40%. It is then important to determine the variation in predicted surface In concentration as a function of deposition flux composition. This is presented in Fig. 3.3 (left panel) where the curves show this quantity for deposition fluxes containing from 5% to 100%.

The WCNH mechanism proposes that a critical surface concentration of In (and associated strain) must build up before the SK-islanding transition take place. Since a deposition flux of 25% In is approximately the lowest that will induce the SK transition, it is possible to identify the corresponding critical surface In concentration from the associated curve in Fig. 3.2: the critical concentration would be predicted to be 80-85% In in the surface layer (saturation concentration). For any particular deposition flux, it is predicted that the SK transition will take place after the surface In concentration rises to this critical level. Thus the islanding transition points for layers grown over the complete range of deposition fluxes can be estimated from plots of the type given in Fig. 3.3 (left panel), so that is possible to estimate the critical transition thickness of the initial flat wetting layer as a function of deposited In concentration. This then gives the continuous ”theoretical” curve in Fig. 3.3 (right panel), which extends from 2.5 nm thickness for a deposition flux of 25% In to 0.3 nm thickness for InAs deposition. It is evident that the thoretically and experimentally derived curves exhibit exactly the same form and are displaced from one another by no more than 0.1-0.5 nm, depending upon In flux concentration. The near coincidence of the curves lends strong support for the importance of segregation in determining the SK 2D-3D transition point, as proposed in the WCNH mechanism.

For deposition of InAs on GaAs, an initial delay in the increase of the surface In concentration to 100% [curve (g) in Fig. 3.3 (left panel)] results from the exchange of In atoms with Ga atoms in the GaAs surface. In this latter case, partial completion of the second monolayer is required before the surface In concentration and associated strain become high enough to trigger the SK 3D-islanding transition.

---

[1] The term surface segregation refers to the enrichment of one or more component of the mixture in the surface region, relative to bulk composition, through the perturbation of the bonding mechanism [25]

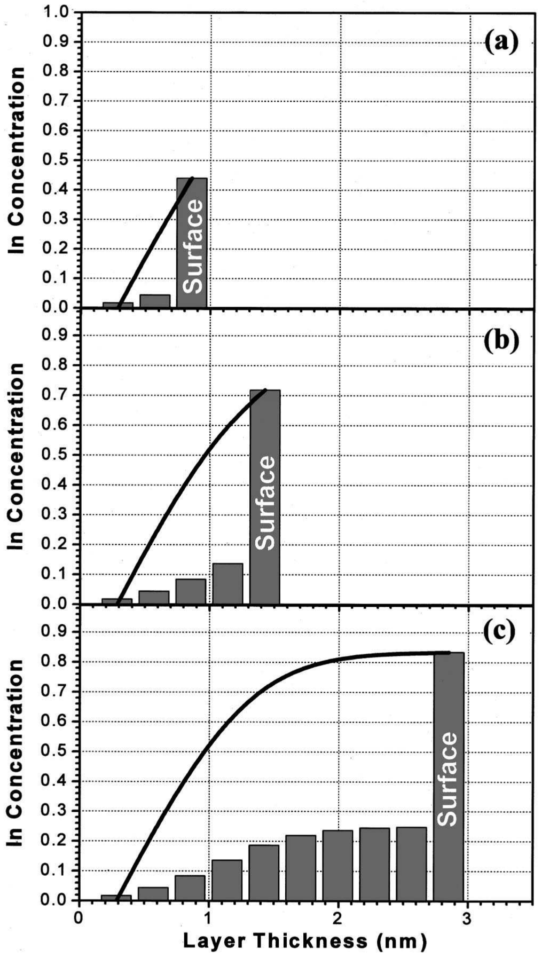

Figure 3.2: Composition variations in the near-surface $In_xGa_{1-x}As$ monolayers (shown by bars), driven by In segregation to the surface (In concentration variation in the surface monolayer is tracked by the solid line). Deposition flux is 25% In and different total-growth thicknesses are: (a) 3 monolayers, (b) 5 monolayers, and (c) 10 monolayers [24].

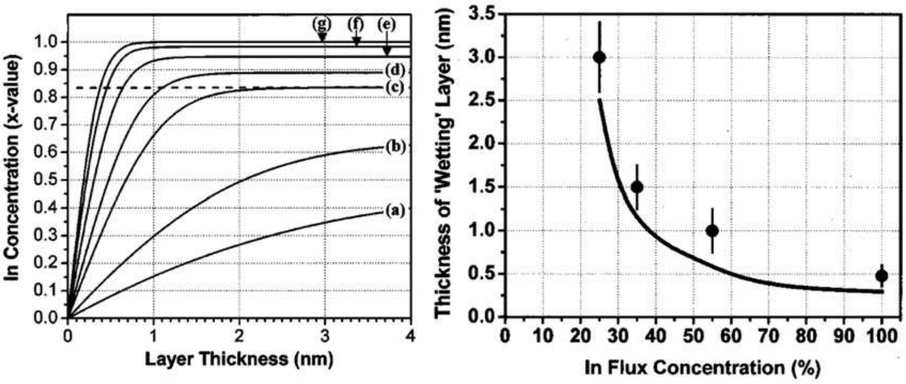

Figure 3.3: Left panel: composition variations in the surface monolayer, driven by In segregation to the surface, for deposition fluxes with (a) 5% In, (b) 10% In, (c) 25% In, (d) 35% In, (e) 55% In, (f) 80% In, and (g) 100% In. Right panel: variation in the flat-layer thickness for the islanding transition as a function of In concentration in the deposition flux: measured values given as data points and theoretically predicted values based upon the WCNH mechanism presented as a continuous curve [23].

3.3 The 3D phase: evolution of the surface morphology during 2D-3D transition

Close to the critical thickness, the morphology of the InAs/GaAs(001) interface become quite rich, as shown in Fig. 3.4. The images reveal an involved morphology of the WL comprising 2D islands 1 ML high, and large terraces one step high. Kinetic instabilities of the growth due to anisotropy of diffusion and the extra barrier for down-hopping at step edges, give rise to the stepped texture of the WL, which strongly influences the in-plane position of dots; in fact, most of them nucleate at step edges. 2D islands appear in all samples at about 1.4 ML and vanish when the massive nucleation of large QDs is taking place. The first small QDs are recognizable for coverage as high as 1.45 ML, whereas at higher InAs deposits the formation and subsequent number increase of large QDs can be seen. Small QDs nucleate preferentially at the upper-step edges of 2D islands and terraces by reason of a favourable strain condition at these sites. Placidi *et al.* [23] demonstrate that they are not simple precursors of large QDs but the process involves a more complex kinetic mechanism.

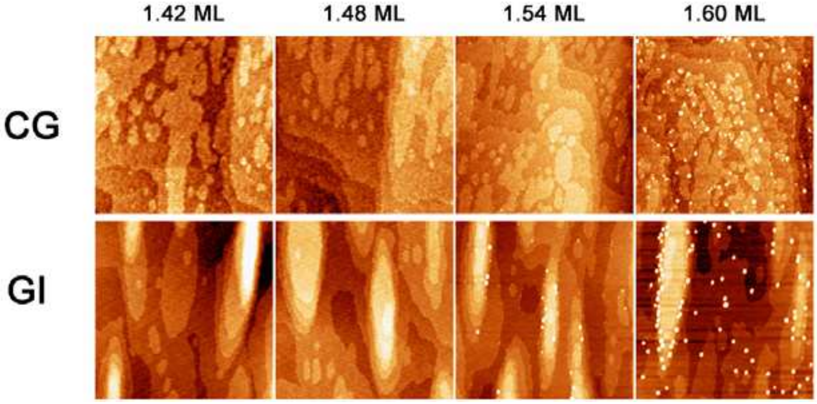

Figure 3.4: 1x1 μm^2 AFM topographies for continuous growth (CG) and growth interruption (GI) samples. The images show the WL at 1.42 ML, free from 3D features, the first small QDs at 1.48 ML and the occurrence of large QDs at 1.54 ML for the GI sample and at 1.60 ML for the other. Adapeted from [23].

The number density evolution of both small and large QDs for the GI (growth interruption) sample is shown in Fig. 3.5. The number of the small QDs begins to increase at 1.45 ML and maximizes at 1.57 ML. Starting from 1.52 ML, the number of the large QDs increases gradually, then, between 1.57 and 1.61 ML, it undergoes a sudden rise, changing value by an order of magnitude. At higher coverages (>1.8 ML) the density rise is much slower.

One of the puzzling aspects of the self-assembled QDs is that the nucleated 3D volume is far larger than that being deposited in the narrow coverage range where the entire nucleation process is completed. This phenomen could be a consequence of the *erosion* of step edge surrounding dots. If the total dot volume was plotted as a function of the deposited InAs (not shown), two regions with different slopes would be distinguished [23]. In the range 1.6-1.8 ML, the dependence of the dot volume on coverage is linear, with

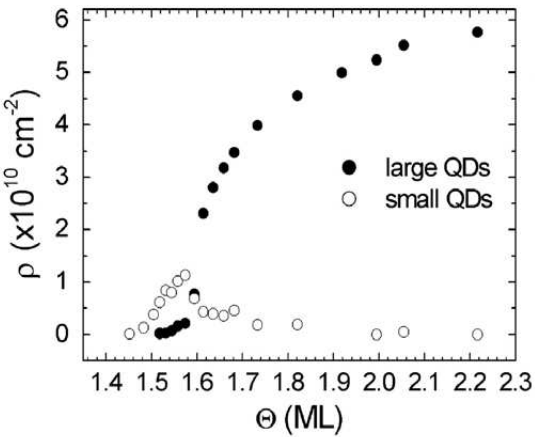

Figure 3.5: Number density dependence on InAs coverage of small and large QDs [23].

slope $F_t \sim 4F_0$ for all the samples, where F_0 is the slope of the straight line representing the volume being deposited by the impinging InAs flux. Above 1.8 ML, the volume increases at the same rate F_0 as the coverage. It is worth underlining that the volume behaviour just described is clear evidence of large surface mass transport from the 2D to the 3D phase at the very initial stage of the transition. This can be quantified as an extra coverage of approximately $\Delta t = 0.9$ ML for the CG (continuous growth) and the GI samples. Such mass transfer ends above 1.8 ML, above which the volume increases solely at the expense of the incoming flux.

The ensuing discussion concerns the microscopic origin of such excess volume.

While at the beginning of nucleation all dots nucleate on step edge, at 1.9 ML $\sim$ 60% of them are found below it. This is consistent with the fact that dots first nucleate at the upper side of the step edge, then, as a result of step erosion, they are located at the lower side of the step. Therefore, in addition to surface segregation and substrate intermixing, a relevant fraction of the dot volume comes from step erosion: not enough, however, to account for all the 3D volume in excess. A further contribution can be attribuited to the presence of floating In adatoms at the very beginning of nucleation.

3.4 Overgrowth: capping process

Freestanding islands are hardly ever employed but are instead covered by a capping layer (typically of the same material as the substrate) that preserves them from the external environment and suppresses nonradiative recombination through surface states also at the upper interface.

A fundamental aspect that has attracted substantial attention is that the deposition of the capping layer might be, and very often is, far from being harmless for the 3D islands [26–29]. In fact, the capping procedure itself is a lattice mismatched heteroepitaxial process and is therefore associated with strain release, segregation, faceting, intermixing, strain-enhanced diffusion, etc. These phenomena take place at the island surface and can strongly modify the QD morphology and composition. Since the optical and electronic properties of QDs strongly depend on their size, shape, and stoichiometry, a detailed microscopic understanding of the capping process that ultimately allows a tailoring of the

optoelectronic characteristics becomes essential.
Strong differences in the capping process have been found, depending on the size of the QDs, but here we focuses on the model for small QDs [29] (suitable for IBSC application), shown in Fig. 3.6.
Exceeding the critical thickness, the InAs layer can relax strain energy by forming the QD structure [Fig. 3.6(a)]. The relaxation occours mostly at the apex of the QD, while the base remains almost at the GaAs lattice parameter due to the pseudomorphic interface. Thus, the local lattice parameter (LLP) at the QD apex is close to the value of bulk InAs, decreasing slightly toward its base edges and corners. The strain energy of this freestanding, uncapped QD amounts to 40%-60% of the energy of the same one capped and thus compressed into the lattice of the surrounding GaAs matrix. During capping the amount of relaxed strain energy in principle has to be reinvested. In the directly surrounding GaAs matrix, the LLP becomes slightly lower than the lattice constant of bulk GaAs. Only far away from the QDs the GaAs capping material adopts its bulk lattice constant. The strain energy situation for the GaAs material strikinig directly the QD is most unfavorable. Thereby, it diffuses toward the sides of the QD where it finds more preferential sticking positions, dragging the InAs from the apex along with it [Fig. 3.6(b) and 3.6(c), lateral arrows]. Thus, the apex gets removed, and both materials intermix and stick to the sides of the QD, increasing the steepness of the side facets. On the one hand, this process leads to a global strain energy reduction compared with the situation of a capped pyramid. On the other hand, the LLP on top of the QD slightly decreases since the distance to the base becomes smaller. During further capping [Fig. 3.6(d)] the GaAs layer is higher above the WL than above the QD, and the QD itself gets covered first at its side and finally at its center. This is the result of a competition between the strain energy and the step energies of a rough growth surface. Finally, the QD gets completely capped and the GaAs growth surface flattens again [Fig. 3.6(e)]. Segregation also occours at the WL after deposition of GaAs [Fig. 3.6(b) and 3.6(d), vertical arrows].

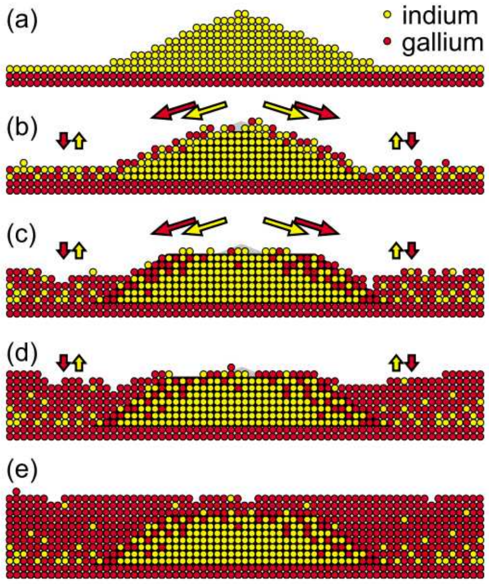

Figure 3.6: Schematic model for the capping process of the QD structure: (a) the situation before capping and [(b)-(e)] after deposition of increasingly thick capping layers [29].

Chapter 4

Experimental

The goal of this thesis is to study the dependence of the QDs density and sizes on the growth parameters, for intermediate band solar cell application.
Self-organized InAs/GaAs QDs structures were grown on n-type GaAs(001) substrate by a Veeco Gen-II solid-source molecular beam epitaxy (MBE) system. The grown layers consisted of a 200 nm GaAs buffer layer grown at 590°C. Afterwards growth was interrupted and the substrate temperature reduced to the value chosen for QD growth. The InAs QDs were capped by 10 nm GaAs grown at the same substrate temperature as the QDs. Then the growth was interrupted again and the substrate temperature raised to 590°C for further 40 nm GaAs deposition. Another QD layer was repeated after the GaAs barrier layer, at the same growth conditions as the buried one, for AFM examinations.
The basic structure of the samples is also shown in Fig. 4.1.

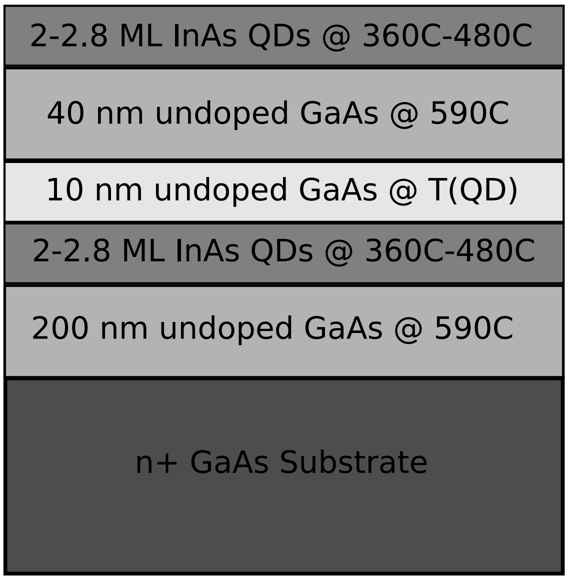

Figure 4.1: Schematic view of the samples structure. Although the structures are qualitatively the same, they were grown at different temperatures (ranging from 360°C to 480°C), with different InAs thicknesses (from 2.0ML to 2.8ML), with different Arsenic fluxes and at different rates.

Several samples were investigated which are summarized in Tab. 4.1.
Each sample was cut and the central region was removed and studied. The measurments were performed in the Physics Department at NTNU, using AFM Multi-Mode^{TM}Scanning Probe Microscope (MM-SPM), Digital Instruments, in contact mode.
For each sample, 3 images of the topmost layer at different magnification (1x1 μm^2, 500x500 nm^2 and 200x200 nm^2) were taken. Then the pictures at 500x500 nm^2 were analyzed using *Gwyddion 2.13*, a program for SPM data analysis, by which density and sizes of QDs were extracted.
Therefore, we examined:

- The influence of the growth temperature on the density and sizes
- The influence of the InAs thickness on the density and sizes
- The influence of the As-flux on the density and sizes
- The influence of growth rate and In:As flux ratio on the density and sizes

Sample	Growth temp. [$\circ$C]	InAs thickness [ML]	As flux [10^{-6} Torr]	Growth rate [ML/s]	In:As flux ratio
541-1	460	2	2	0.09	1:30
541-2	380	2	2	0.09	1:30
541-3	420	2	2	0.09	1:30
541-4	400	2	2	0.09	1:30
542-1	380	2.8	2	0.09	1:30
542-3	360	2	2	0.09	1:30
542-4	380	2.4	2	0.09	1:30
543-1	480	2	6	0.09	1:106
543-2	480	2	2	0.09	1:30
543-3	480	2	0.5	0.09	1:9
544-1	480	2.2	2	0.09	1:30
544-2	480	2.4	2	0.09	1:30
547-1	480	2	2	0.5	1:7
547-2	480	2	2	1	3:1

Table 4.1: Summary of growth conditions used for the investigated samples.

Chapter 5

Image processing using Gwyddion

In this chapter, a brief description of Gwyddion is given in section 5.1. Moreover in section 5.2 the main sources of errors are discussed and in section 5.3 different routines for image processing are presented. The results of the processing are shown in section 5.4, while the final routine and the estimated errors are stated in section 5.5.

5.1 Introduction

Gwyddion is a modular program for SPM data analysis. Primarily it is supposed to be used for analysis of height fields obtained by means of scanning probe microscopy techniques (AFM, MFM, STM, NSOM), but generally it can be used for any other height field analysis or image analysis.
It is a free-source and open-source program available on internet [30]; it is also possible to find a comprehensive user guide [31].
The useful information that we want to extract from an AFM image are:

- The density of QDs
- The mean diameter of QDs
- The mean height of QDs
- The FWHM of diameters' distribution
- The FWHM of heights' distribution

By Gwyddion it is possible to extract a raw data file containing all the information we need. Processing the raw data by, e.g. MATLAB®, allows us to get the final results.

5.2 Sources of error

An AFM image will typically be affected by several sources of error (horizontal scars, lines, noise, etc.), that compromise the quality of the picture and the validity of the results. It

is, therefore, fundamental to set the most important nonlinerities and sources of error that have to be corrected before quantitatively analySe the image, trying to preserve the information in it.
In Fig. 5.1 and 5.2 it is shown an AFM image at which no processing has been carried out. There are visible horizontal lines and a curved background that could influence the results.

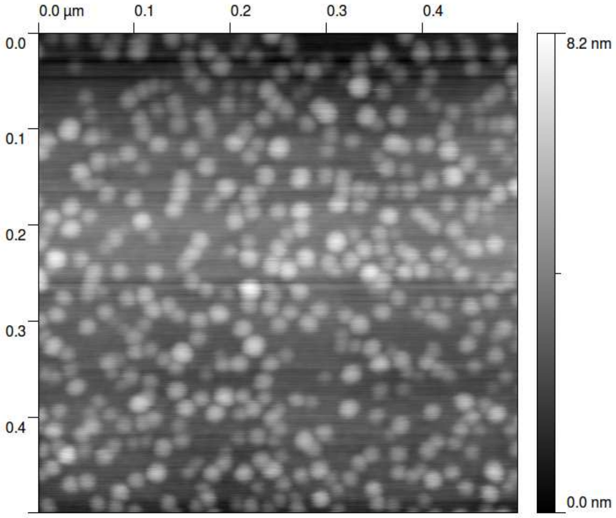

Figure 5.1: Example of AFM image, surface view.

Moreover, it is known that the image got is, actually, the convolution of the real surface with the AFM tip. It is, indeed, not the physical surface the one detected by AFM, although, depending on the sharpness of the tip, it could be in some cases very similar to the real one. However, the image should be corrected from convolution if we want to get trustable values. Finally, the last source of error considered is the noise, which has the high frequency contribution.
So, the main actions taken the image should be:

- Correction of lines
- Correction of horizontal scars
- Removal of polynomial background
- Surface reconstruction (deconvolution process)
- Low pass filtering (2D FFT filtering)

The main questions are to understand which is the effect of any correction we apply on the image and to define a reliable image routine. This study is also necessary in order to state the error range of the results.

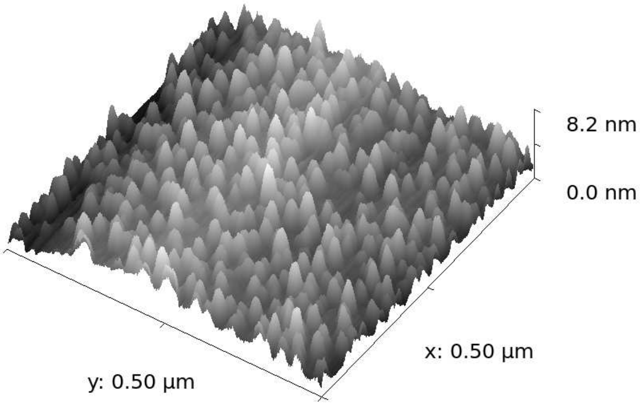

Figure 5.2: Example of AFM image, 3D plot.

5.3 Image processing: different routines

There were set 8 different routines for the same image and, by comparison of the different quantitative results, it was possible to define a common routine for all the AFM images used in this thesis. The routines are the following:

Routine 1

- Correct lines
- Correct horizontal scars
- Mark grains
- Extract raw data

In this routine, after the correction of lines and scars, the grains (QDs) are marked by masks. Under every mask, there are information concerning the QDs. The raw data extracted are related to the regions under the masks, so to the QDs.

Routine 2

- Correct lines
- Correct horizontal scars
- Remove polynomial background (horizontal polynom degree 3^{rd} and vertical polynom degree 3^{rd})
- Mark grains
- Extract raw data

In this routine, the background is removed using a 3^{rd} degree polynom as fitting function. The entire image is used for fitting.

Routine 3

- Correct lines
- Correct horizontal scars
- Mark grains
- Remove polynomial background (horizontal polynom degree 3^{rd} and vertical polynom degree 3^{rd}, excluding region under mask)
- Extract raw data

In this routine, the background is removed using a 3^{rd} degree polynom as fitting function but it is not exploited the entire image for fitting. The QDs are excluded from the operation and preserved from the previous operation.

Routine 4

- Correct lines
- Correct horizontal scars
- Mark grains
- Remove polynomial background (horizontal polynom degree 3^{rd} and vertical polynom degree 3^{rd}, excluding region under mask)
- Blind tip estimation (run partial)
- Surface reconstruction
- Mark grains in the deconvoluted image
- Extract raw data

In this routine, the background is removed using a 3^{rd} degree polynom as fitting function but it is not exploited the entire image for fitting. The QDs are excluded from the operation and preserved from the previous operation. Afterwards, a blind tip estimation is performed and the deconvolution is carried out using as tip the estimated one.

Routine 5

- Correct lines
- Correct horizontal scars
- Remove polynomial background (horizontal polynom degree 3^{rd} and vertical polynom degree 3^{rd})
- Blind tip estimation (run partial)
- Surface reconstruction
- Mark grains in the deconvoluted image
- Extract raw data

In this routine, the background is removed using a 3^{rd} degree polynom as fitting function. The entire image is used for fitting. Afterwards, a blind tip estimation is performed and the deconvolution is carried out using as tip the estimated one.

Routine 6

- Correct lines
- Correct horizontal scars
- Mark grains
- Remove polynomial background (horizontal polynom degree 3^{rd} and vertical polynom degree 3^{rd}, excluding region under mask)
- Low pass filtering (2D FFT filtering)
- Mark grains in the filtered image
- Extract raw data

In this routine, the background is removed using a 3^{rd} degree polynom as fitting function but it is not exploited the entire image for fitting. The QDs are excluded from the operation and preserved from the previous operation. Afterwards, low pass filtering is carried out.

Routine 7

- Correct lines

- Correct horizontal scars
- Mark grains
- Remove polynomial background (horizontal polynom degree 1st and vertical polynom degree 1st, excluding region under mask)
- Extract raw data

In this routine, the background is removed using a 1st degree polynom as fitting function but it is not exploited the entire image for fitting. The QDs are excluded from the operation and preserved from the previous operation.

Routine 8

- Correct lines
- Correct horizontal scars
- Mark grains
- Remove polynomial background (horizontal polynom degree 2nd and vertical polynom degree 2nd, excluding region under mask)
- Extract raw data

In this routine, the background is removed using a 2nd degree polynom as fitting function but it is not exploited the entire image for fitting. The QDs are excluded from the operation and preserved from the previous operation.

In all the routines is assumed that correcting lines and horizontal scars does not affect significantly the final results.
Comparing routine 1,2 and 3 is, therefore, possible to analyze the effect of background subtraction including and excluding the regions under the masks; comparing routine 7, 8 and 3 the different degrees of polynomial background subtraction are studied. Moreover, looking at routine 2 and 5 as weel as routine 3 and 4, the effect of surface reconstruction is evaluated. Finally routine 3 and 6 give information about low pass filtering.

5.4 Image processing: results

5.4.1 Background subtraction

In Fig. 5.3 and 5.4 the effect of the background subtraction including and excluding the region under the masks is shown, considering the distribution of diameters and heights of the QDs.
Removing polynomial background including the grains leads to a marked reduction (~1nm) in mean diameter, while the mean height does not seem to be affected. It suggests that removing polynomial background without ”protecting” the QD from this action affects

the contour of the QD, a sensitive part of the image that strongly feels the effect of subtraction. Moreover the normal distributions fitting of routine 1 and 3 are overlapped, as expected.
Fig. 5.5 and 5.6, instead, show the comparison between the 1st, the 2nd and the 3rd order of polynomial background subtracted from the original image, excluding the QDs. Undoubtedly the three routines lead to an identical result, both for diameters and heights.

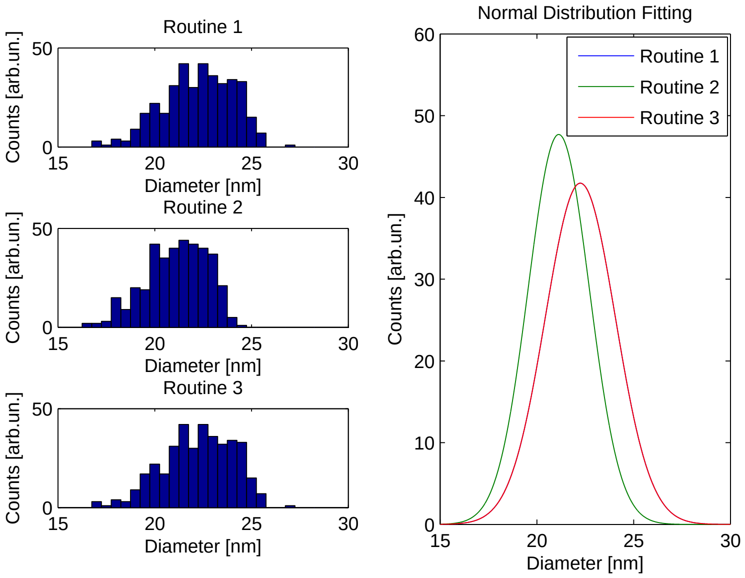

Figure 5.3: Histograms and normal distributions fitting of diameters for routine 1, 2 and 3. The normal distributions of routine 1 and 3 are overlapped.

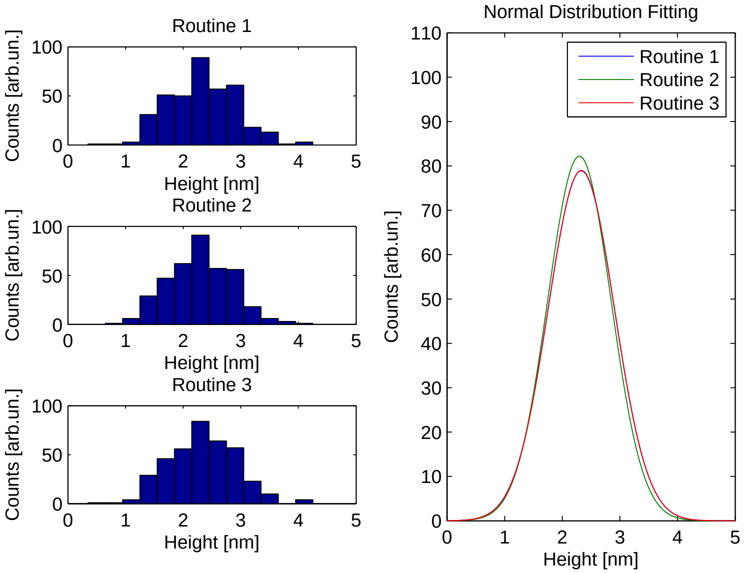

Figure 5.4: Histograms and normal distributions fitting of heights for routine 1, 2 and 3. The normal distributions of routine 1 and 3 are overlapped.

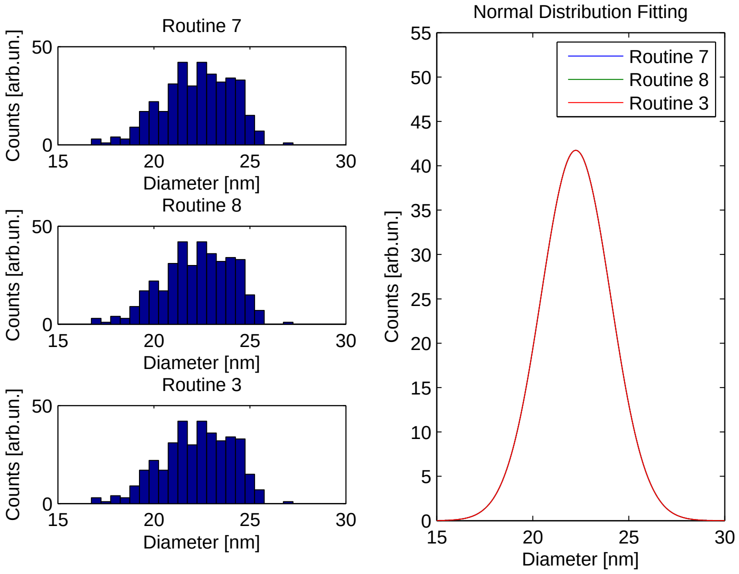

Figure 5.5: Histograms and normal distributions fitting of diameters for routine 7, 8 and 3.

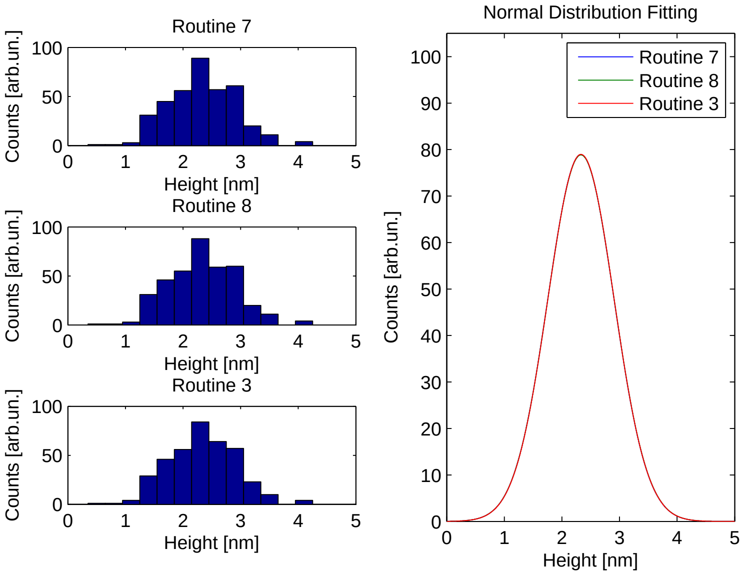

Figure 5.6: Histograms and normal distributions fitting of heights for routine 7, 8 and 3.

In conclusion, background subtraction likely reduces the heights and the diamaters of the QDs if they are not excluded from this action. It can therefore slightly modify the sizes of the nanostructers imaged. Moreover. background subtraction, regardless which degree polynom used, if performed excluding the grains does not affect the original data. It is just a way to flatten the background.

5.4.2 Surface reconstruction

In Fig. 5.7 and 5.8 the consequence of surface reconstruction on the diameters is shown, while in Fig. 5.9 and 5.10 this action is analysed taking into account the heights. In routine 2 and 5 the background subtraction is carried out including the QDs, while in routine 3 and 4 excluding the region under the mask. Afterwords, for routine 4 and 5 surface reconstruction is applied. In Fig. 5.11 is also shown an example of tip estimation output.

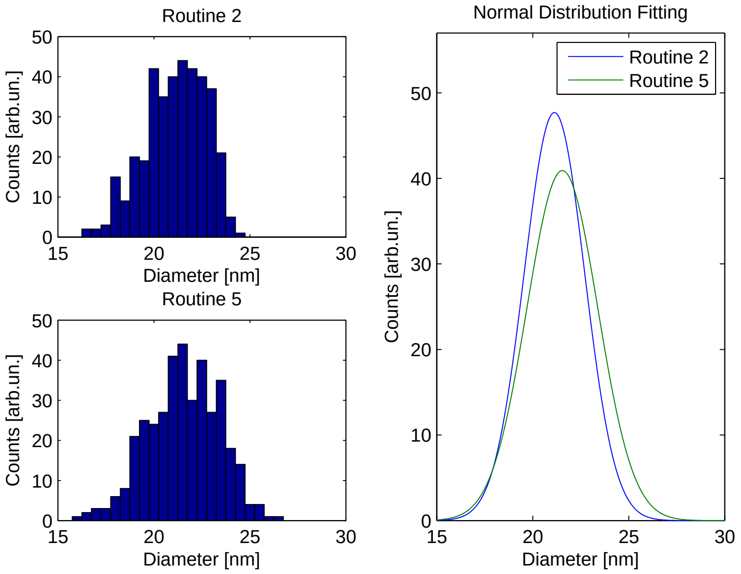

Figure 5.7: Histograms and normal distributions fitting of diameters for routine 2 and 5.

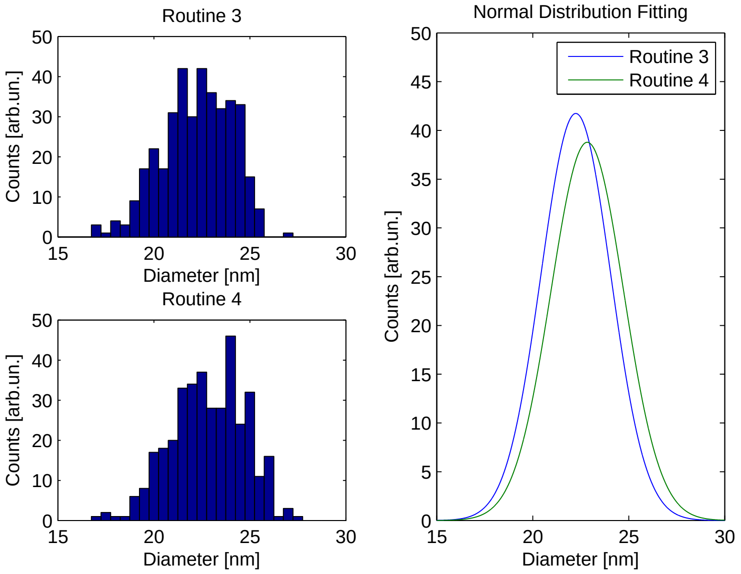

Figure 5.8: Histograms and normal distributions fitting of diameters for routine 3 and 4.

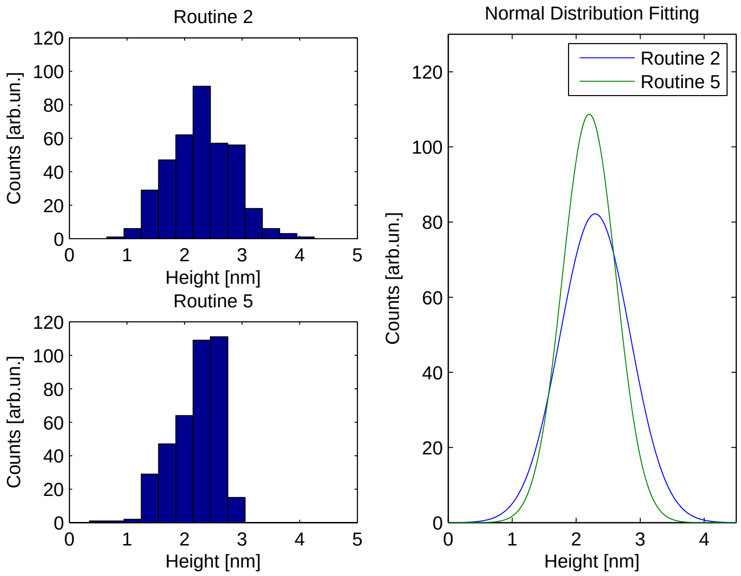

Figure 5.9: Histograms and normal distributions fitting of heights for routine 2 and 5.

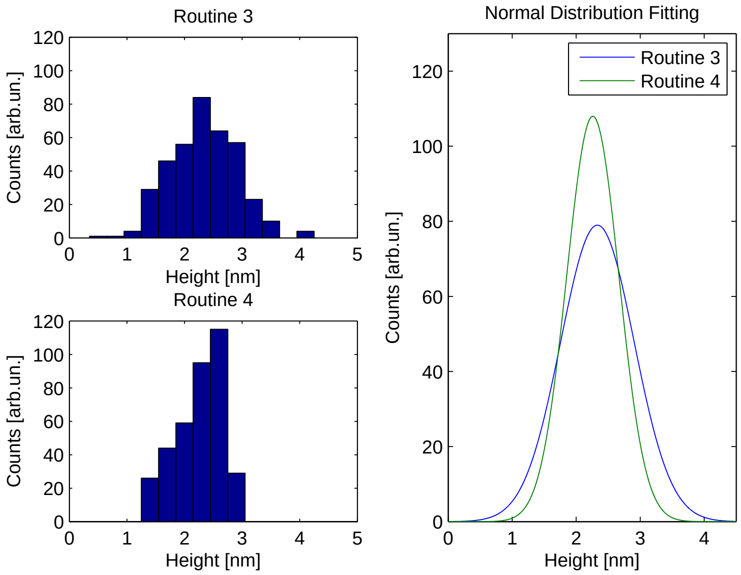

Figure 5.10: Histograms and normal distributions fitting of heights for routine 3 and 4.

The most remarkable effects are the slighlty decrease in mean height (∼4.5%) and the narrowing of the normal distribution fitting for heights (∼20.5%). The diameters, instead, have the opposite trend; the mean increases of about 1.8-2.6% and the normal distributions broaden. The amount of this broadening is quite different looking at the two different routines involved in surface reconstruction, routine 4 and 5. The latter, that involves background subtraction including QDs, leads to a FWHM of normal distribution larger of 17% than the one in routine 2, while for the former, that excludes QDs from the subtraction, the broadening is smaller (∼5%).

Then, surface reconstruction contributes to reduce the mean height and narrow its normal distribution, while regarding the diameters, the mean value is larger and the distribution is broader.

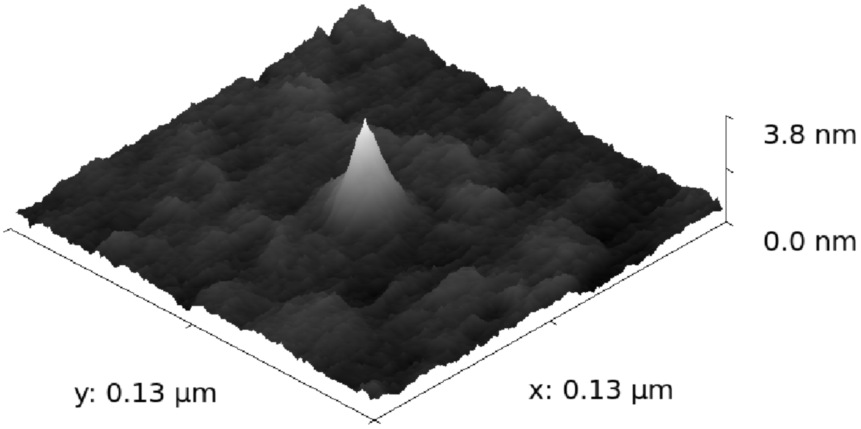

Figure 5.11: Example of blind tip estimation output, 3D view.

5.4.3 Low pass filtering

The last comparison that was analyzed is between routine 3 and 6, in order to check the effect of low pass filtering as shown in Fig. 5.12 and 5.13.

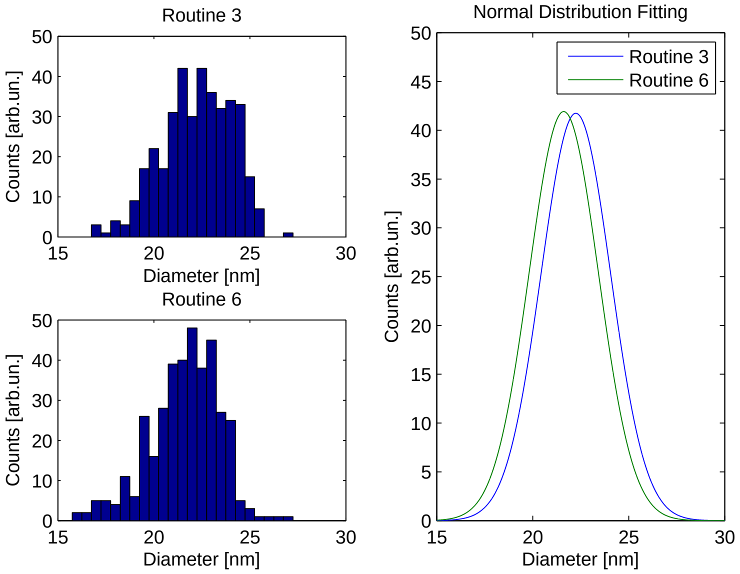

Figure 5.12: Histograms and normal distributions fitting of diamteres for routine 3 and 6.

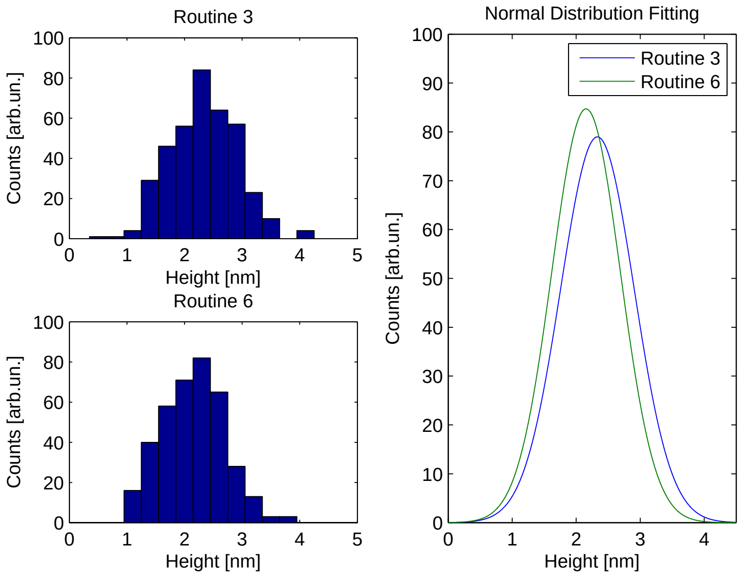

Figure 5.13: Histograms and normal distributions fitting of heights for routine 3 and 6.

Low pass filtering the image leads to a reduction of either the mean height (~4.5%) and mean diameter (~2.7%), keeping FWHMs unchanged.
This operation is helpful and logically necessary because the noise in the image has mainly an high frequency contribution.

5.5 Image processing: final routine

The evaluation of the image processing showed in the previous sections has been necessary in order to understand and quantify the effect that every single step in the processing will have on the original image. The final routine chosen for the analysis of all the samples grown by MBE is a suitable and logically ordered sequence of operation that can be performed by Gwyddion.
The final routine is the following:

- Correct lines
- Correct horizontal scars
- Mark grains
- Remove polynomial background (horizontal polynom degree 3$^{\text{rd}}$ and vertical polynom degree 3$^{\text{rd}}$, excluding region under mask)
- Blind tip estimation, run partial
- Surface reconstruction
- Low pass filtering (2D FFT filtering)
- Mark grains in the deconvoluted and filtered image

- Extract raw data

Finally, the estimated errors for density, mean diameter and mean height are 3.5%, 7.5% and 4.5% respectively.

Chapter 6

Results and discussion

In this chapter the results of this study are shown and discussed. In section 6.1, the results are presented, while the dependence of sizes and density of QDs on growth temperature, InAs thickness, As flux, growth rate and In:As flux ratio are discussed in section 6.2, 6.3, 6.4, 6.5 and 6.6, respectively.

6.1 Presentation of results

The 14 samples grown by MBE are presented in chapter 4, Tab. 4.1. The central part of the samples was cut and AFM images were taken at different magnification (1x1 μm^2, 500x500 nm^2 and 200x200 nm^2).
The best images are shown in Appendix A.
Then, the 500x500 nm^2 images were analyzed using Gwyddion 2.13, by means of the image processing routine described in chapter 5. The raw data extracted after the processing were elaborated using MATLAB®'s codes attached in Appendix B.
In Tab. 6.1 and 6.2 the results are displayed. In Tab. 6.1, the densities and the amount of material incorporated in the QDs, expressed in equivalent monolayer (MLeq), are shown, while in Tab. 6.2, the average heights and diamaters as well as the corresponding FWHMs are pointed out. The zeros in both tables express the impossibilty of getting any quantitative results from the images. This is due not because the routine or the program is unable to do that, but simply because the samples theirselves do not show any proper QDs in the surface, as it will be discussed later in the chapter.

Sample	Density $[10^{11}\ \mathrm{cm}^{-2}]$	MLeq [ML]
541-1	1,85	0,52
541-2	0	0
541-3	2,74	0,41
541-4	0	0
542-1	0	0
542-3	0	0
542-4	0	0
543-1	1,44	1,71
543-2	1,46	1,1
543-3	1,48	1,13
544-1	1,71	1,05
544-2	1,56	1,56
547-1	1.97	0,6
547-2	1,79	0,7

Table 6.1: Results: the densities and the amount of material incorporated in the QDs, expressed in equivalent monolayer (MLeq), are shown .

Sample	Mean Height [nm]	FWHM Height [nm]	Mean Diameter [nm]	FWHM Diameter [nm]
541-1	1.1	0,71	22,1	8,48
541-2	0	0	0	0
541-3	0,8	0,59	17,3	6,59
541-4	0	0	0	0
542-1	0	0	0	0
542-3	0	0	0	0
542-4	0	0	0	0
543-1	3,2	1,88	24,6	8,01
543-2	2,2	1,18	23,1	6,83
543-3	2	0,94	21,2	4
544-1	1,8	0,94	22,8	8,24
544-2	2,7	2,12	24,6	8,24
547-1	1,1	0,71	21,1	5,56
547-2	1,4	1,06	22,9	6,83

Table 6.2: Results: the mean heights and diameters as well as the corresponding FWHMs are shown.

6.2 Dependence on growth temperature

Fig. 6.1 shows 1x1 μm^2 AFM images of samples growth at temperatures ranging from 360 to 480°C (2.0 ML InAs, 2x10^{-6} Torr As flux and 0.09 ML/s growth rate).
The only sample that clearly displayes QDs is the one at 480°C, while for the other temperatures, just some coalescence is visible.

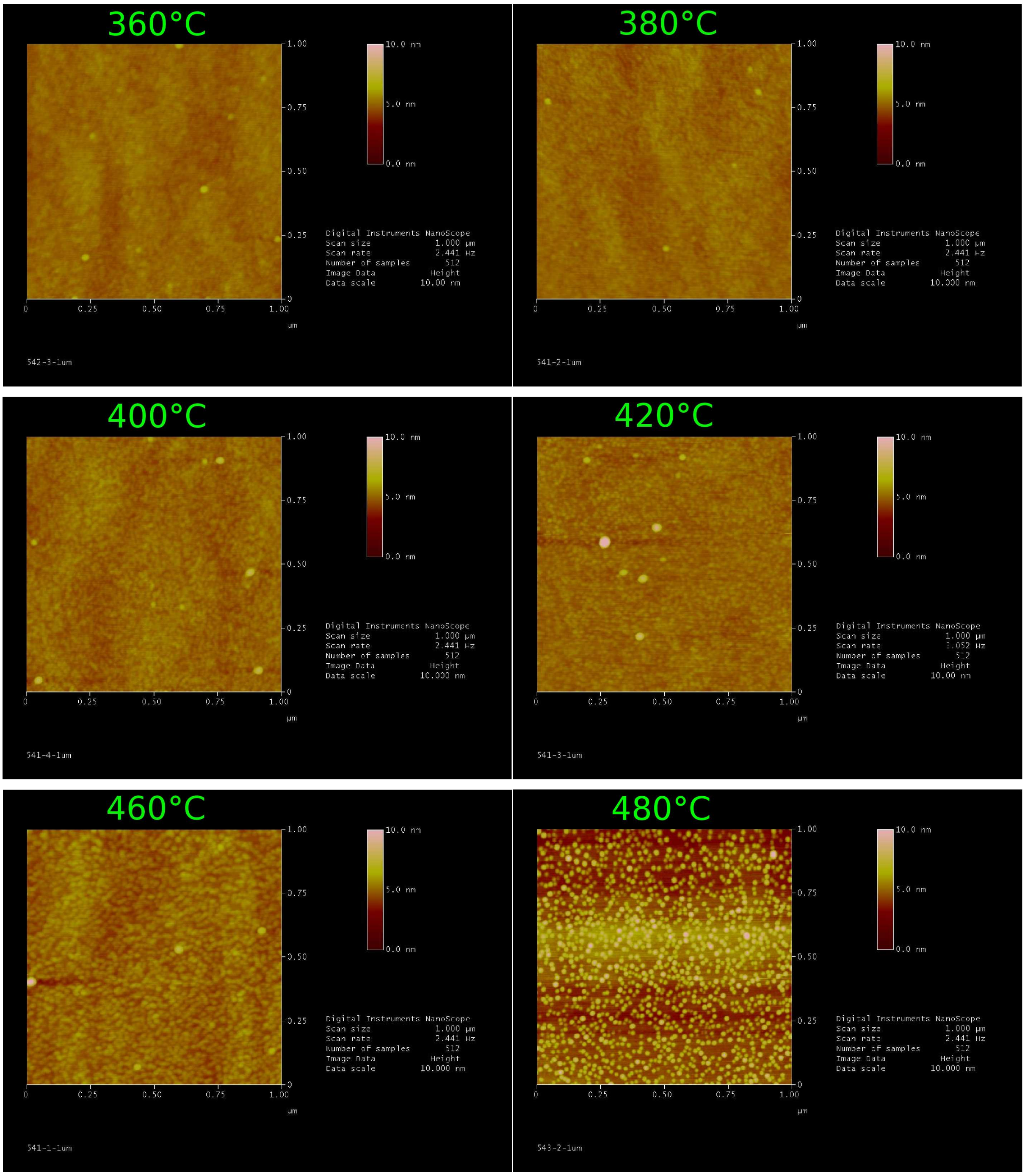

Figure 6.1: 1x1 μm^2 top view AFM images of 2.0 ML InAs, 2x10^{-6} Torr As flux and 0.09 ML/s growth rate, grown at different temperatures.

In order to have a quantitative description of the surfaces, height profiles of samples were taken, as shown in Fig. 6.2. To make the comparison easier, where possible, coalescent dot was included in the profile.
Up to 400°C, the profiles show mounds around 0.5 nm high that made any quantitative analysis impossible. These is a feature of rough surfaces that can hardly be classified as QDs.
Proper QDs show up at 420°C, 460°C and definitely at 480°C.

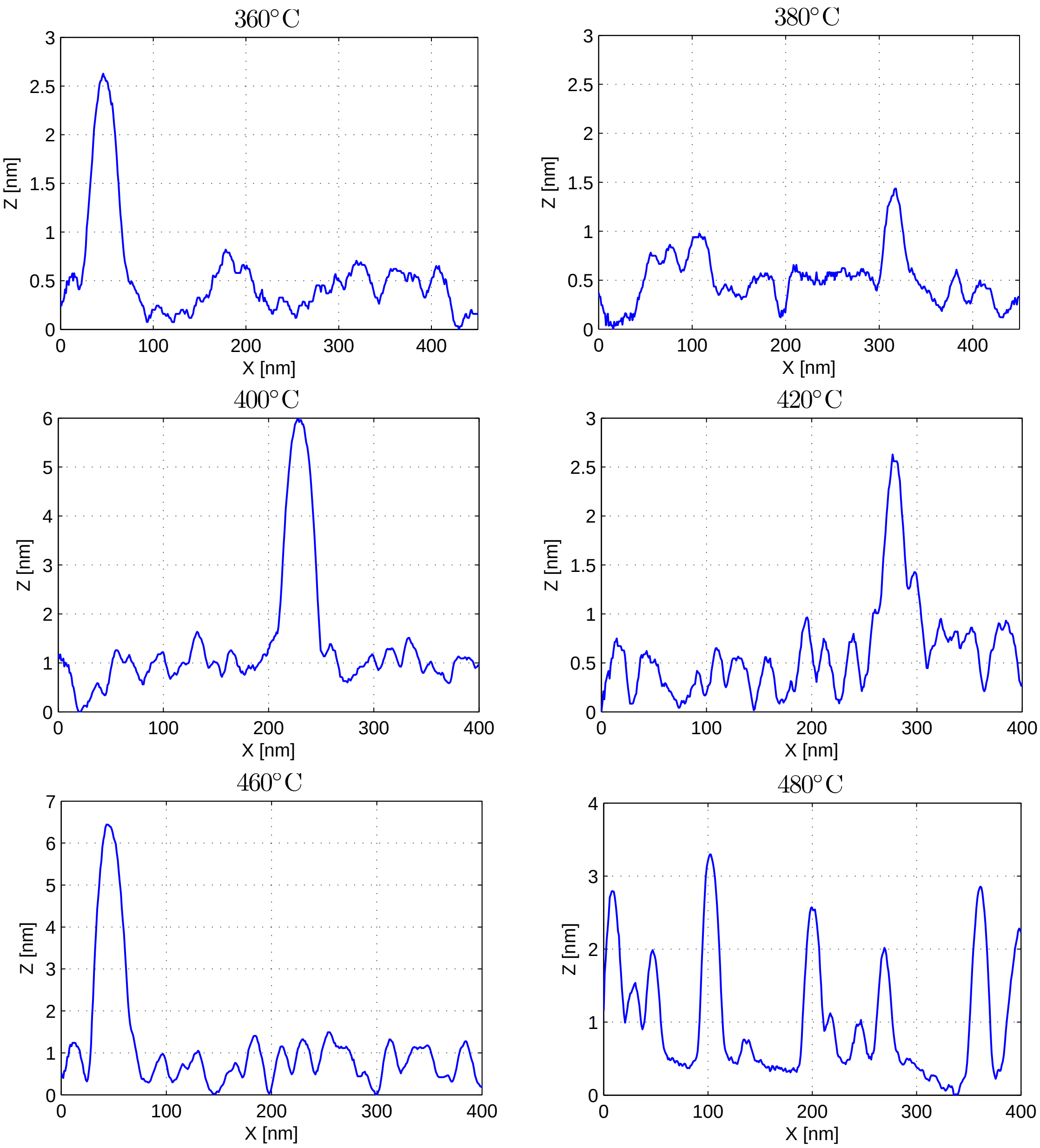

Figure 6.2: Surface profiles of samples of 2.0 ML InAs, 2x10^{-6} Torr As flux and 0.09 ML/s growth rate, grown at different temperatures.

In Fig. 6.3, the density, mean diameters and mean heights are plotted.
Once the QDs are formed, increasing the temperature leads to a decrease in density, while the mean diameter increases. These trends are in agreement with several previous studies

(e.g. [32], [33]). The formation of fewer but larger QDs at a higher substrate temperature can be explained by an increase of the surface diffusion length of adatoms with increasing substrate temperature. If the migration length increases, the adatoms will reach nucleation centers already formed, making these larger.

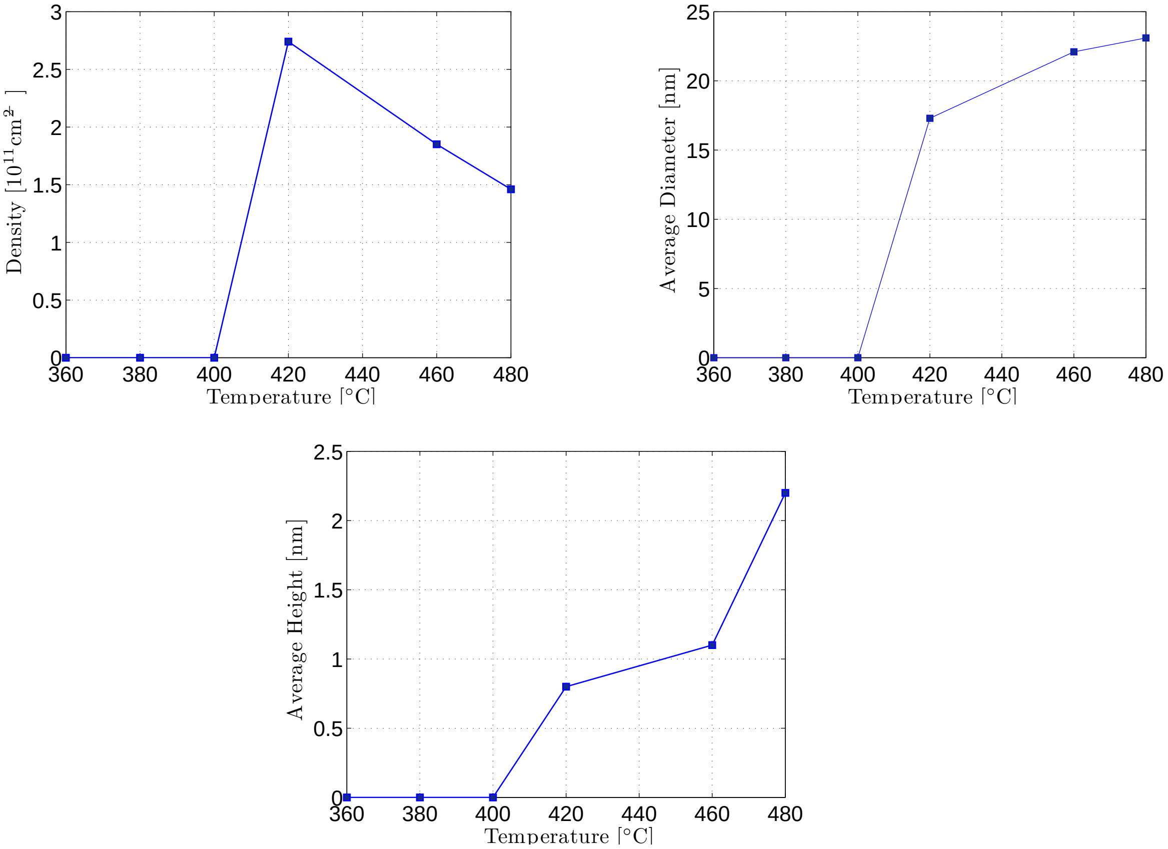

Figure 6.3: Density, mean diameter and mean height of QDs growth at different temperatures.

But, contrary to Cherkashin *et al.* [34] also the heights are increasing and, as a consequence, the volume of the QDs expresses in MLeq is increased (not shown). However, this result is in agreement with the model of self-limited growth in the SK model, which predict increasing island volume with rising T, due to a high coefficient of surface diffusion of adatoms and a weaker effect of the diffusion barriers at higher T.

Moreover, in Fig. 6.4, it is shown the *coefficient of variation* (CV) of the normal distibutions of heights and diameters. It is defined as:

$$CV = \frac{\sigma}{\mu}\text{x}100 \tag{6.1}$$

where σ is the standard deviation while μ is the mean value of the distribution. It represents the percentage broadening of the normal distribution with respect to the mean value. It is a useful parameter when we want to compare distributions which have different mean values. Both the CVs follow the same trend: they decrease increasing the temperature.

Therefore, although at lower temperature the QDs density is higher, the very small sizes of the nanostructures might be not so effective for creating the intermediate band in the solar cell because the quantum confinement required could be hardly manifested. In addition, the higher CVs make 420°C not a suitable temperature for growing IBSC, keeping the other growth parameters constant, because the distribution of size should be as narrow as possible. From this perspective, 480°C could be suitable for that purpose, having a good compromise between density and broadening and likely also the quantum confinement required.

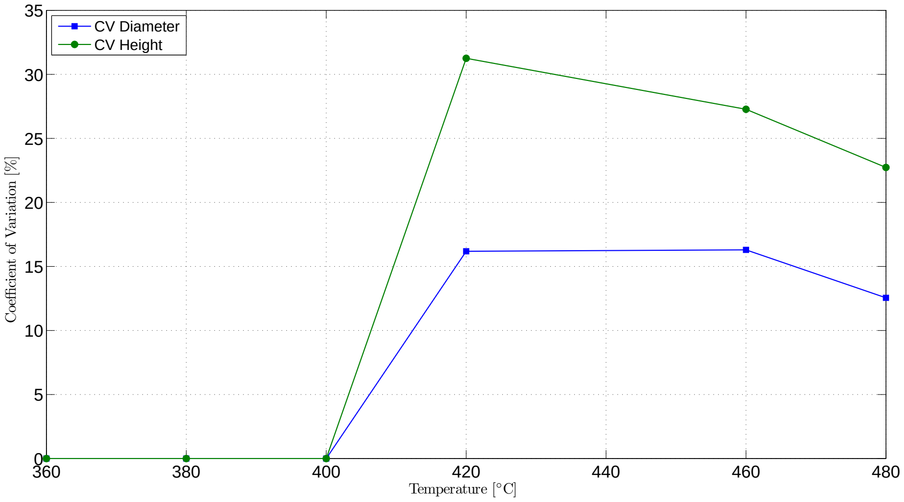

Figure 6.4: Coefficient of variation of diameters and heights at various growth temperatures.

6.3 Dependence on InAs thickness

In Fig. 6.5, 1x1 μm^2 top view AFM images of samples grown varying the InAs amount deposited are shown. Two different series are considered, the first at 380°C substrate temperature and the second at 480°C.

Increasing the amount of InAs deposited, leads to big InAs cluster formation for both substrate temperatures. This result has already been demonstrated by, e.g., Zhou *et al.* [33] and here it is further strengthen. But for the lower temperature no coherent dots are present while for the higher temperature it is possible to analyse quantitatively the fully developed dots.

In Fig: 6.6 the dependence of density, mean diameter and mean height on the amount of InAs deposited is depicted, for 480°C substrate temperature.

A clear turning point is visible at 2.2 ML. The density increases and, after this point, it starts to decrease. The opposite trend is revealed by the sizes: the mean diameter and height display a minimum at 2.2 ML. We believe that this behavior could be caused by the self-limiting size effect. This hypotesis is further strengthen by the data in Fig. 6.7. It points out the amount of InAs embodied by all the QDs. Since the total InAs deposited is known, it is also possible to estimate the thickness of the wetting layer (WL).

The increase of the InAs thickness from 2 ML to 2.2 ML does not effect the *total* volume

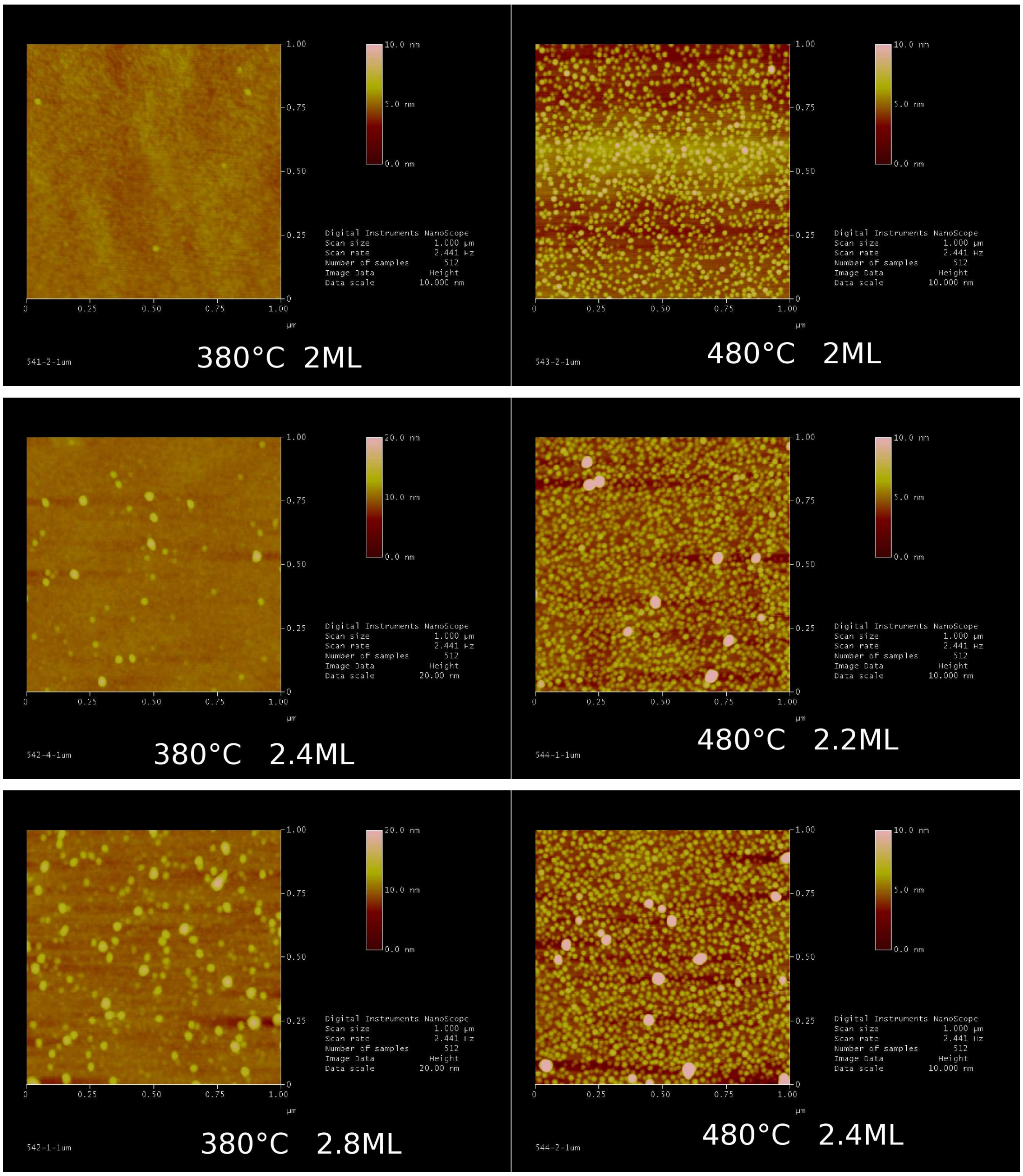

Figure 6.5: 1x1 μm^2 top view AFM images: (left column) samples grown at 380°C, 2x10^{-6} Torr As flux and 0.09 ML/s growth rate, with different InAs thicknesses; (right column) samples grown at 480°C, 2x10^{-6} Torr As flux and 0.09 ML/s growth rate, with different InAs thicknesses.

of the QDs, it is fairly constant: the decrease in the average size of the QD is balanced by an increase in the density. Therefore, the extra InAs deposited thickens the WL which increases the strain. As demonstrated by Barabási [35], the strain energy is higher at the edge of the island. This means that, if atoms are deposited near the island, strain biases their otherwise random motion, generating a net surface current that points towards the decreasing strain direction. Thus the strain field around an island generates a net current of adatoms away from the island. Moreover, for large islands the strain energy at the edge become comparable to the bonding energy of the edge atom, enhancing its detachment, thus leading to a gradual dissolution of the island. Such a mechanism favors a smaller

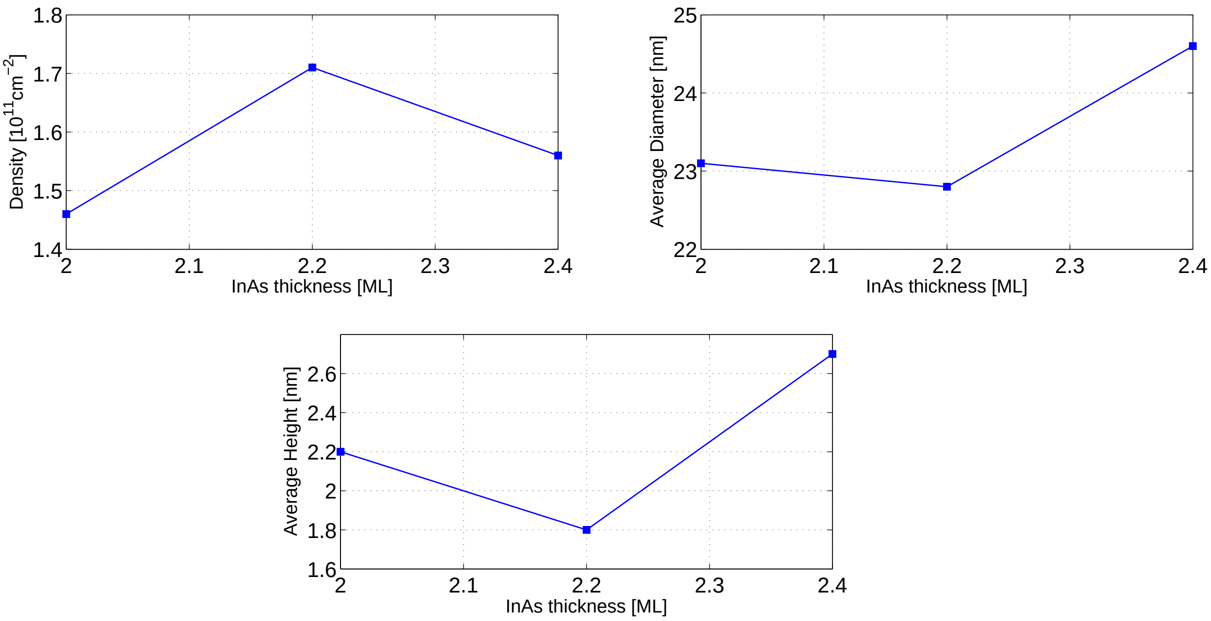

Figure 6.6: Density, mean diameter and mean height of QDs growth with different InAs thicknesses.

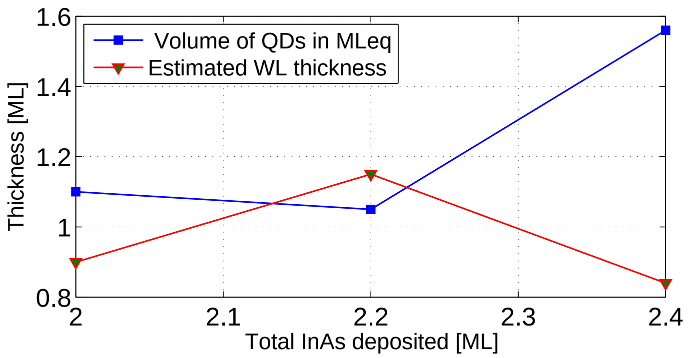

Figure 6.7: InAs amount absorbed by the QDs and thickness of the WL, depending on the total amount of InAs deposited.

average island size.

A further increase in deposition amount (2.4 ML) shows bigger QDs size and a reduced density. The total volume of InAs absorbed by the QDs, however, does not come from just the extra 0.2 ML deposited, as shown in Fig. 6.7, but also from the WL. In this case the dots erode the WL absorbing InAs from it.

To summarize, increasing InAs deposition from 2 ML to 2.2 ML leads to the self-limiting size effect. The strain reaches a threshold that triggers the detachment of the edge atoms of the QDs, reducing the average size of the QDs. Moreover, the net current flow that pushes the detached adatoms away from the already formed QDs, induces the formation of new coherent islands, increasing therefore the density number. A further increase of InAs deposited leads to a strain too high that breaks the previous balance. The strain is relaxed forming big clusters and increasing the average size of the QDs at the expense of the WL that becomes thinner.

Since for IBSC application a high QDs density and a good homogeneity is required, the best choise regarding InAs thickness seems to be 2 ML.

6.4 Dependence on As flux

In Fig. 6.8, 1x1 μm^2 top view AFM images of samples grown varying the As fluxes are shown.
At high flux, big cluster formation are induced, while at low flux better QDs homogeneity is clearly visible.

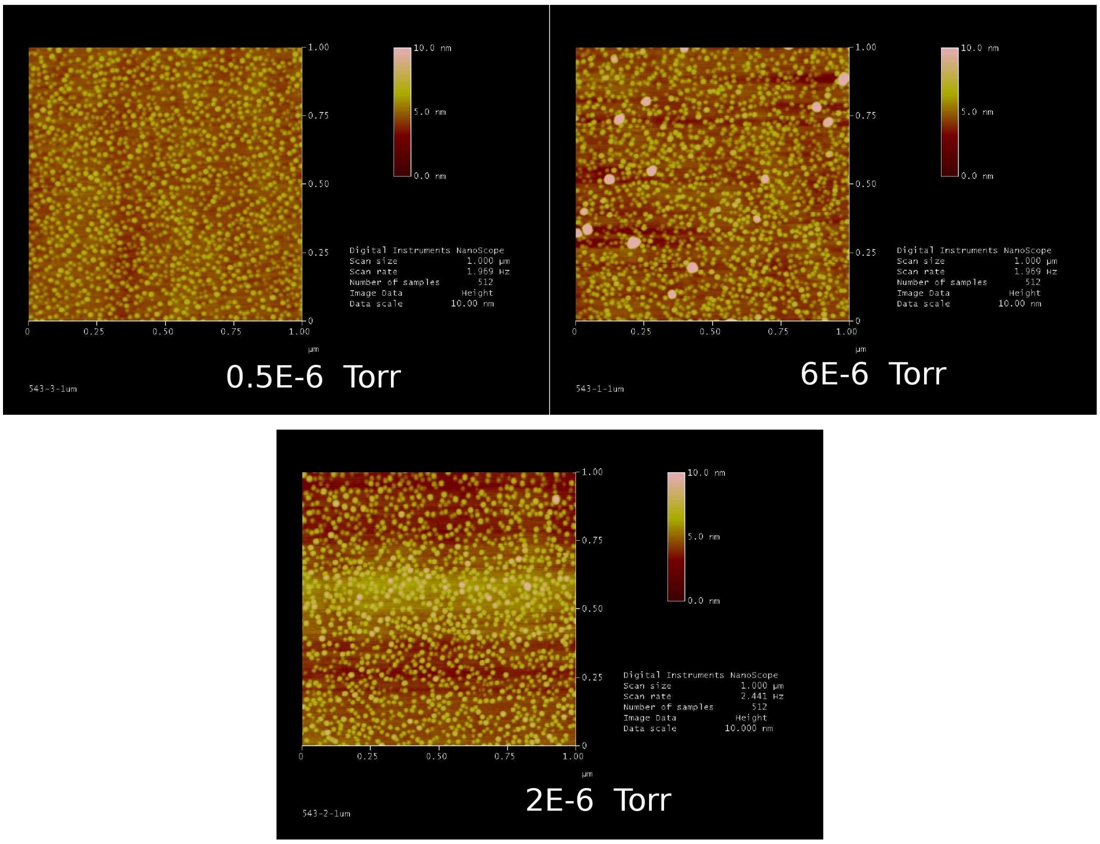

Figure 6.8: 1x1 μm^2 top view AFM images of three samples grown at 480°C, 2 ML InAs thickness, 0.09 ML/s growth rate and at different As fluxes.

In Fig. 6.9 the dependence of density, mean diameter and mean height on As flux is depicted. The density slightly decreases by increasing the flux, while the average size of the QD increases.
At low As fluxes the migration length of In adatoms increases. The adatoms can, therefore, reach many QDs, but are preferentially incorporated into smaller dots, limiting the size and narrowing its distribution, as shown in Fig. 6.10. As the As flux increases, the diffusion length diminishes and so the probability for the adatoms to be absorbed by small dots, resulting in bigger average sizes and dispersion.

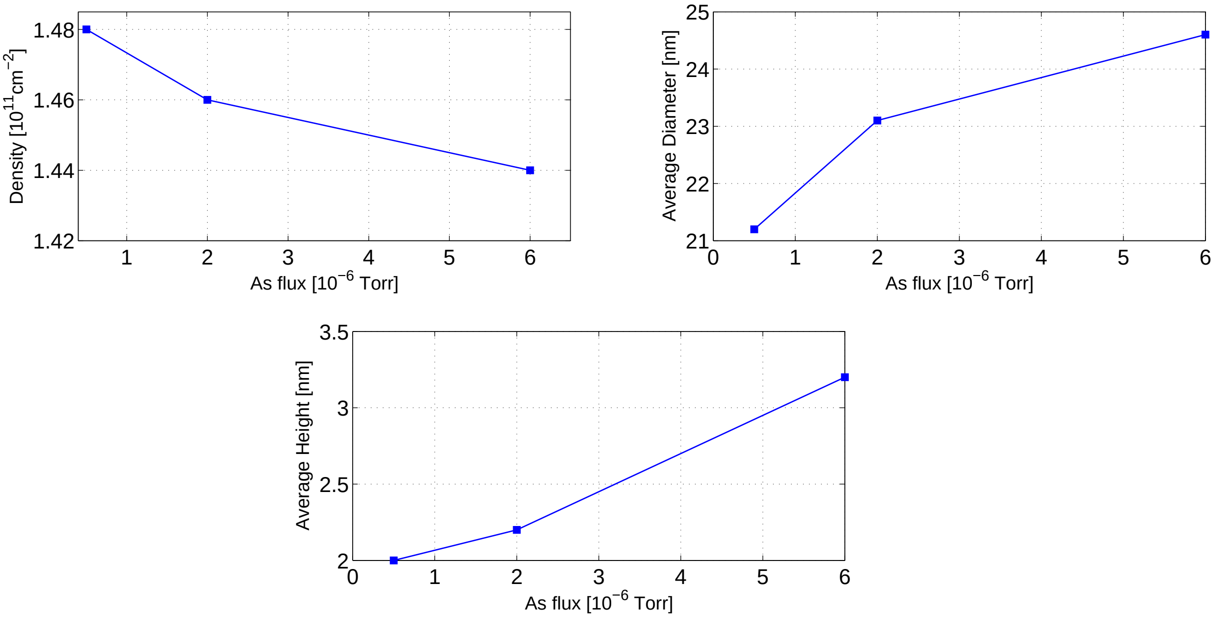

Figure 6.9: Density, mean diameter and mean height of QDs growth at different As fluxes.

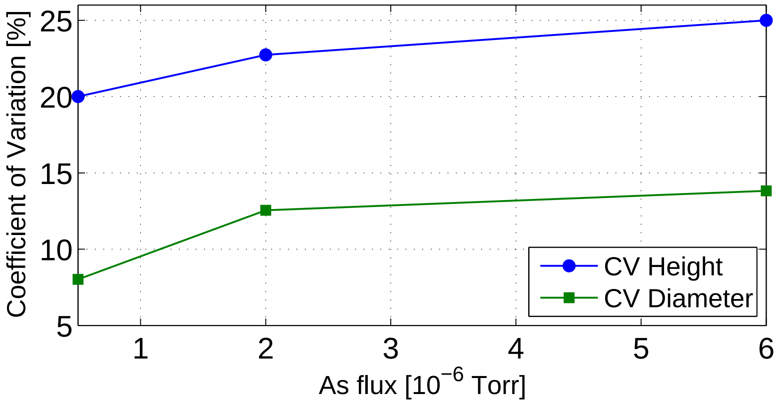

Figure 6.10: Coefficient of variation of diameters and heights depending on As flux.

Moreover, coalescent dots start to ripen, degrading the homogeneity and, therefore, the optical properties of the potential IBSC grown at this condition.
In short, low As-fluxes has to be chosen in order to manufacture homogeneous and narrow size distributed QDs.

6.5 Dependence on growth rate

In Fig. 6.11, 1x1 μm^2 top view AFM images of samples grown varying the growth rate, keeping the other parameters constant (480°C, 2.0 ML InAs, 2x10^{-6} Torr As flux), are shown.
Reducing the growth rate increases the homogeneity of the sample and coalescence is suppressed.

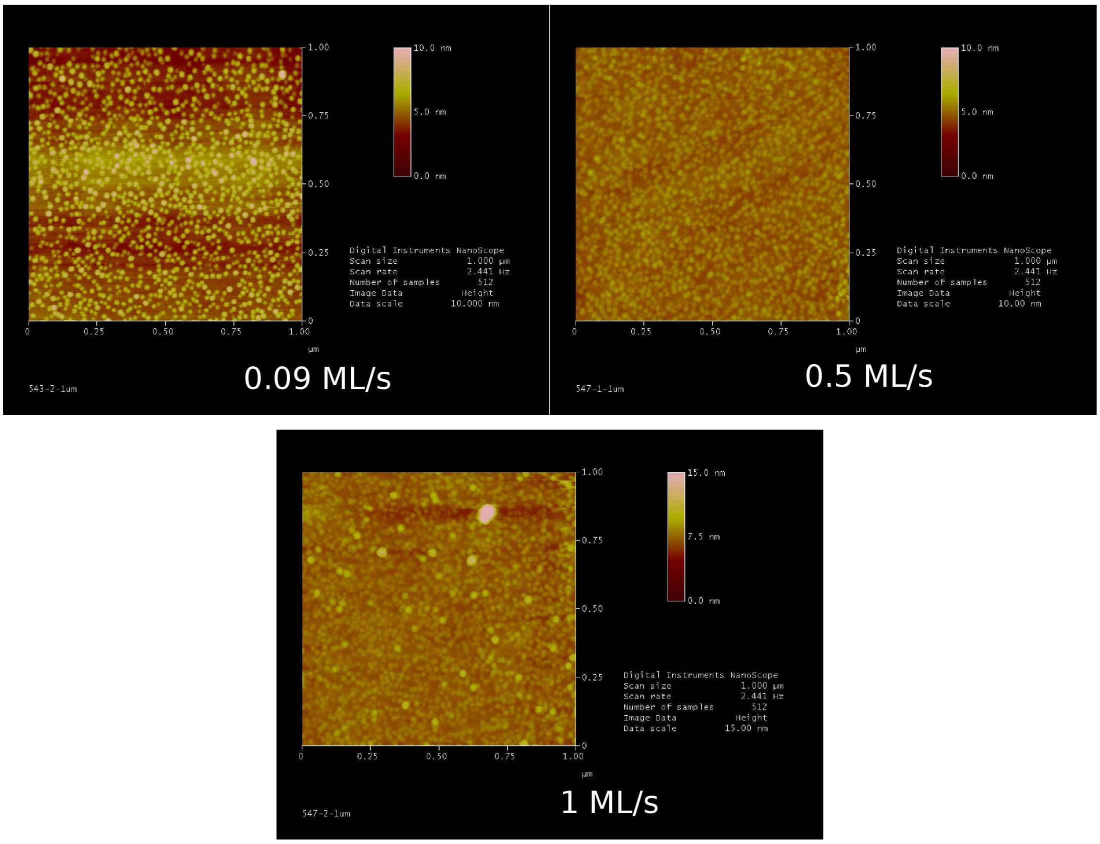

Figure 6.11: 1x1 μm^2 top view AFM images of three samples grown at 480°C, 2 ML InAs thickness, 2x10^{-6} Torr As flux and at different growth rates.

In Fig. 6.12, densities, average diameters and heights are illustrated.
At high growth rate the density increases in accordance with other reports ([32], [36]). Moreover, similarly to Chia *et al.*[37], the density seems to reach a saturation point around 1.85-1.9x10^{11} cm^{-2}. The saturation of dot density could be understood by the competition between nucleation rate and nucleation probability. With an increase in growth rate, the nucleation rate increases, leading to a high dot density. Meanwhile, the higher dot density may inhibit further nucleation of new dots since the available sites (probability) for nucletion is reduced. At a relatively lower growth rate, the first process dominates, while at a relatively higher growth rate, the first and the second processes might reach a dynamic equilibrium, resulting in dot density saturation.
Their researches have also underlined a correspondig decrease in the dot size and a narrowing of the dot lateral size distribution.
We, instead, report a slightly different behavior. The height has an overall reduction as expected, while the diameter, surprisingly, after a decrease from 0.09 ML/s to 0.5 ML/s, increases again at 1 ML/s. Moreover, as depicted in Fig. 6.13, the CV of the diameter is fairly constant in the range examined, while the CV of height increases. The unexpected trend at 1 ML/s can be understood analysing the In:As flux ratio, as it will be discussed in section 6.6. However, as already said, at high rate, big clusters are formed that makes the samples not good candidate for IBSCs. Therefore, low growth rate has to be chosen for this purpose.

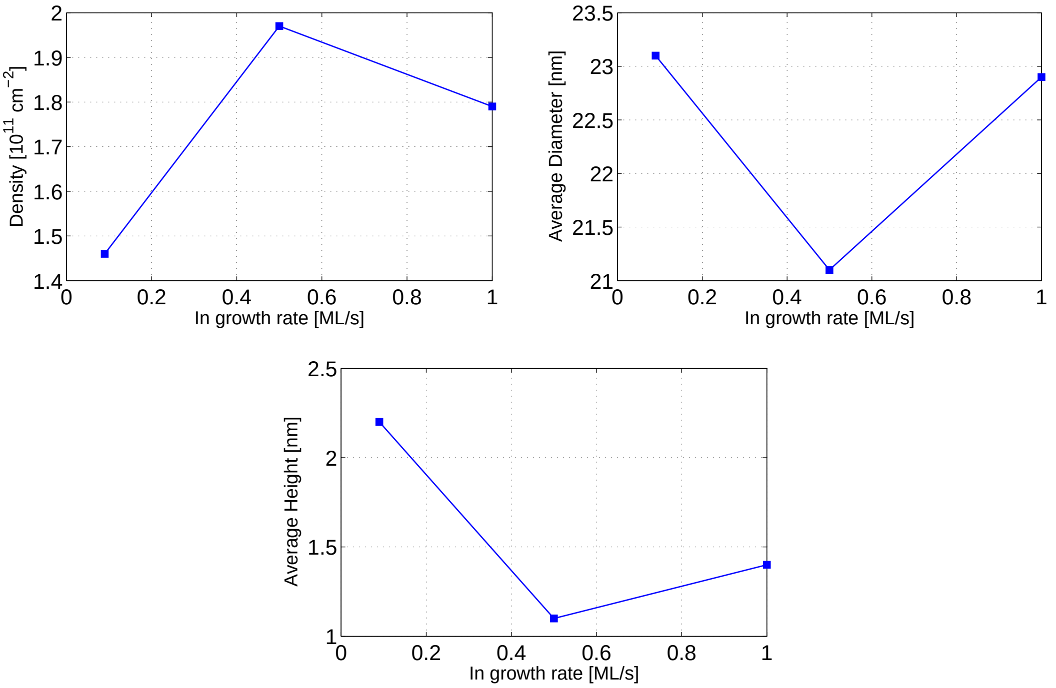

Figure 6.12: Density, average diameter and average height of QDs grown at different growth rates.

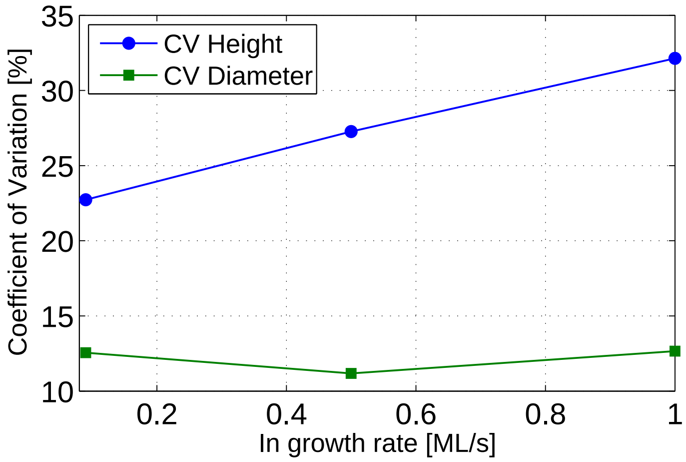

Figure 6.13: Coefficient of variation of diameters and heights depending on growth rate.

6.6 Dependence on In:As flux ratio

In this section, the last analysis performed is discussed.
In Fig. 6.14 1x1 μm^2 top view AFM images of samples grown at different III/V flux ratios are illustrated (480°C, 2.0 ML)

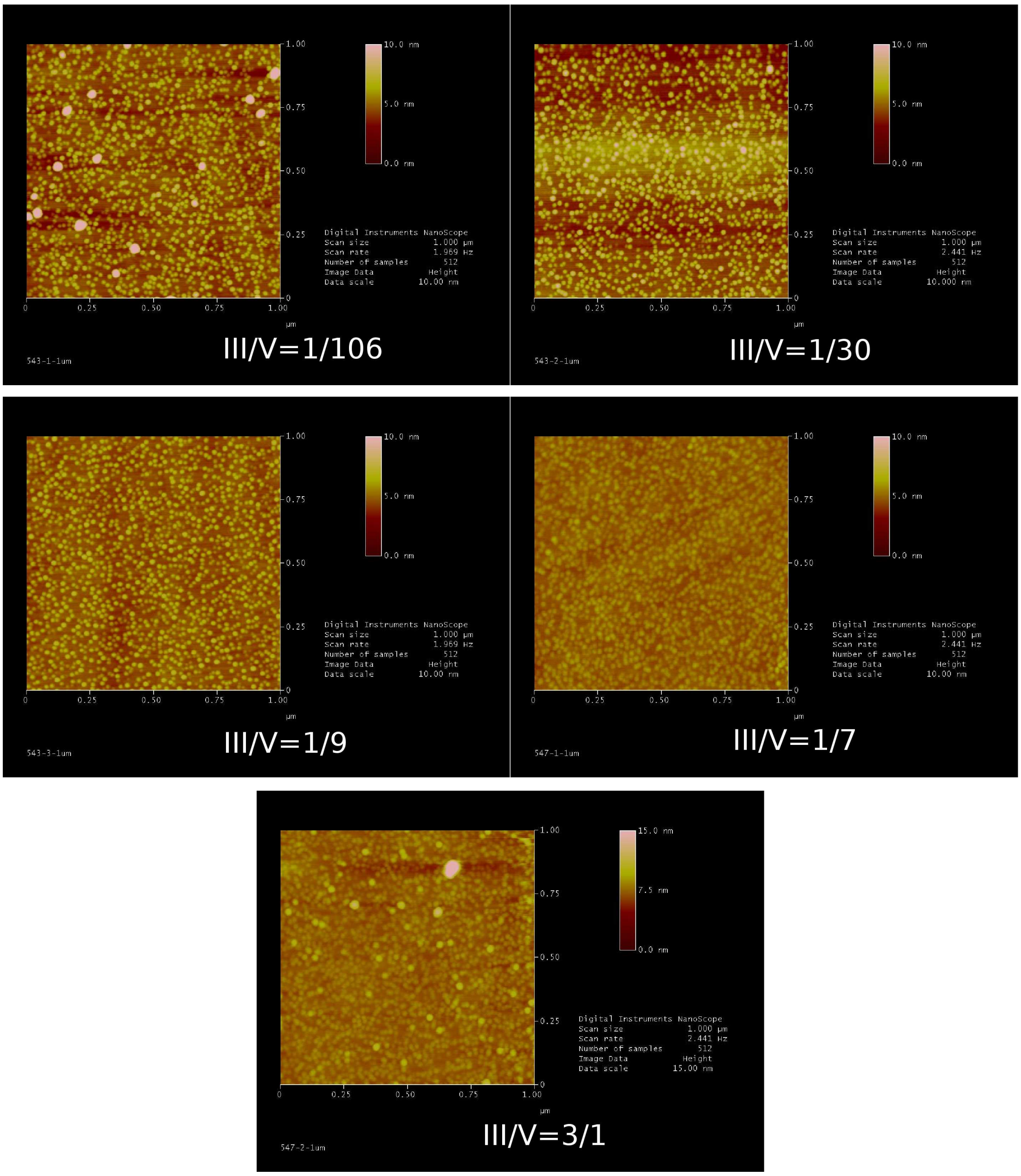

Figure 6.14: 1x1 μm^2 top view AFM images of samples grown at different III/V flux ratio.

At very high flux ratio as well as at low flux ratio, the QDs homogeneity seems compromised because of big clusters formation while at ratios ranging from 1/30 to 1/7 good homogeneity is produced.
Quantitative description of variation of QDs density and sizes depending on In:As ratio is given in Fig. 6.15. A turning point in each plot is present at In:As 1/7. Up to this point the density increases while the average size decreases. The explanation for this trend relies on the fact that increasing the III/V ratio increases the In surface migration length, thus increasing the density. Moreover, enhancing the In adatom surface diffusivity in the WL allows it to attain a more thermodinamically equilibrium state with respect to uniform strain and uniform roughening. A more uniforme strain distribution and roughened growth front will lead to a more uniform island distribution on top of the WL, therefore

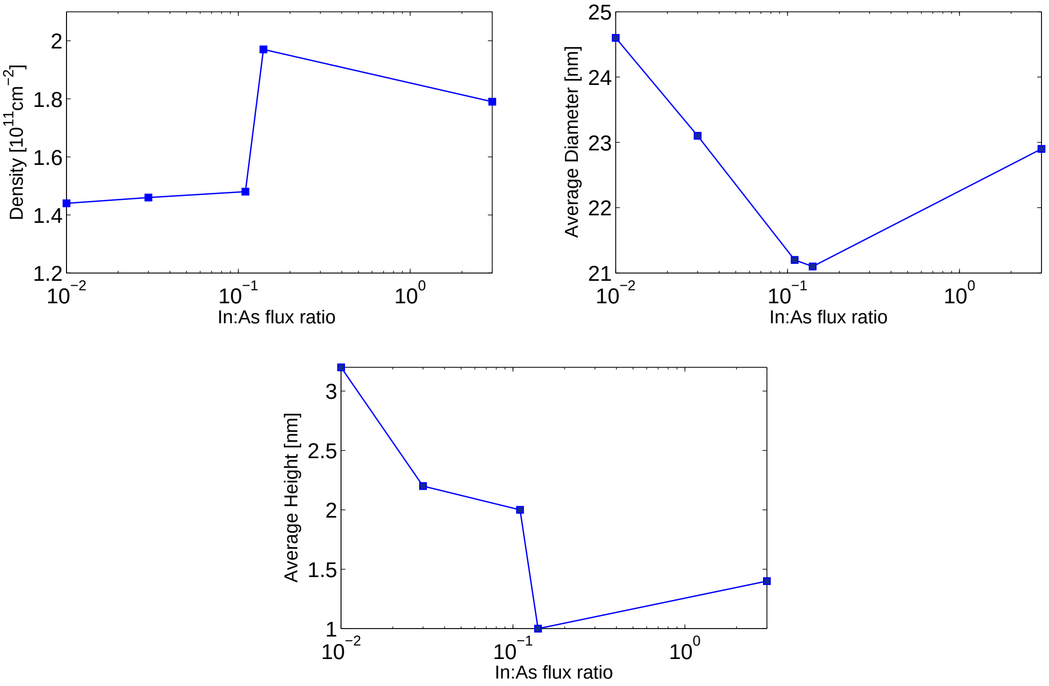

Figure 6.15: Density, mean diameter and mean height of QDs growth at different III/V ratios.

narrowing the distribution as shown in Fig. 6.16.

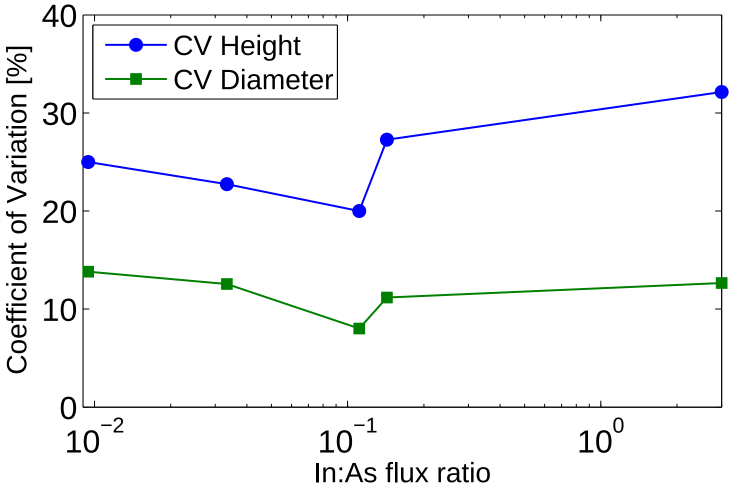

Figure 6.16: Coefficient of variation of diameters and heights depending on III/V ratio.

After the turning point at $\sim 1/7$, the density starts to decrease and the average size increases again, slighlty broadening the distribution. For that sample the ratio was equal to 3, so the In flux was three times higher than the As flux. This is the only sample of the entire serie grown at flux ratio where the In flux was higher than the As flux. At this unusual condition, the kinetic process of QDs formation is different from the normal condition In:As <1. In this regime, after a small InAs coverage, In forms a metallic layer on the GaAs buffer surface. After a certain critical thickness, in order to minimize the

strain, the Inlayer starts to ripen in drops, forming QDs with a very high In content. It is therefore probably misleading to compare ratios <1 with ratios >1. It may also be for the same qualitative reason that the dependence on the InAs growth analysed in the previous section was a little bit different from the reported ones. The sample grown at 1 ML/s is the one with In:As flux ratio 3:1.
To summarize, comparing homogeneity and quantitative data, the best choise of III/V flux ratio for IBSC application lies in the range 1/10 - 1/5, while due to speculations on the process involved in QDs formation at III/V ratio >1, the sample at III/V = 3 should not be directly compared with the other ones. In this case the growth rate dependence discussed in section 6.5 confirms the results of several other works ([32], [36] and [37]).

Chapter 7

Conclusion

The influence of the conditions during growth of InAs/GaAs quantum-dot structures on GaAs(001) by molecular-beam epitaxy has been investigated systematically with respect to achieving high quantum dot densities, homogeneity and narrow sizes distribution. The growth temperature, InAs deposit, As flux, growth rate and III/V flux ratio were varied. Atomic force microscopy and a modular program for SPM data analysis have been used to study the morphological properties of the QDs. First, the image processing has been studied in order to verify the effect that every operation has on the image. Afterward, with the routine defined, all the samples have been analysed.

Removing polynomial background from the AFM images reduces the heights and the diameters of the QDs if they are not excluded from this operation while, if they are excluded it does not affect the original data, regardless which degree polynom used. Deconvoluting the image and the AFM reduces the mean height and narrow its normal distribution, while the mean diameter increases and the distribution broadens. Moreover, low pass filtering the image does not change the FWHMs of the diameters and heights distribution while reduces the mean height and diameter.
The estimated errors for density, mean diameter and mean height has been set to 3.5%, 7.5% and 4.5% respectively.

QDs are not devepoled at temperature ranging from 360°C to 400°C. The lowest temperature at which 2D-3D transition is visible is 420°C for the growth conditions used in this work. Increasing the growth temperature to 480°C leads to a decrease in the density and an increase in the average QD size, although the distributions narrow. The result is in agreement with the model of self-limited growth in the S-K model, which predict increasing island volume increasing the temperature and, thus, the coefficient of In surface diffusion.
Increasing InAs deposition from 2 ML to 2.2 ML leads to the self-limiting size effect. The strain reaches a threshold that triggers the detachment of the edge atoms of the QDs, reducing the average size of the QDs. Moreover, the net current flow that pushes the detached adatoms away from the already formed QDs, induces the formation of new coherent islands, increasing therefore the density number. A further increase of InAs deposited leads to a strain too high that breaks the previous balance. The strain is relaxed forming big clusters and increasing the average size of the QDs at the expense of the WL

that becomes thinner.

At low As fluxes the migration length of In adatoms increases. The adatoms can, therefore, reach many QDs, but are preferentially incorporated into smaller dots, limiting the size and narrowing its distribution. As the As flux increases, the diffusion length diminishes and so the probability for the adatoms to be absorbed by small dots, resulting in bigger average sizes and dispersion. Moreover, coalescent dots start to ripen, degrading the homogeneity.

At very high flux ratio as well as at low flux ratio, the QDs homogeneity seems compromised because of big clusters formation. The sample at ratio equal to 3 is excluded from the serie because different processes than the S-K growth mode are involved in QDs formation if the In flux is higher than the As flux. Increasing the In:As flux ratio enhances the density and reduces the average QDs size, narrowing also the distributions. It relies on the fact that increasing the III/V ratio increases the In surface migration length and it allows the WL to attain a more uniform strain distribution that leads to a more uniform island distribution.

Finally, increasing the growth rate the density increases while the average size decreases. The coefficient of variation of the diameters is not affected while for the heights it increases.

Therefore the optimized growth conditions are: 480°C, 2 ML InAs deposit, 0.5x10^{-6} Torr As flux, 0.09 ML/s growth rate, leading to a III/V ratio of 1/9.

Appendices

Appendix A

AFM Images

A.1 541-1

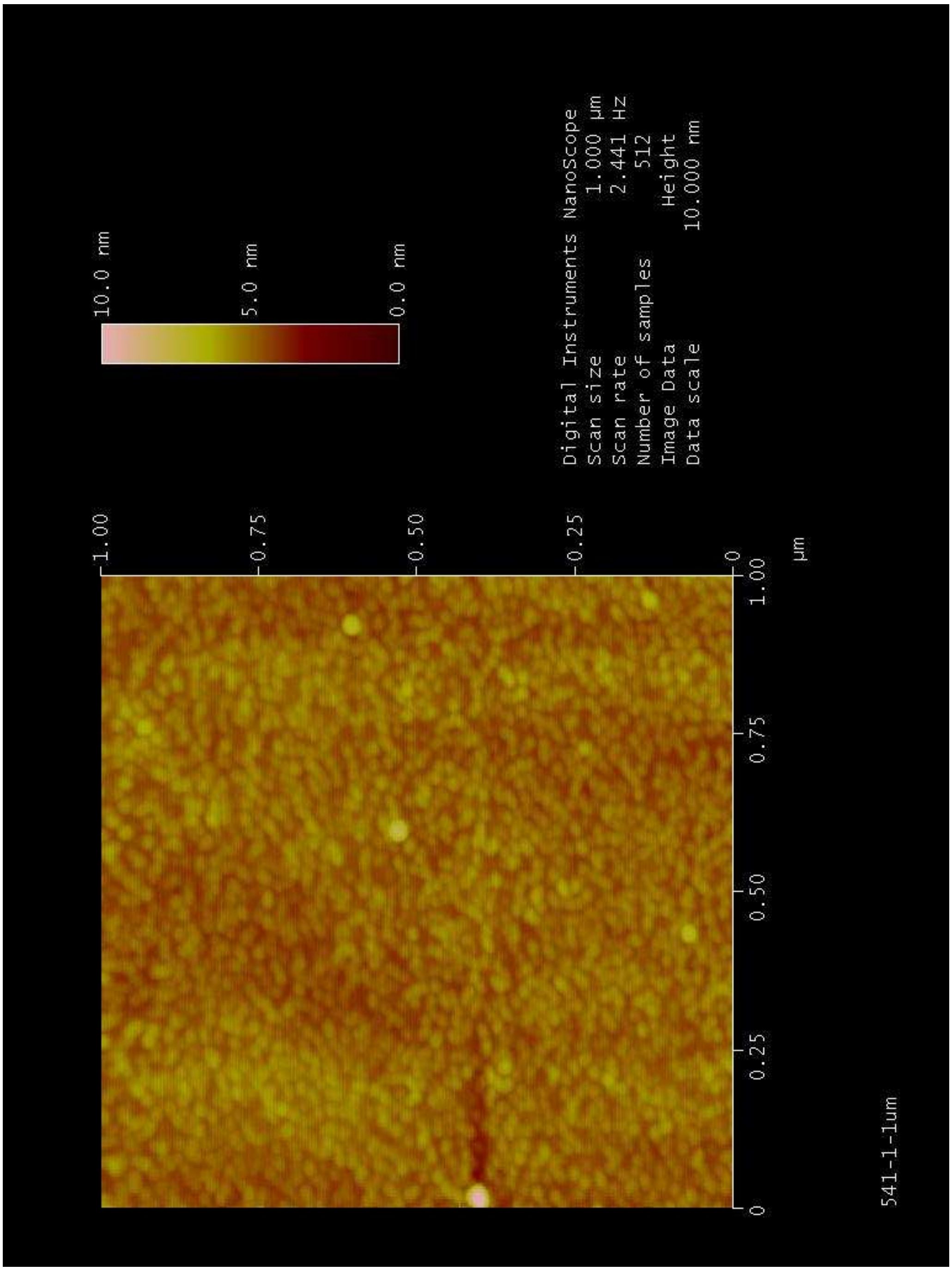
10.0 nm
5.0 nm
0.0 nm
Digital Instruments NanoScope
Scan size 1.000 µm
Scan rate 2.441 Hz
Number of samples 512
Image Data Height
Data scale 10.000 nm
1.00
0.75
0.50
0.25
0
µm
1.00
0.75
0.50
0.25
0
541-1-1um

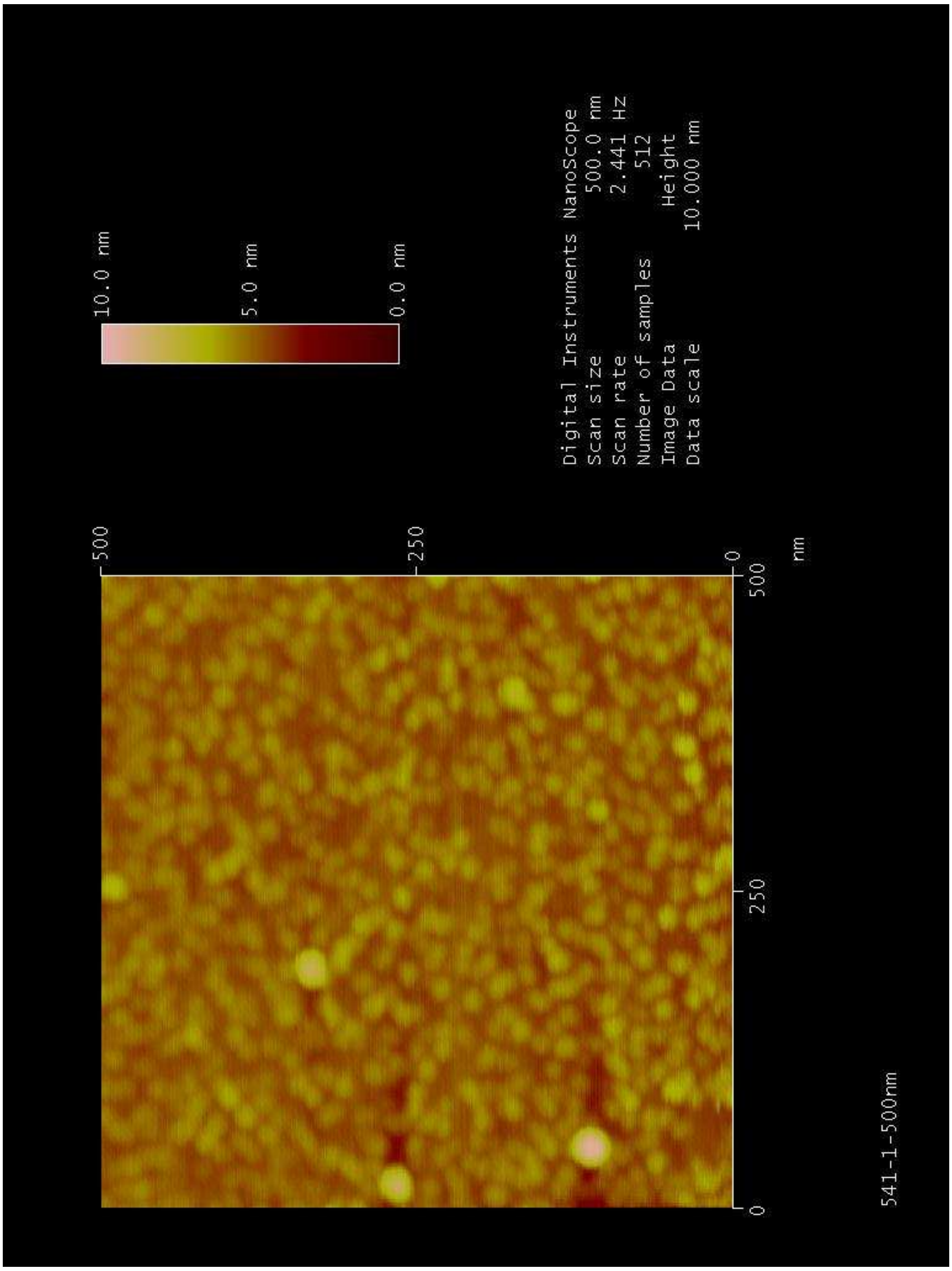
10.0 nm
5.0 nm
0.0 nm
Digital Instruments NanoScope
Scan size 500.0 nm
Scan rate 2.441 Hz
Number of samples 512
Image Data Height
Data scale 10.000 nm
500
250
0
nm
541-1-500nm

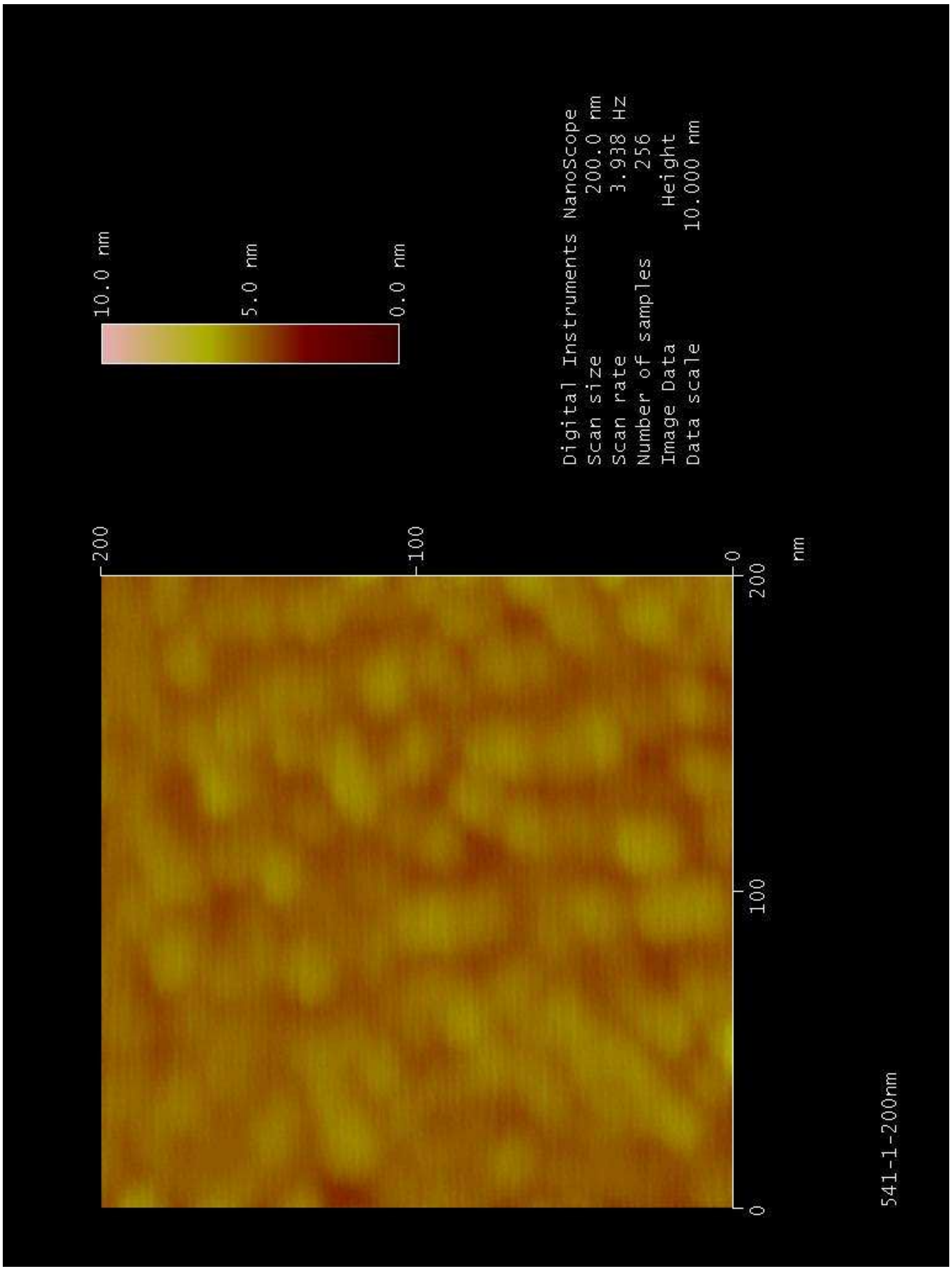

Digital Instruments NanoScope
Scan size 200.0 nm
Scan rate 3.938 Hz
Number of samples 256
Image Data Height
Data scale 10.000 nm

A.2 541-2

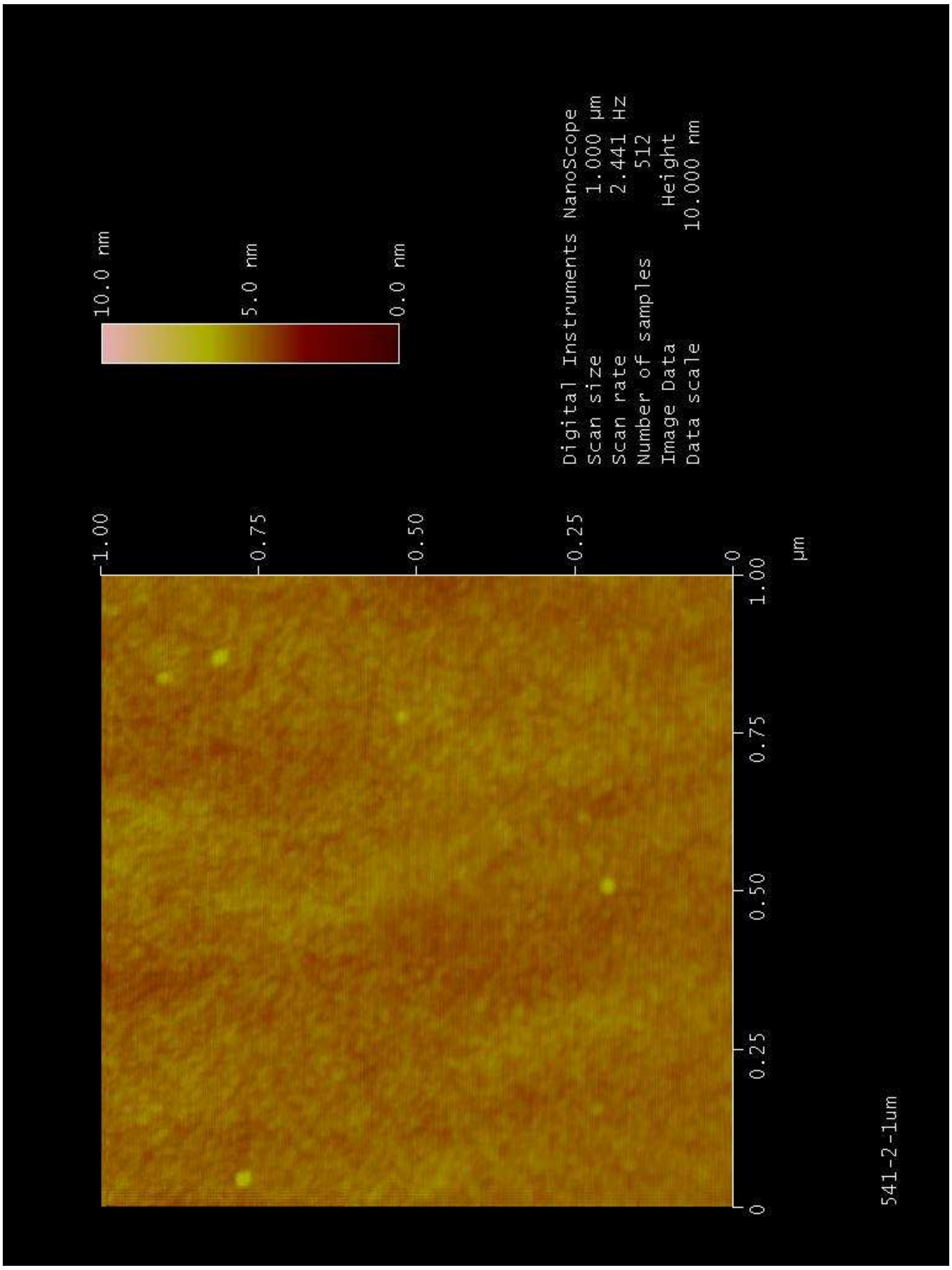
10.0 nm
5.0 nm
0.0 nm
Digital Instruments NanoScope
Scan size 1.000 µm
Scan rate 2.441 Hz
Number of samples 512
Image Data Height
Data scale 10.000 nm
1.00
0.75
0.50
0.25
0
µm
541-2-1um

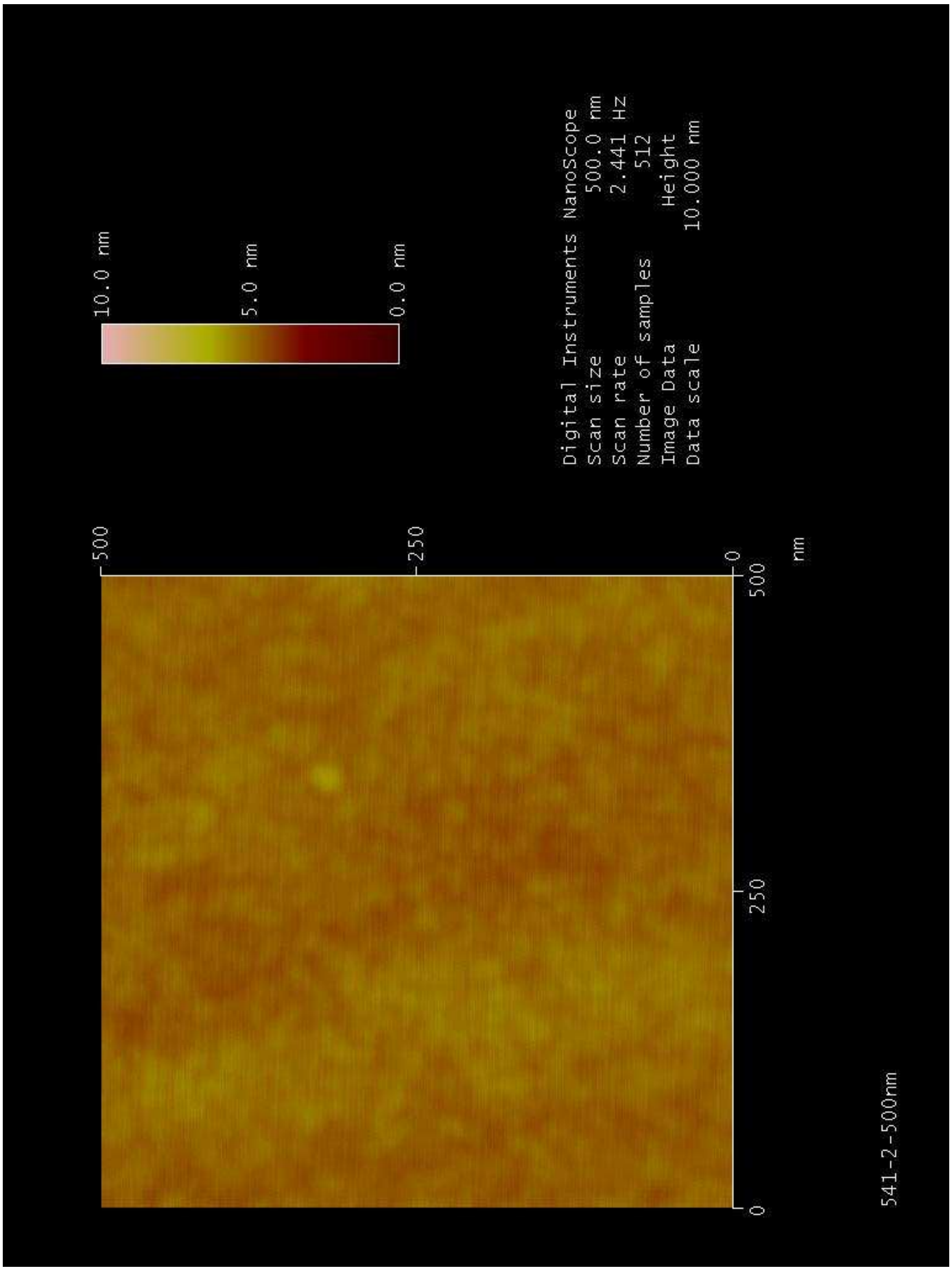
10.0 nm
5.0 nm
0.0 nm
Digital Instruments NanoScope
Scan size 500.0 nm
Scan rate 2.441 Hz
Number of samples 512
Image Data Height
Data scale 10.000 nm
500
250
0
nm
541-2-500nm

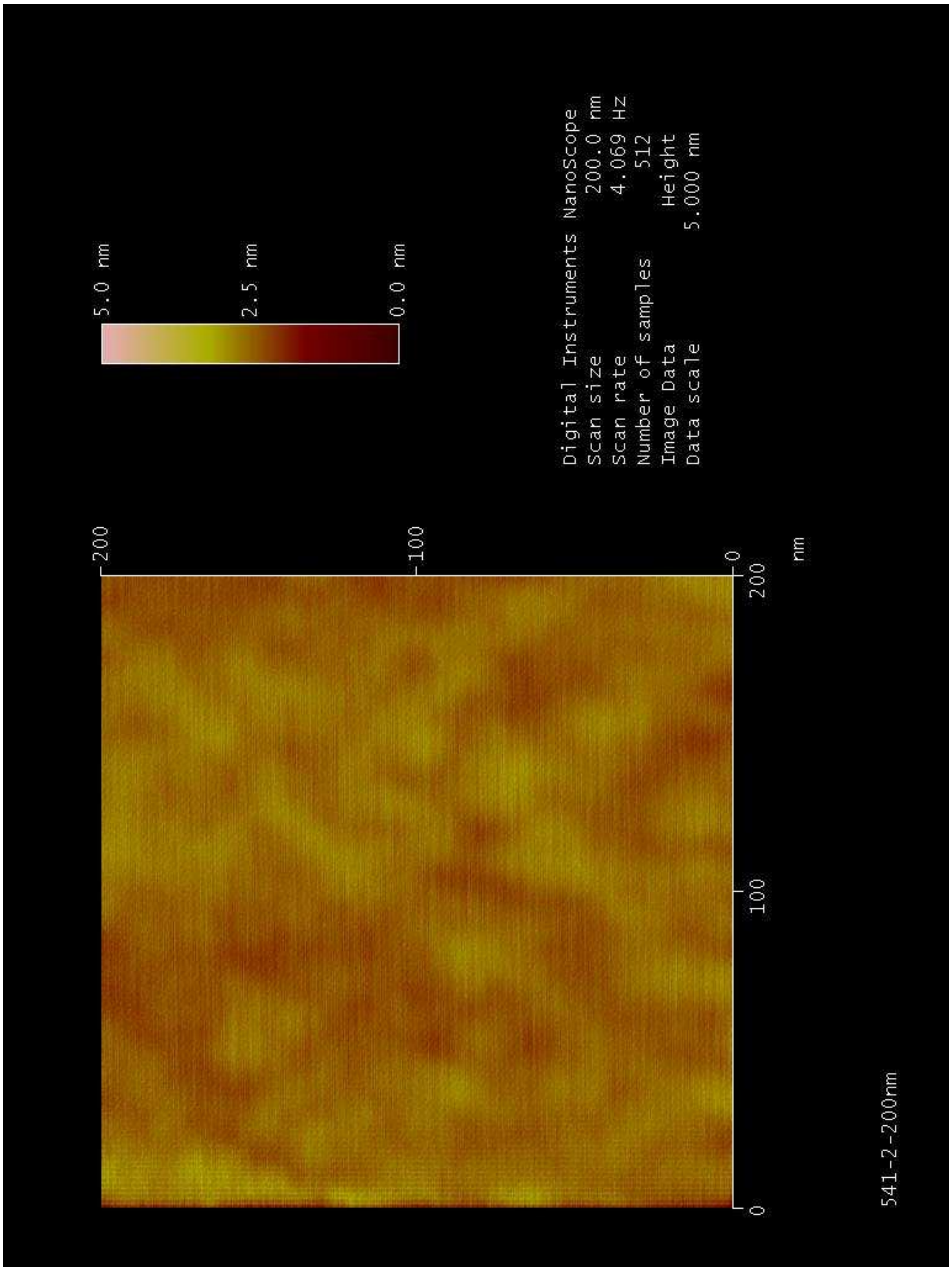
200
100
0
nm
0
100
200
5.0 nm
2.5 nm
0.0 nm
Digital Instruments NanoScope
Scan size 200.0 nm
Scan rate 4.069 Hz
Number of samples 512
Image Data Height
Data scale 5.000 nm
541-2-200nm

A.3 541-3

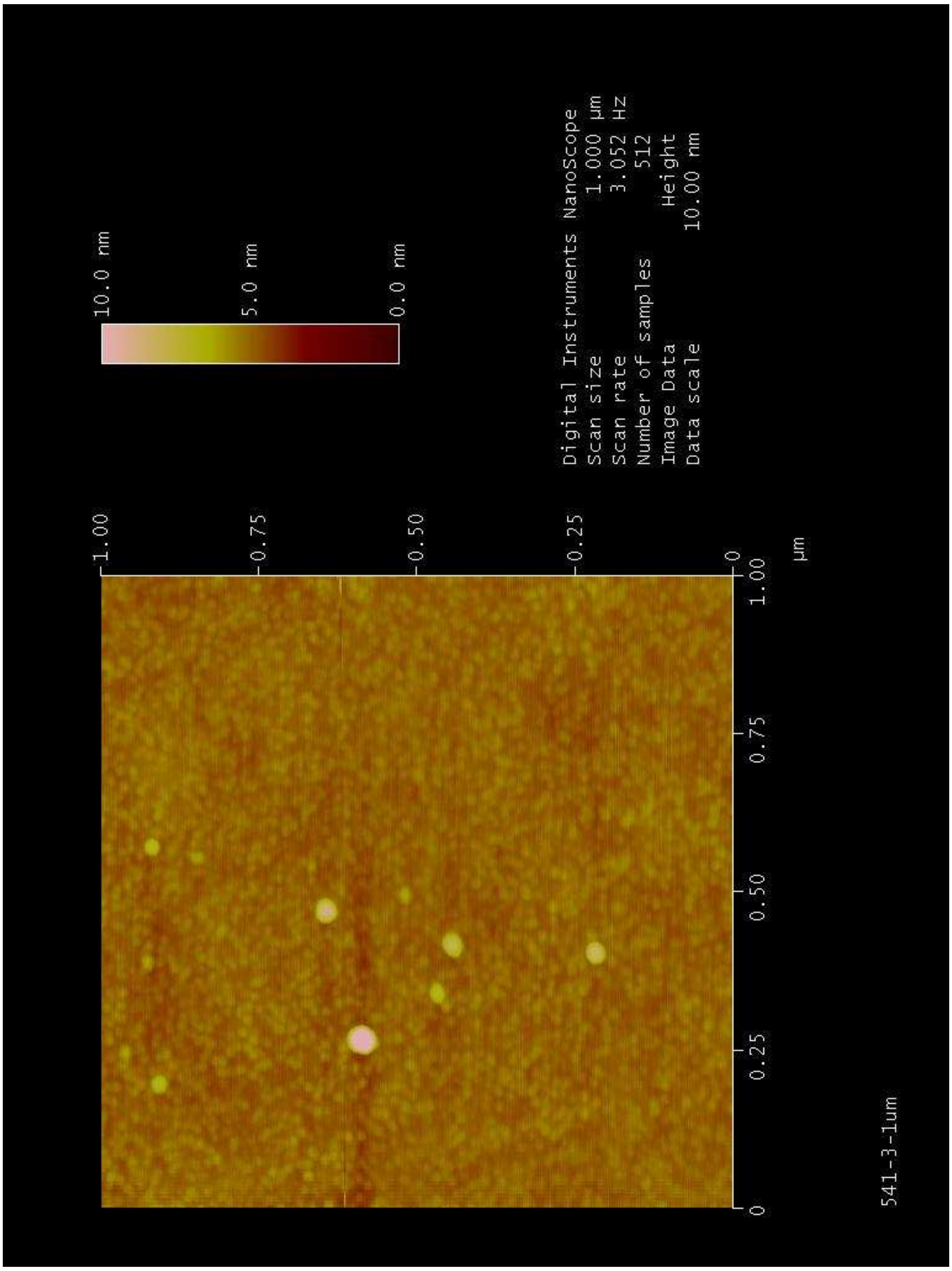
10.0 nm
5.0 nm
0.0 nm
Digital Instruments NanoScope
Scan size 1.000 µm
Scan rate 3.052 Hz
Number of samples 512
Image Data Height
Data scale 10.00 nm
1.00
0.75
0.50
0.25
0
µm
0
0.25
0.50
0.75
1.00
541-3-1um

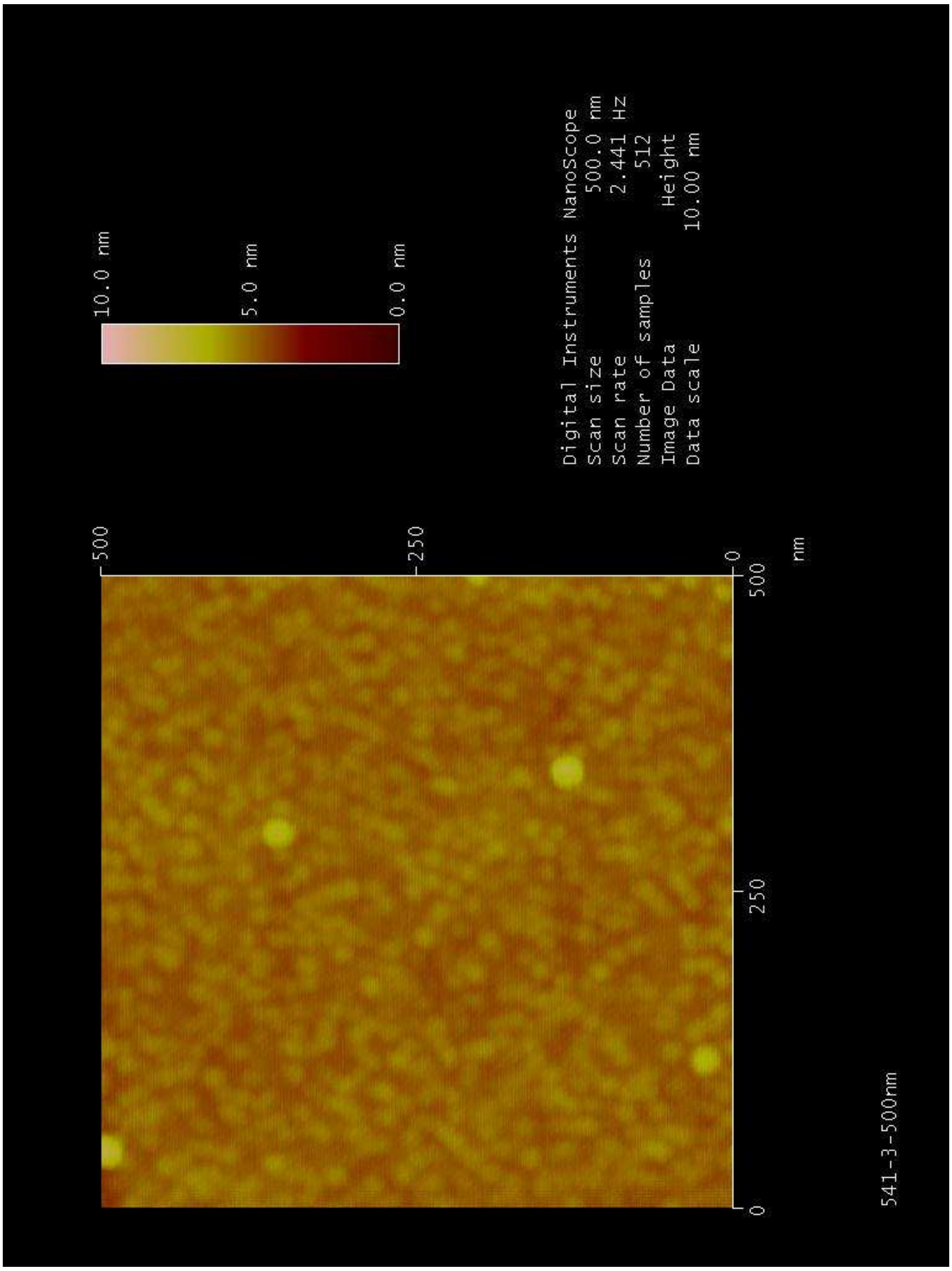
10.0 nm
5.0 nm
0.0 nm
Digital Instruments NanoScope
Scan size 500.0 nm
Scan rate 2.441 Hz
Number of samples 512
Image Data Height
Data scale 10.00 nm
500
250
0
500
250
0
nm
541-3-500nm

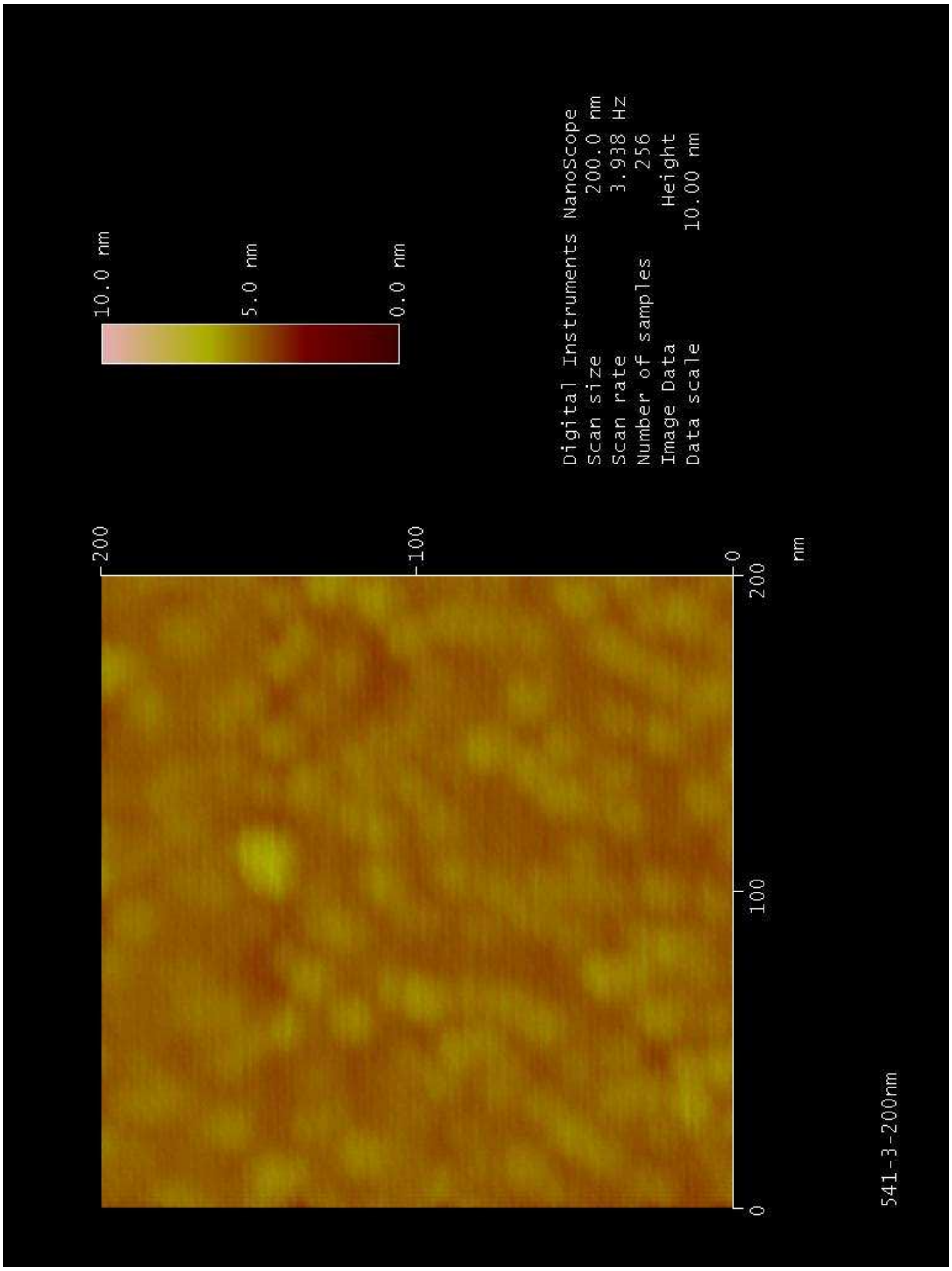
10.0 nm
5.0 nm
0.0 nm
Digital Instruments NanoScope
Scan size 200.0 nm
Scan rate 3.938 Hz
Number of samples 256
Image Data Height
Data scale 10.00 nm
200
100
0
nm
0
100
200
541-3-200nm

A.4 541-4

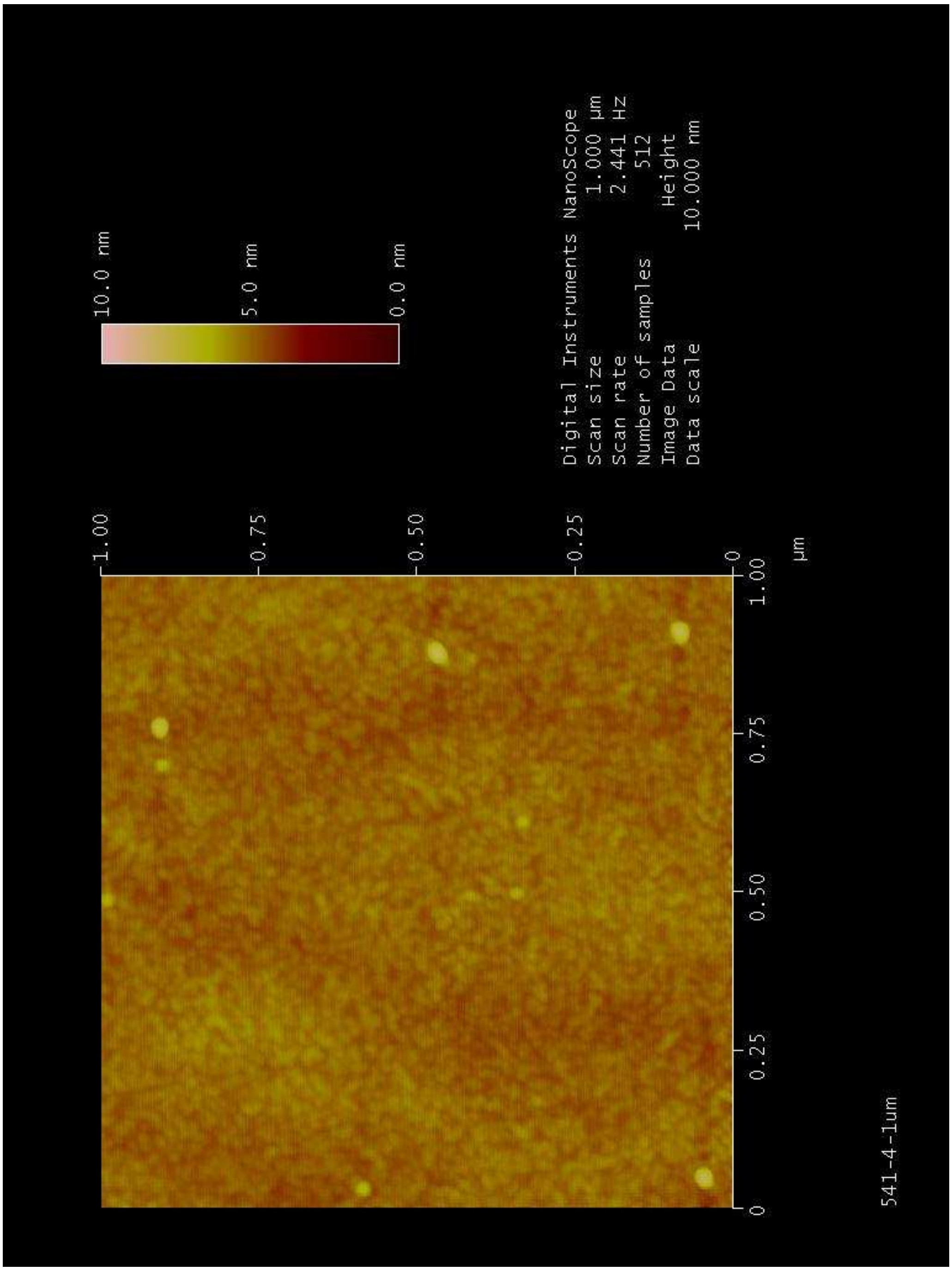
10.0 nm
5.0 nm
0.0 nm
Digital Instruments NanoScope
Scan size 1.000 µm
Scan rate 2.441 Hz
Number of samples 512
Image Data Height
Data scale 10.000 nm
1.00
0.75
0.50
0.25
0
µm
0
0.25
0.50
0.75
1.00
541-4-1um

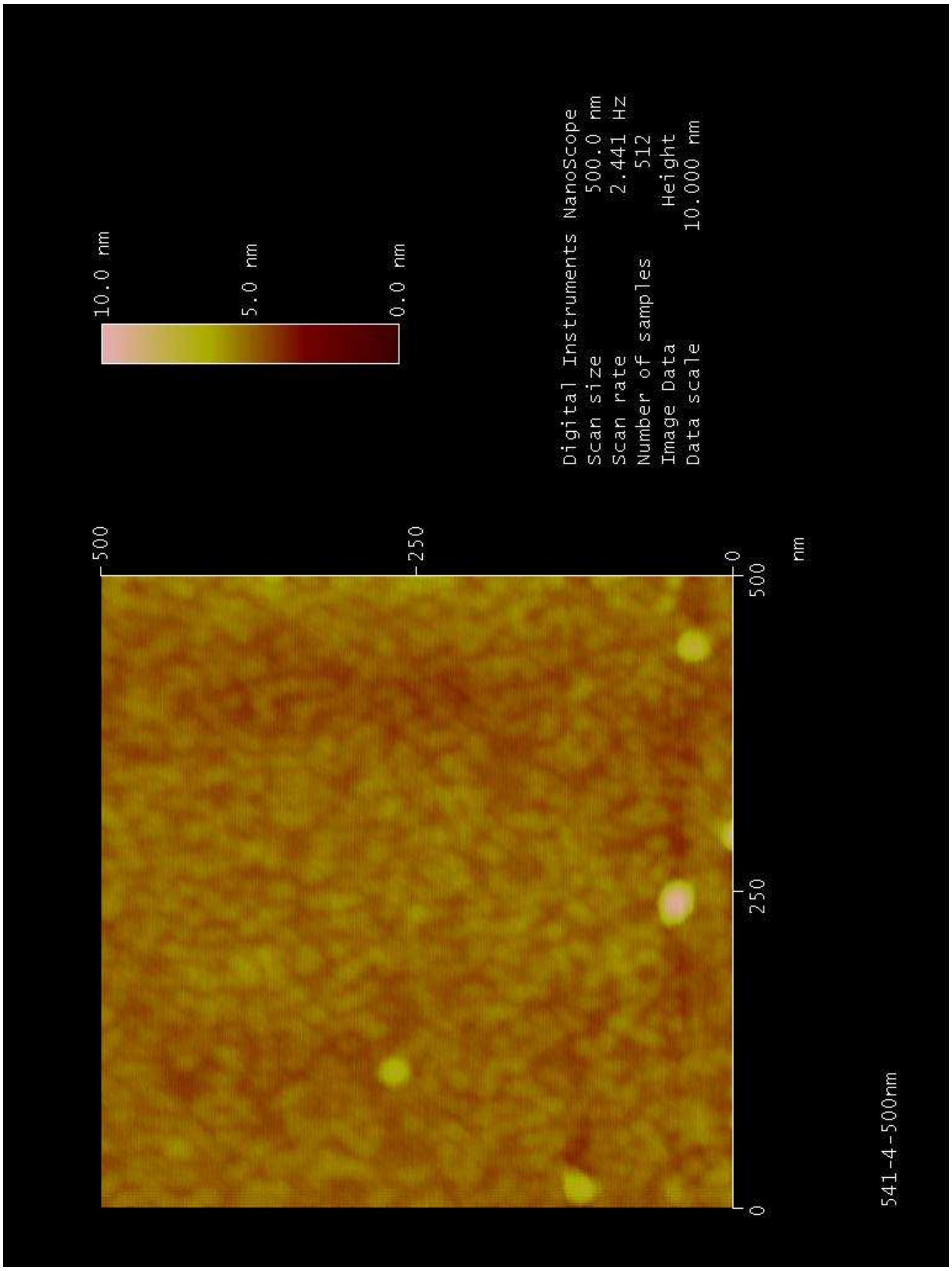
Digital Instruments NanoScope
Scan size 500.0 nm
Scan rate 2.441 Hz
Number of samples 512
Image Data Height
Data scale 10.000 nm
10.0 nm
5.0 nm
0.0 nm
500
250
0
nm
0
250
500
541-4-500nm

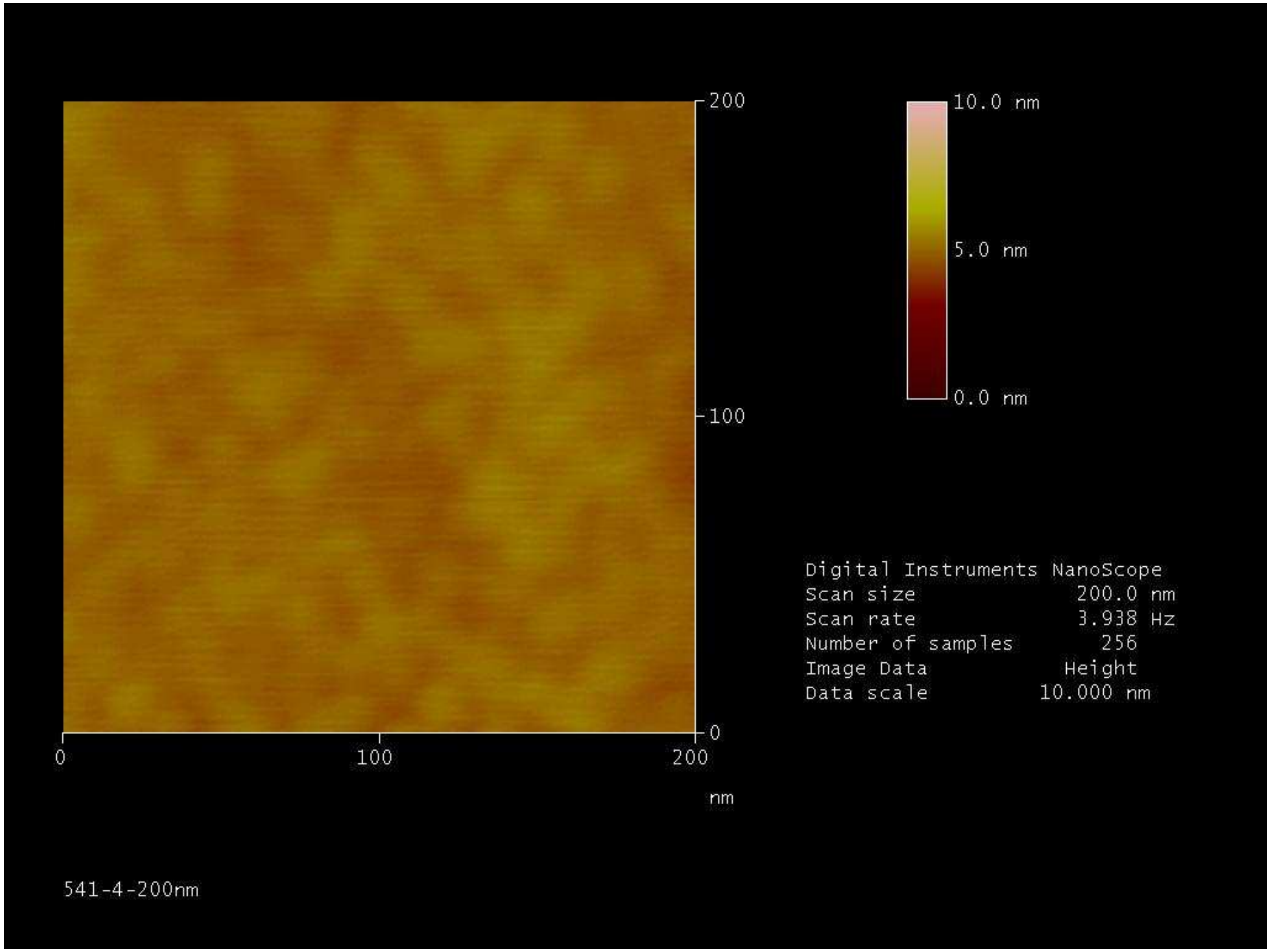
200
100
0
0
100
200
nm
10.0 nm
5.0 nm
0.0 nm
Digital Instruments NanoScope
Scan size 200.0 nm
Scan rate 3.938 Hz
Number of samples 256
Image Data Height
Data scale 10.000 nm
541-4-200nm

A.5 542-1

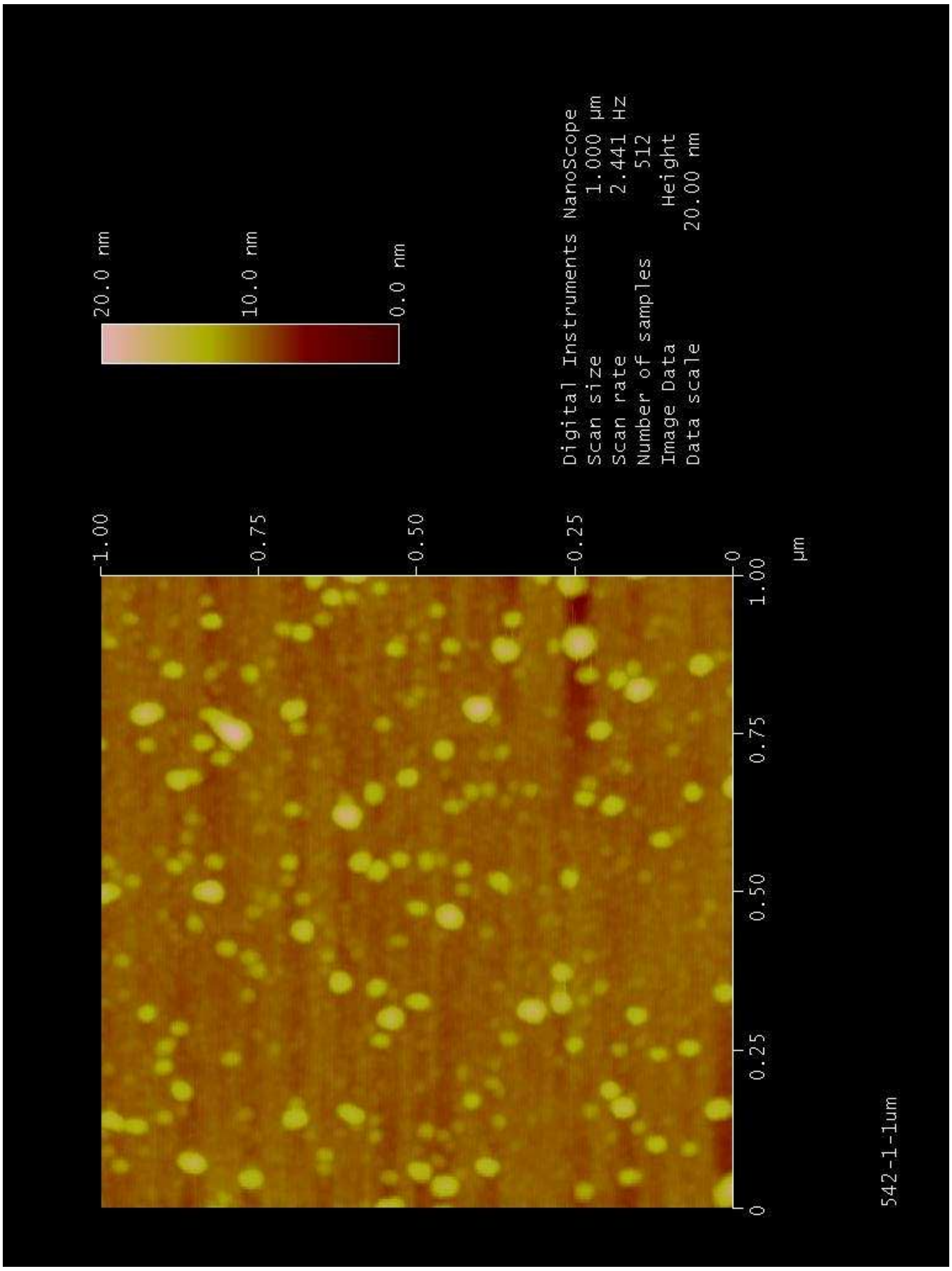

Digital Instruments NanoScope
Scan size 1.000 µm
Scan rate 2.441 Hz
Number of samples 512
Image Data Height
Data scale 20.00 nm

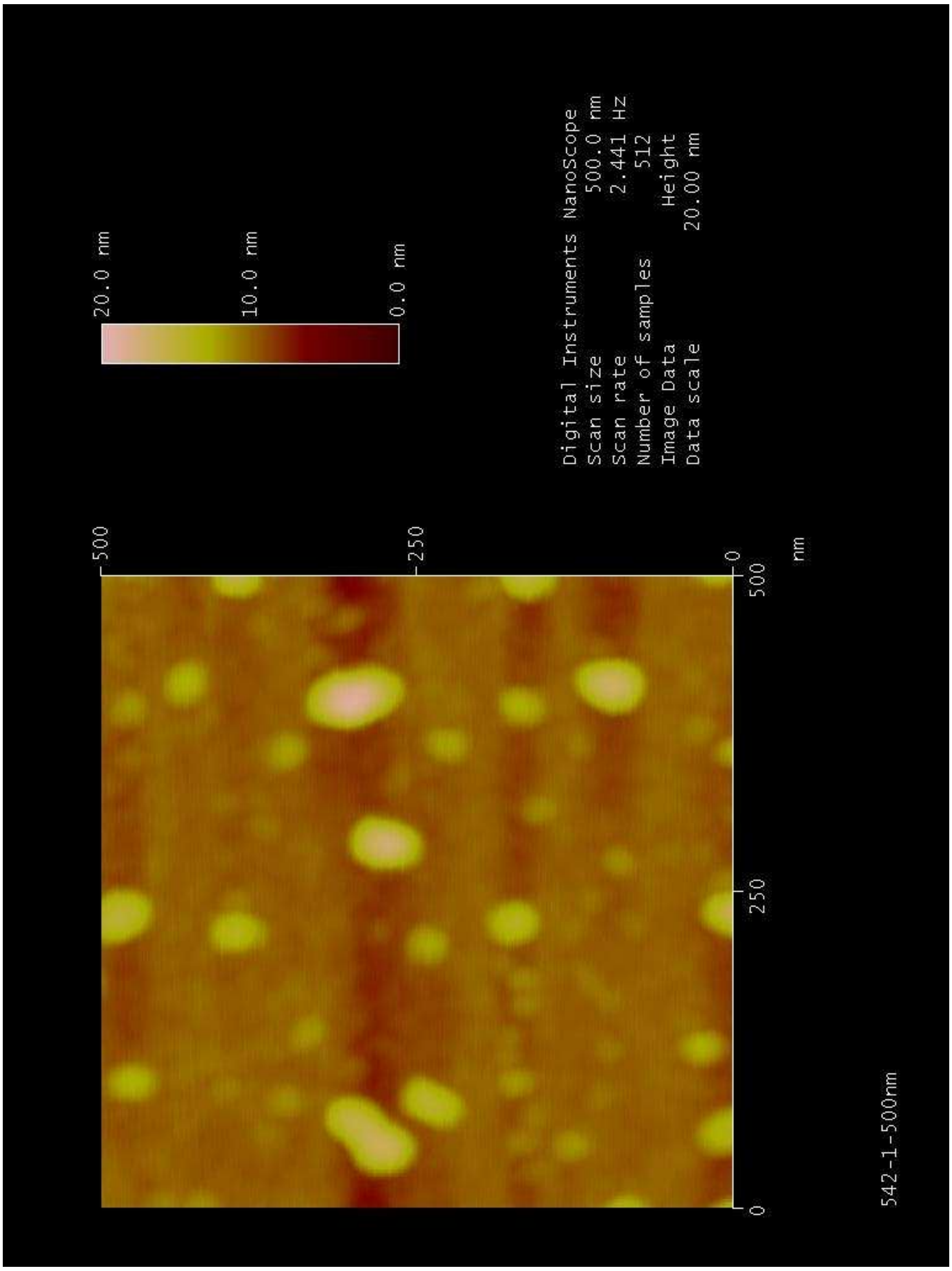
500
250
0
nm
0
250
500
20.0 nm
10.0 nm
0.0 nm
Digital Instruments NanoScope
Scan size 500.0 nm
Scan rate 2.441 Hz
Number of samples 512
Image Data Height
Data scale 20.00 nm
542-1-500nm

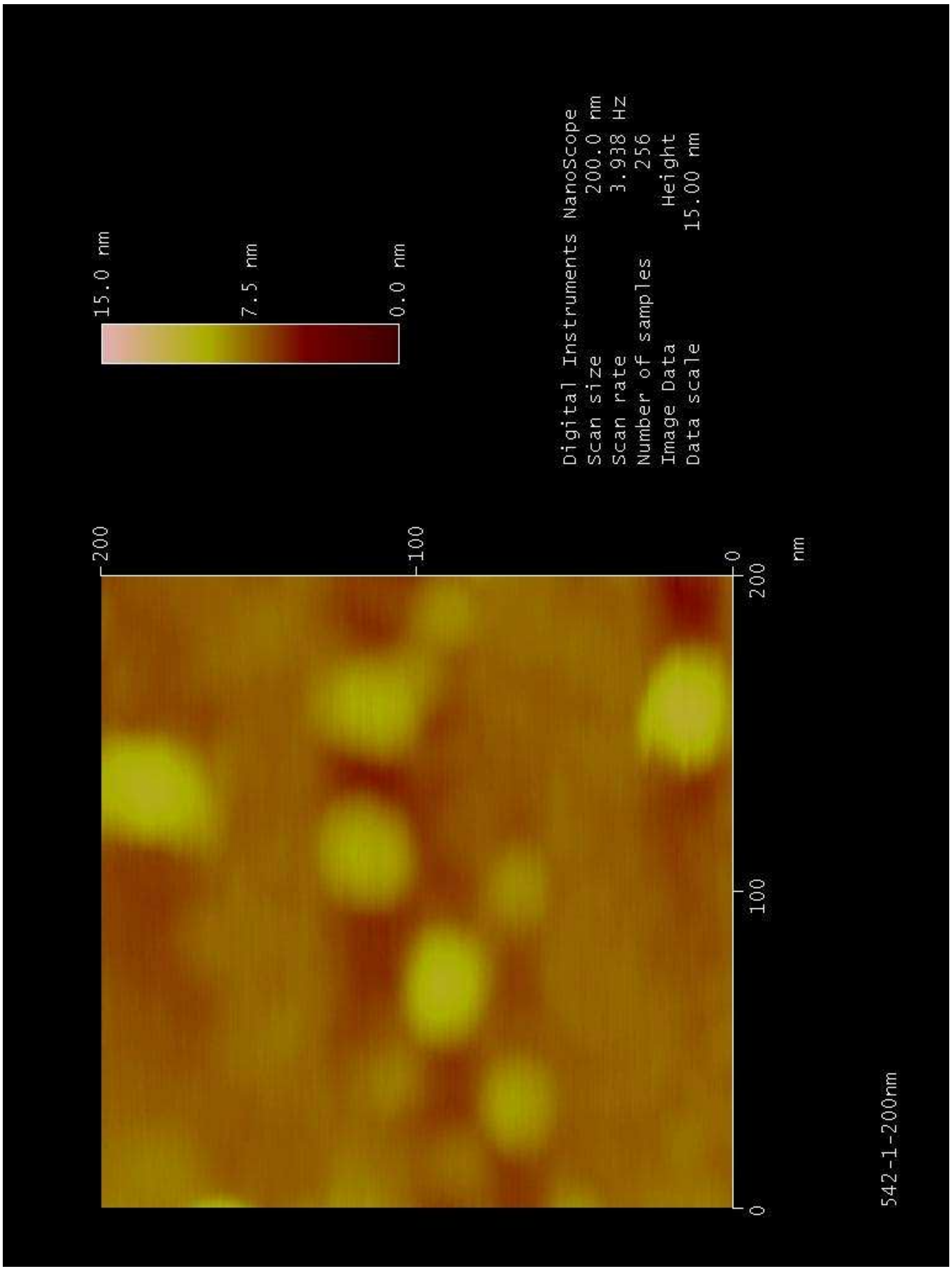
15.0 nm
7.5 nm
0.0 nm
Digital Instruments NanoScope
Scan size 200.0 nm
Scan rate 3.938 Hz
Number of samples 256
Image Data Height
Data scale 15.00 nm
200
100
0
200
100
0
nm
542-1-200nm

A.6 542-3

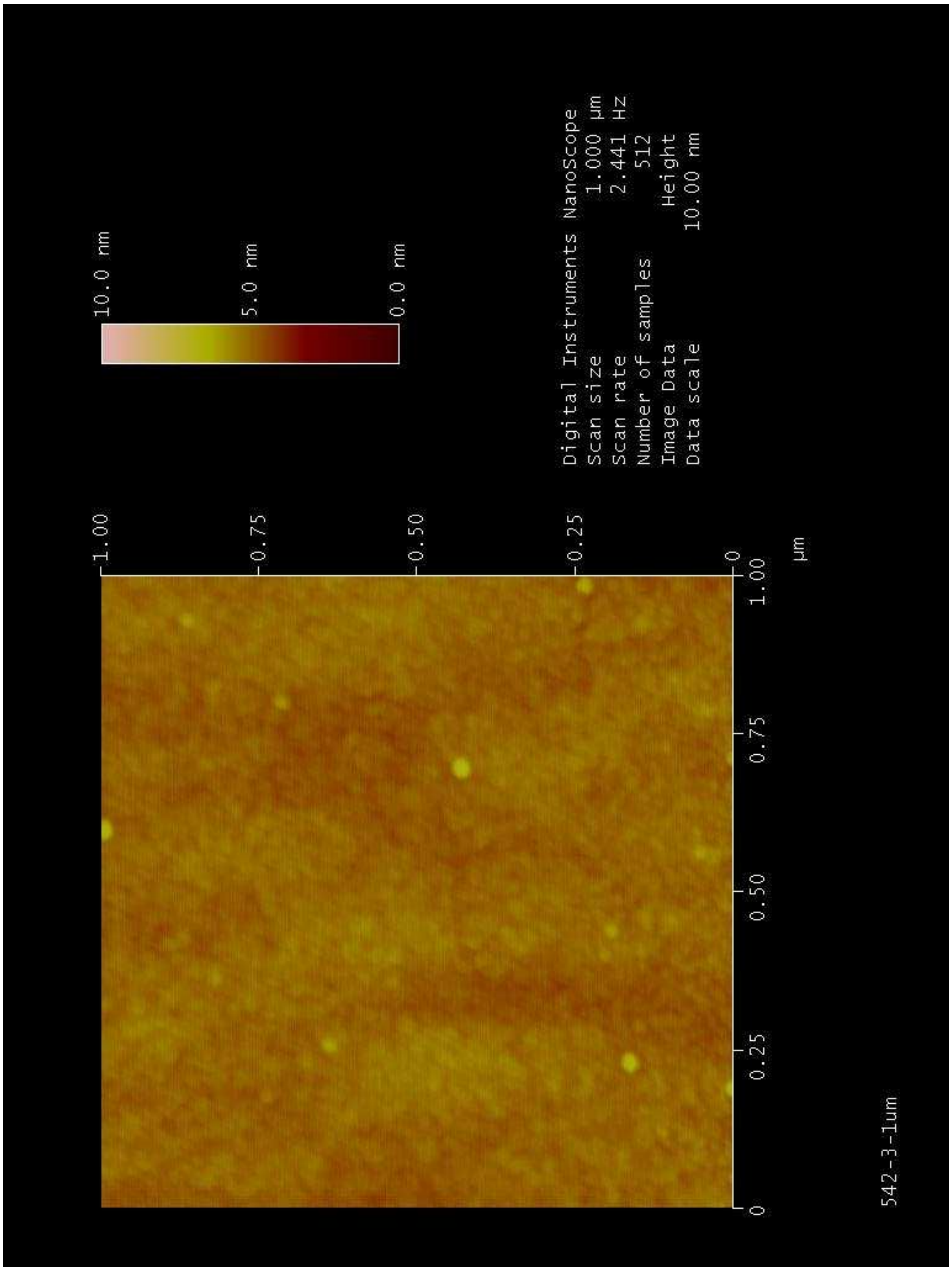

Digital Instruments NanoScope
Scan size 1.000 µm
Scan rate 2.441 Hz
Number of samples 512
Image Data Height
Data scale 10.00 nm

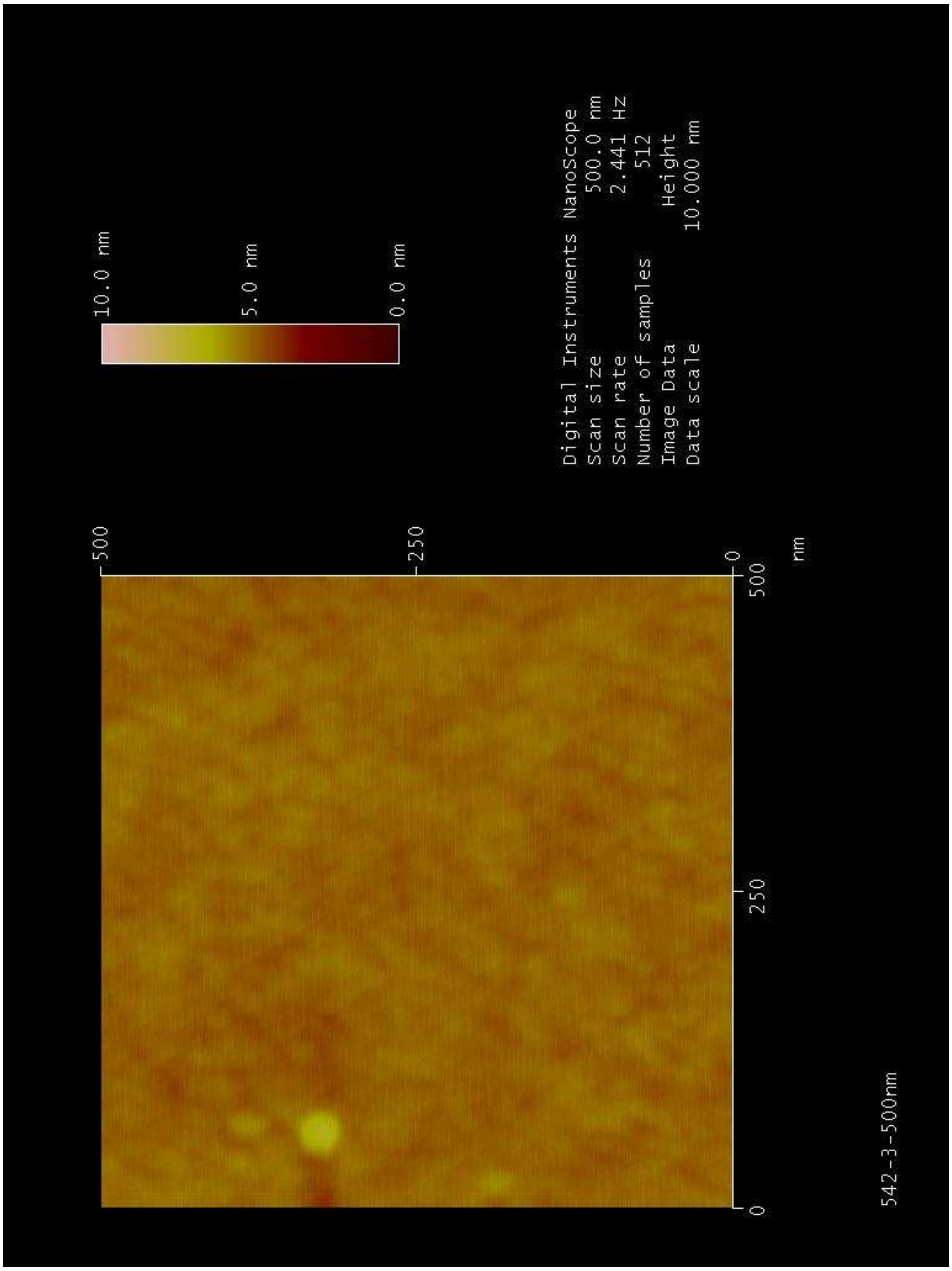
10.0 nm
5.0 nm
0.0 nm
Digital Instruments NanoScope
Scan size 500.0 nm
Scan rate 2.441 Hz
Number of samples 512
Image Data Height
Data scale 10.000 nm
500
250
0
nm
0
250
500
542-3-500nm

A.7 542-4

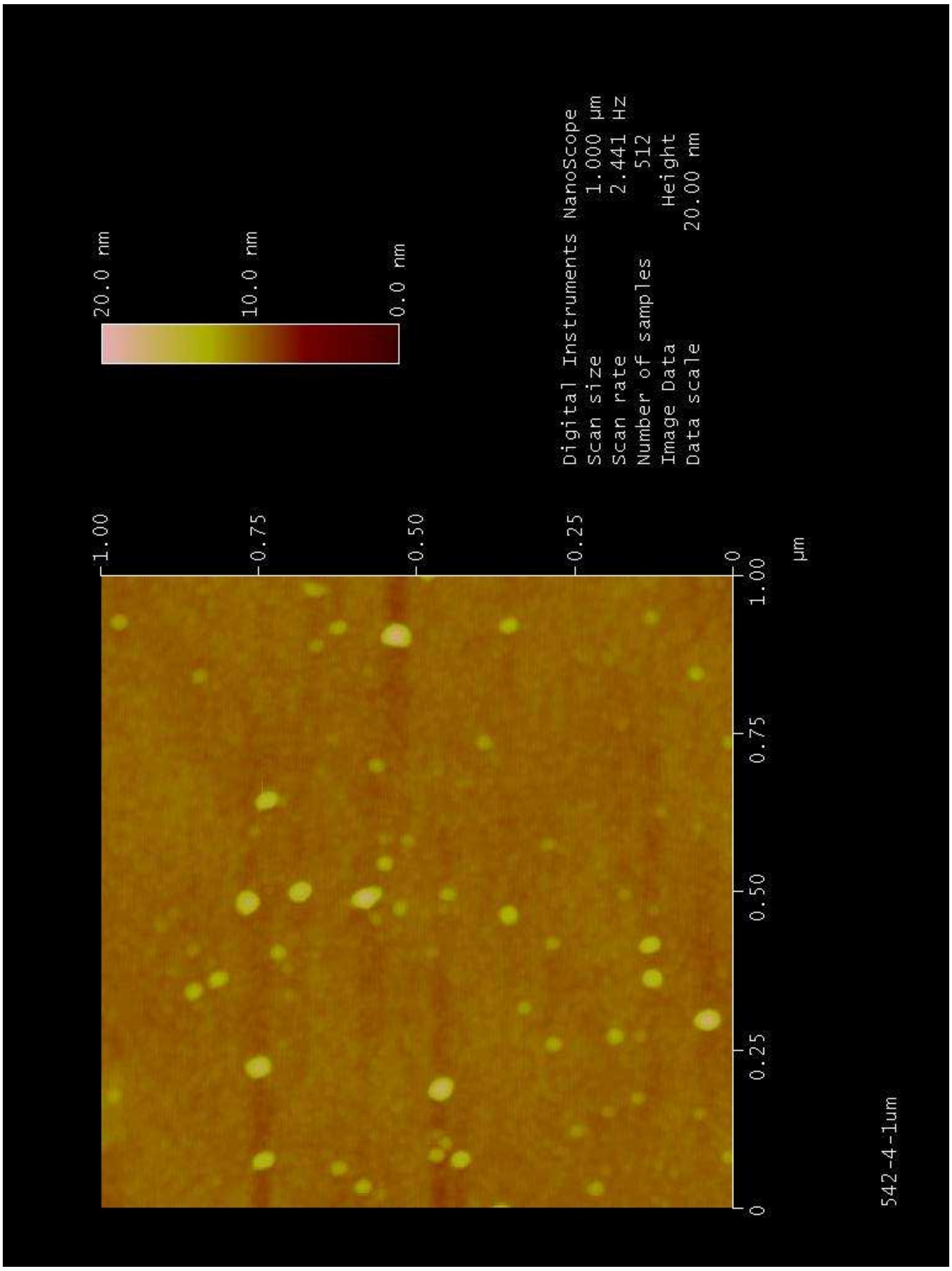
20.0 nm
10.0 nm
0.0 nm
Digital Instruments NanoScope
Scan size 1.000 µm
Scan rate 2.441 Hz
Number of samples 512
Image Data Height
Data scale 20.00 nm
1.00
0.75
0.50
0.25
0
µm
542-4-1um

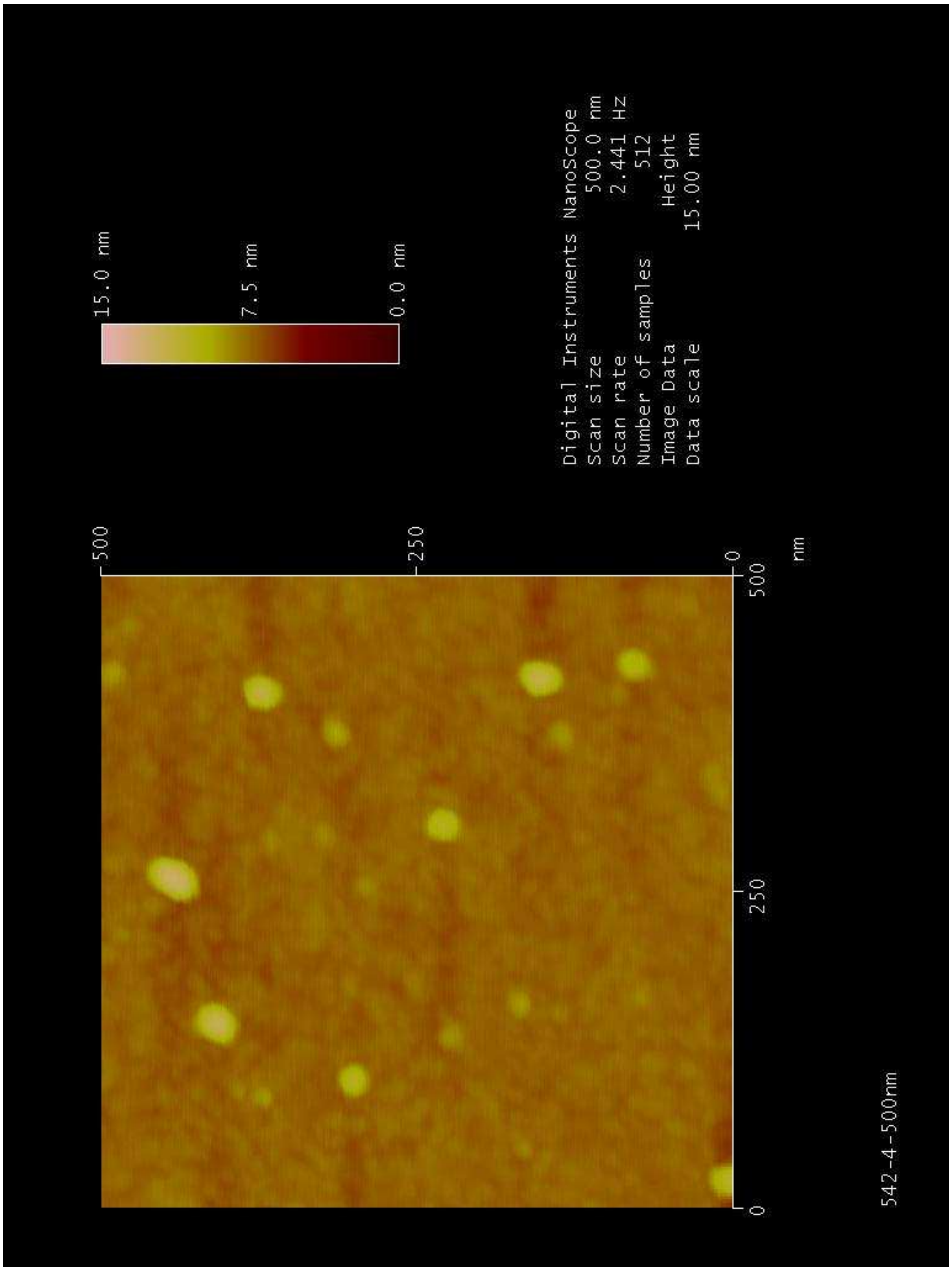

Digital Instruments NanoScope
Scan size 500.0 nm
Scan rate 2.441 Hz
Number of samples 512
Image Data Height
Data scale 15.00 nm

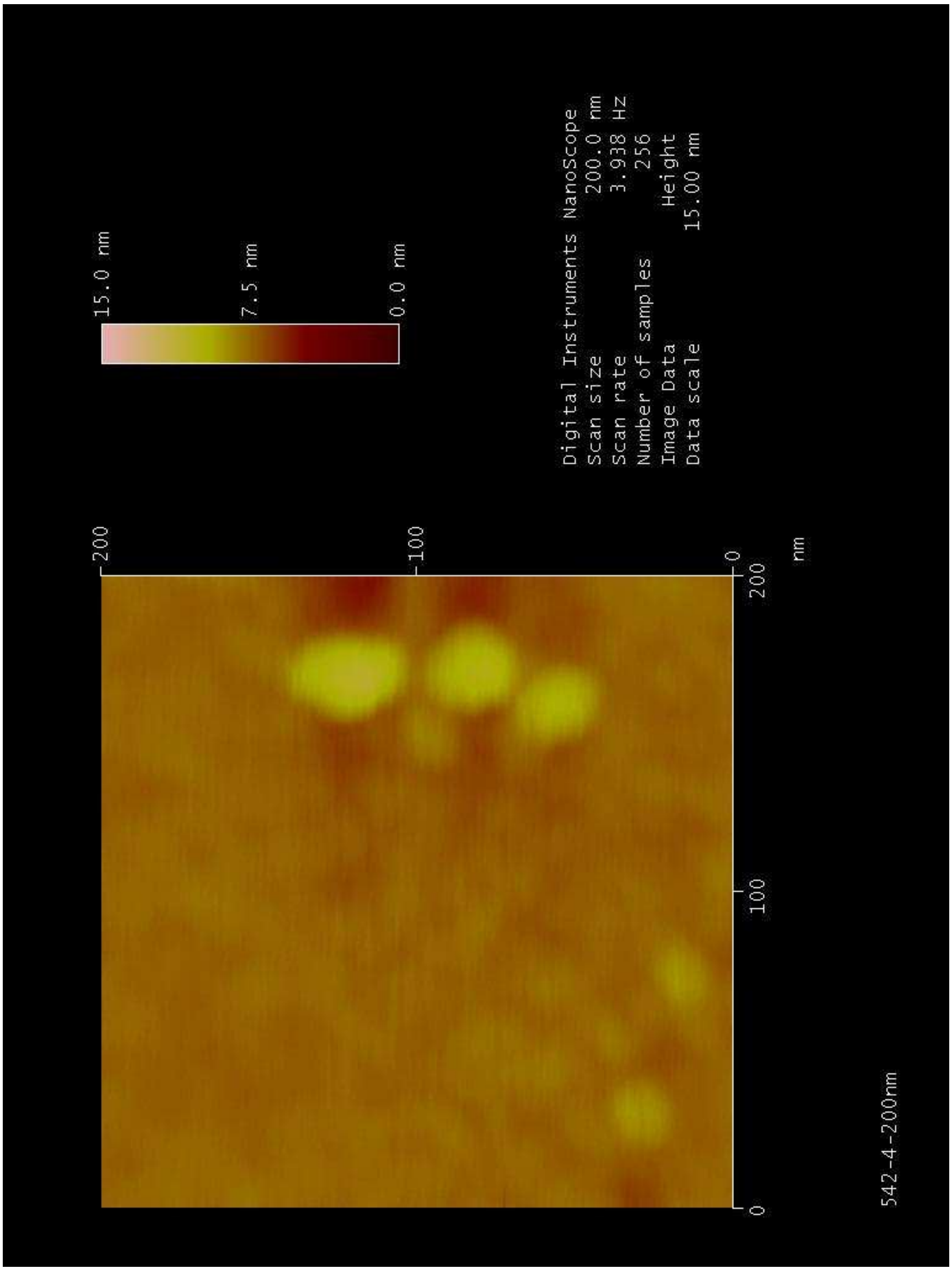
15.0 nm
7.5 nm
0.0 nm
Digital Instruments NanoScope
Scan size 200.0 nm
Scan rate 3.938 Hz
Number of samples 256
Image Data Height
Data scale 15.00 nm
200
100
0
nm
0
100
200
542-4-200nm

A.8 543-1

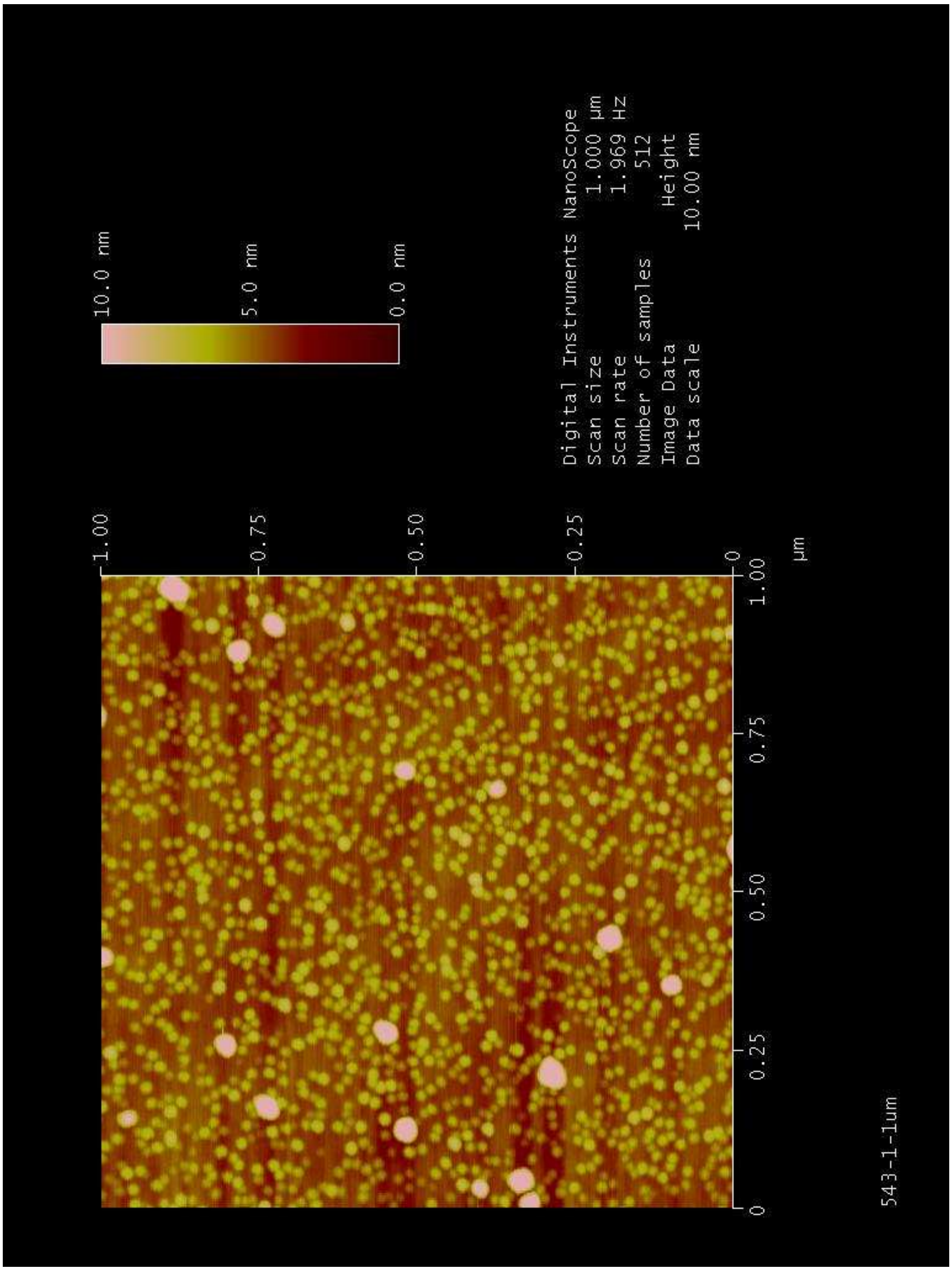
10.0 nm
5.0 nm
0.0 nm
Digital Instruments NanoScope
Scan size 1.000 µm
Scan rate 1.969 Hz
Number of samples 512
Image Data Height
Data scale 10.00 nm
1.00
0.75
0.50
0.25
0
µm
543-1-1um

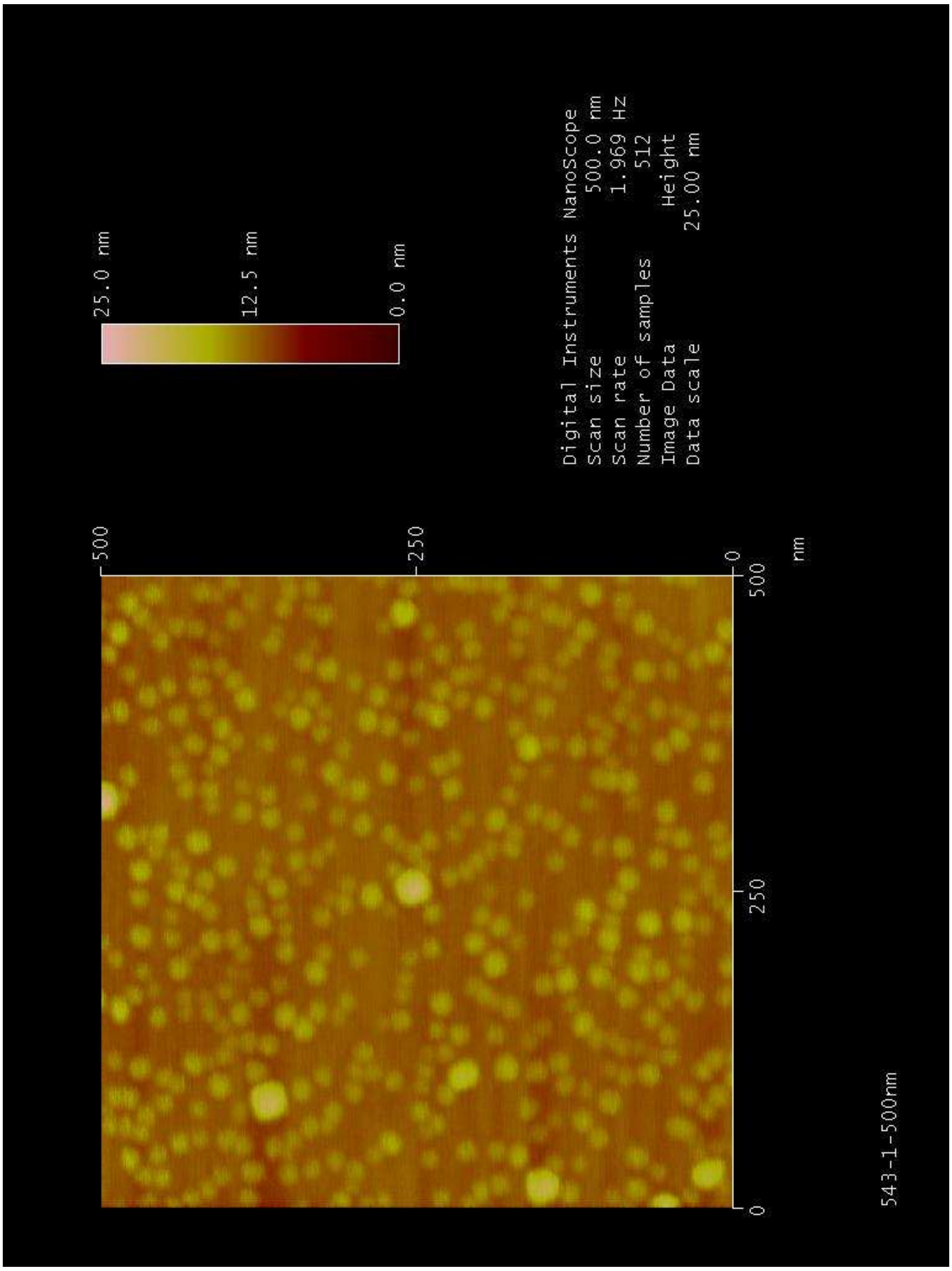
25.0 nm
12.5 nm
0.0 nm
Digital Instruments NanoScope
Scan size 500.0 nm
Scan rate 1.969 Hz
Number of samples 512
Image Data Height
Data scale 25.00 nm
500
250
0
nm
0
250
500
543-1-500nm

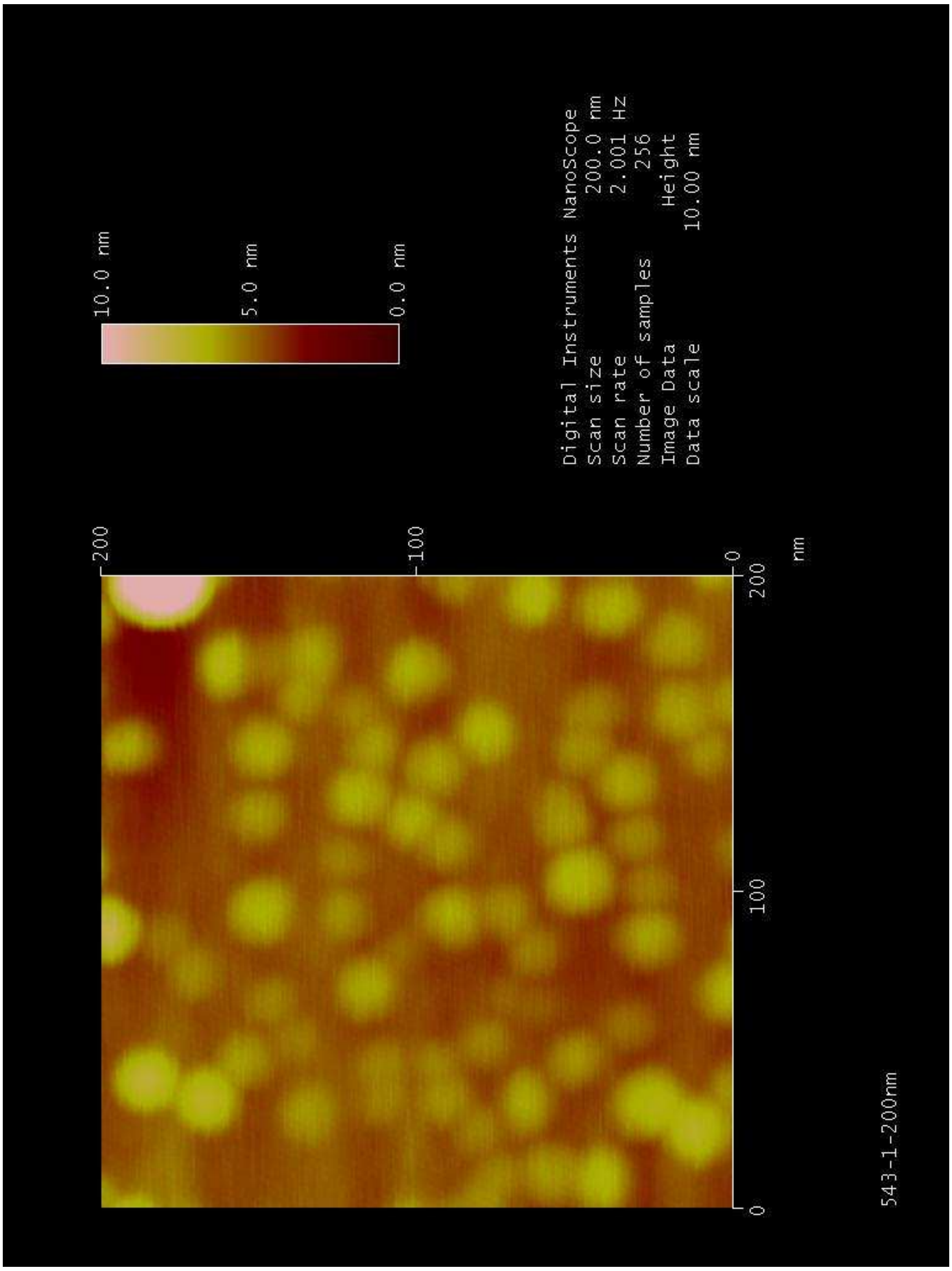
10.0 nm
5.0 nm
0.0 nm
Digital Instruments NanoScope
Scan size 200.0 nm
Scan rate 2.001 Hz
Number of samples 256
Image Data Height
Data scale 10.00 nm
200
100
0
nm
0
100
200
543-1-200nm

A.9 543-2

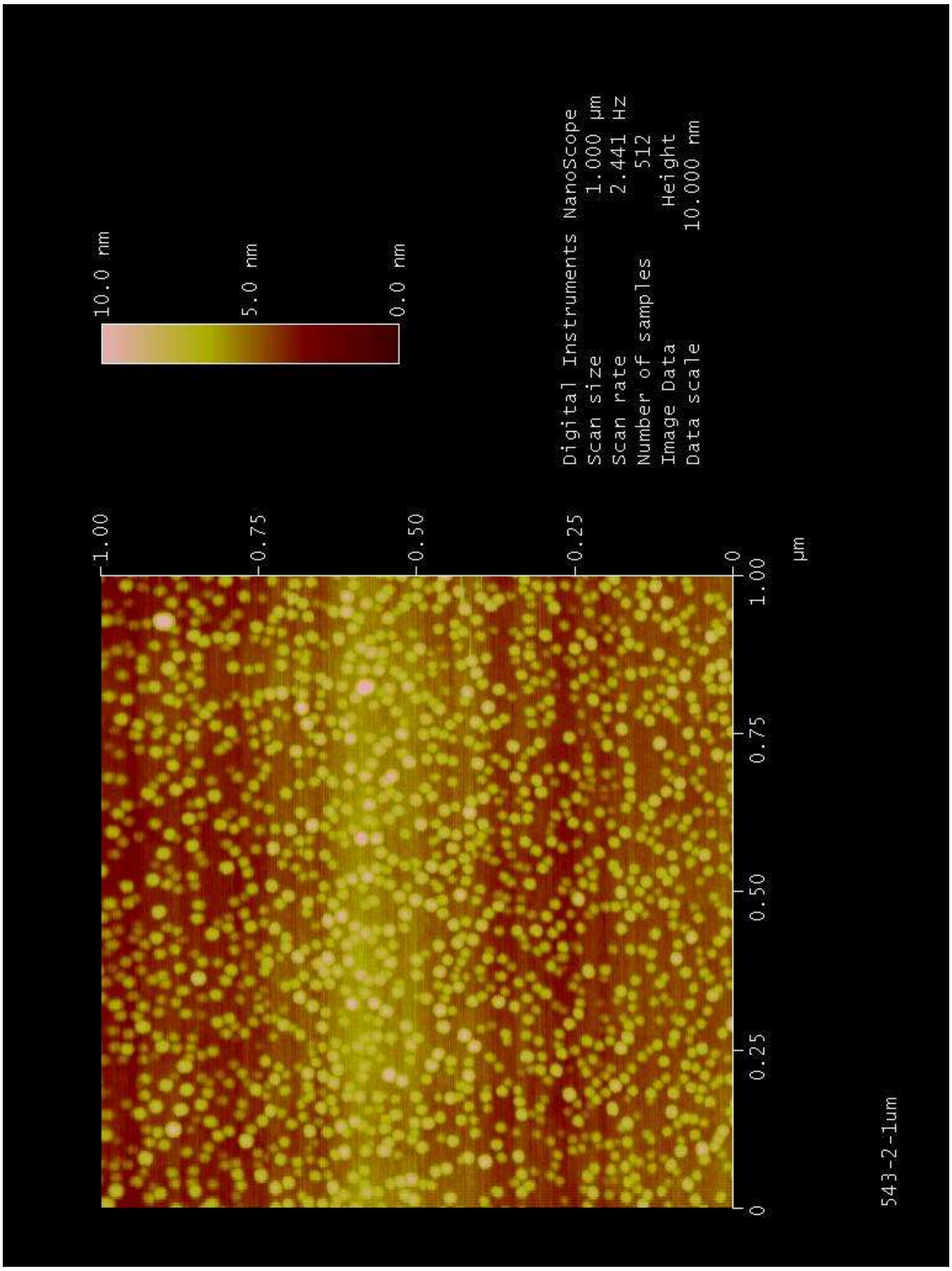
10.0 nm
5.0 nm
0.0 nm
Digital Instruments NanoScope
Scan size 1.000 µm
Scan rate 2.441 Hz
Number of samples 512
Image Data Height
Data scale 10.000 nm
1.00
0.75
0.50
0.25
0
µm
543-2-1um

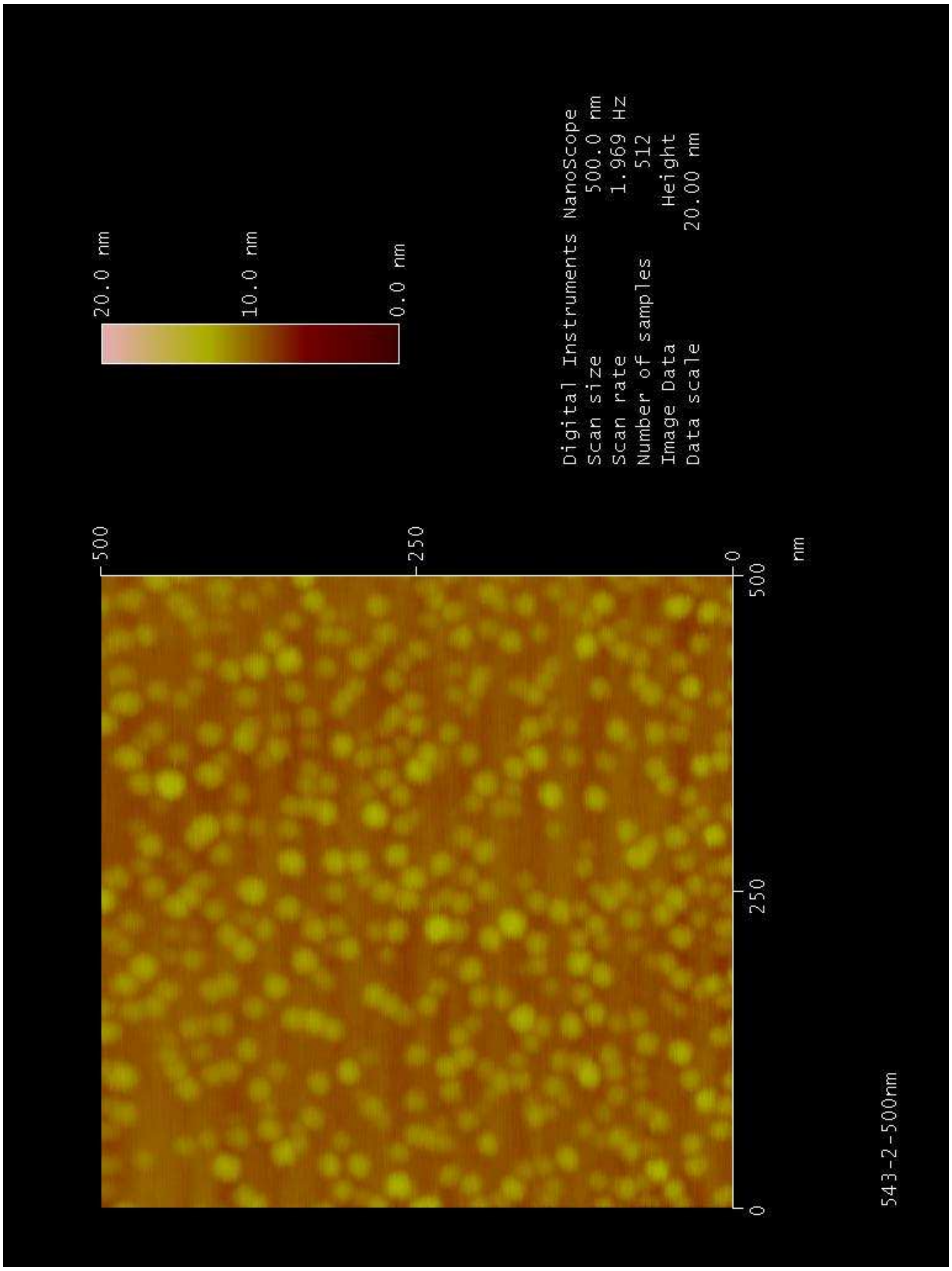
20.0 nm
10.0 nm
0.0 nm
Digital Instruments NanoScope
Scan size 500.0 nm
Scan rate 1.969 Hz
Number of samples 512
Image Data Height
Data scale 20.00 nm
500
250
0
nm
543-2-500nm

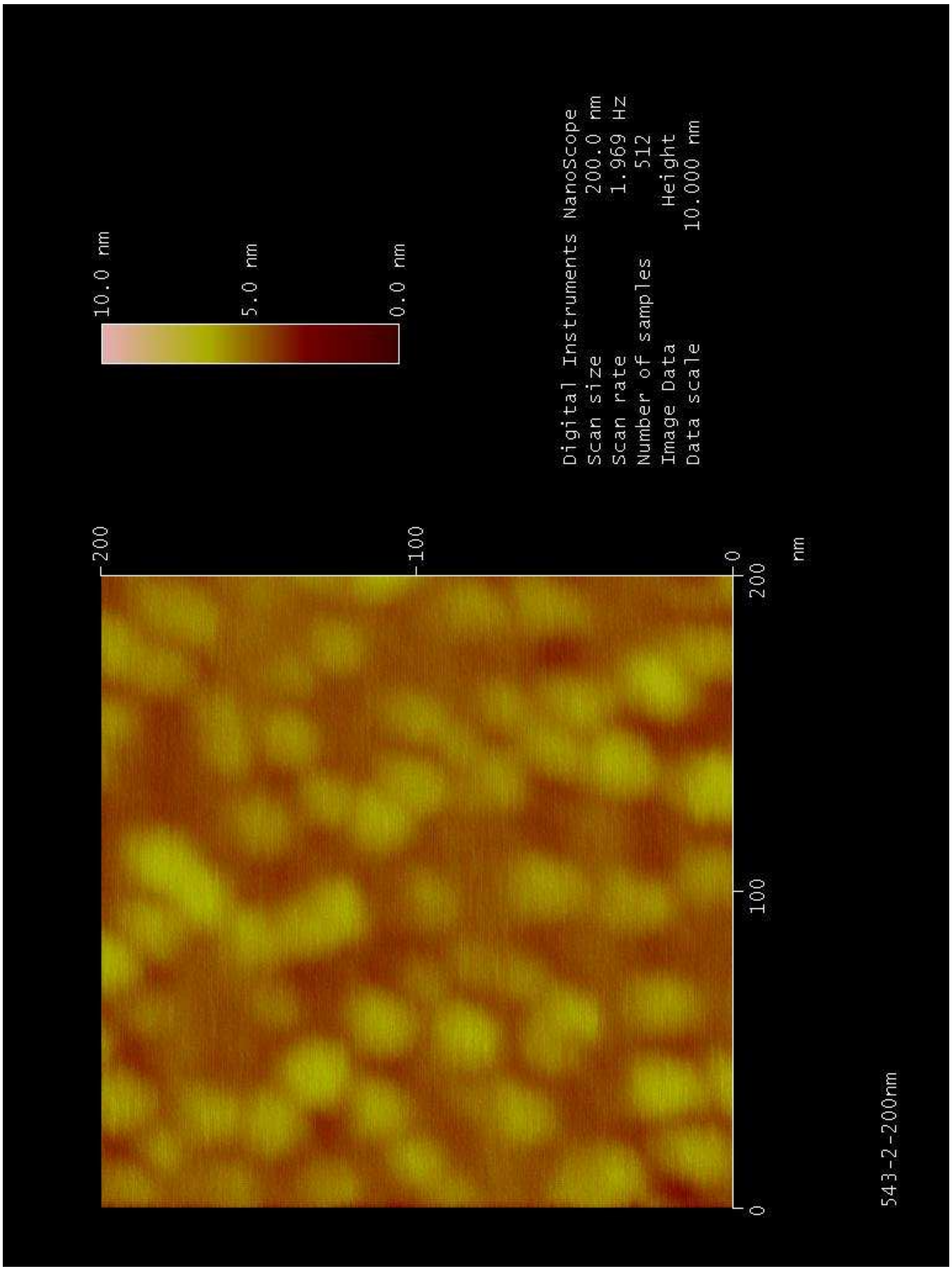
10.0 nm
5.0 nm
0.0 nm
Digital Instruments NanoScope
Scan size 200.0 nm
Scan rate 1.969 Hz
Number of samples 512
Image Data Height
Data scale 10.000 nm
200
100
0
200
100
0
nm
543-2-200nm

A.10 543-3

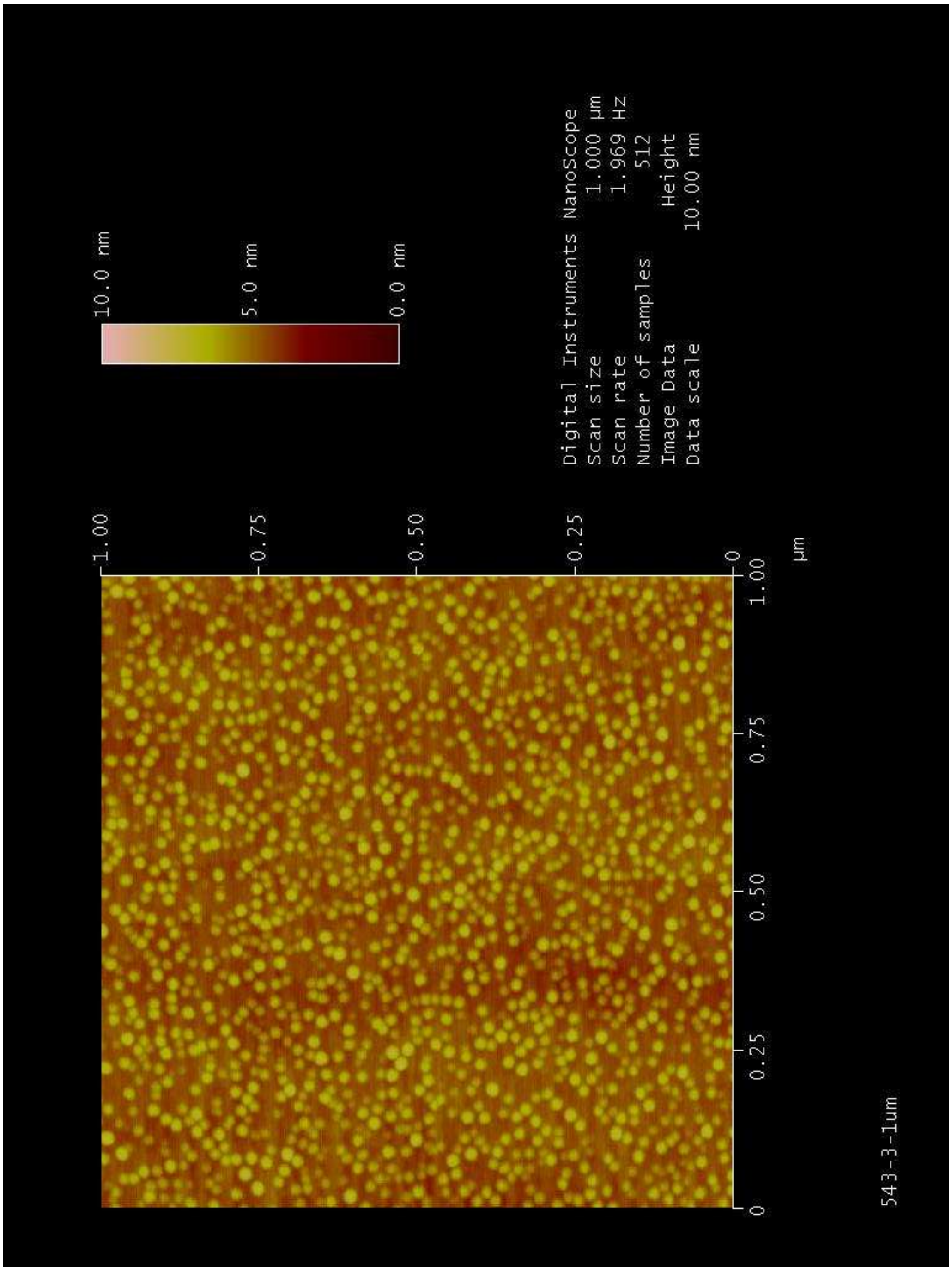
10.0 nm
5.0 nm
0.0 nm
1.00
0.75
0.50
0.25
0
µm
Digital Instruments NanoScope
Scan size 1.000 µm
Scan rate 1.969 Hz
Number of samples 512
Image Data Height
Data scale 10.00 nm
543-3-1um

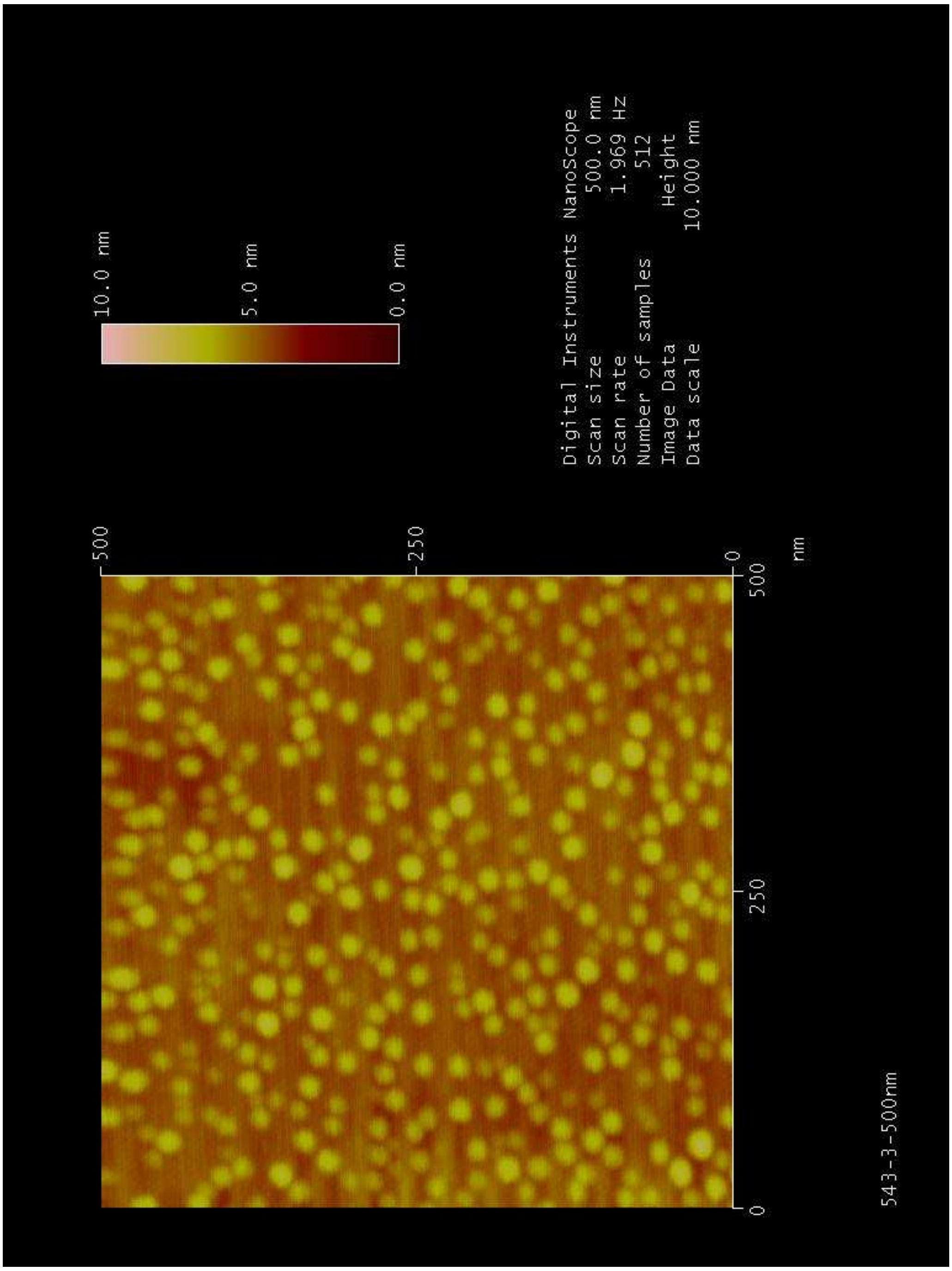
500
250
0
nm
0
250
500
10.0 nm
5.0 nm
0.0 nm
Digital Instruments NanoScope
Scan size 500.0 nm
Scan rate 1.969 Hz
Number of samples 512
Image Data Height
Data scale 10.000 nm
543-3-500nm

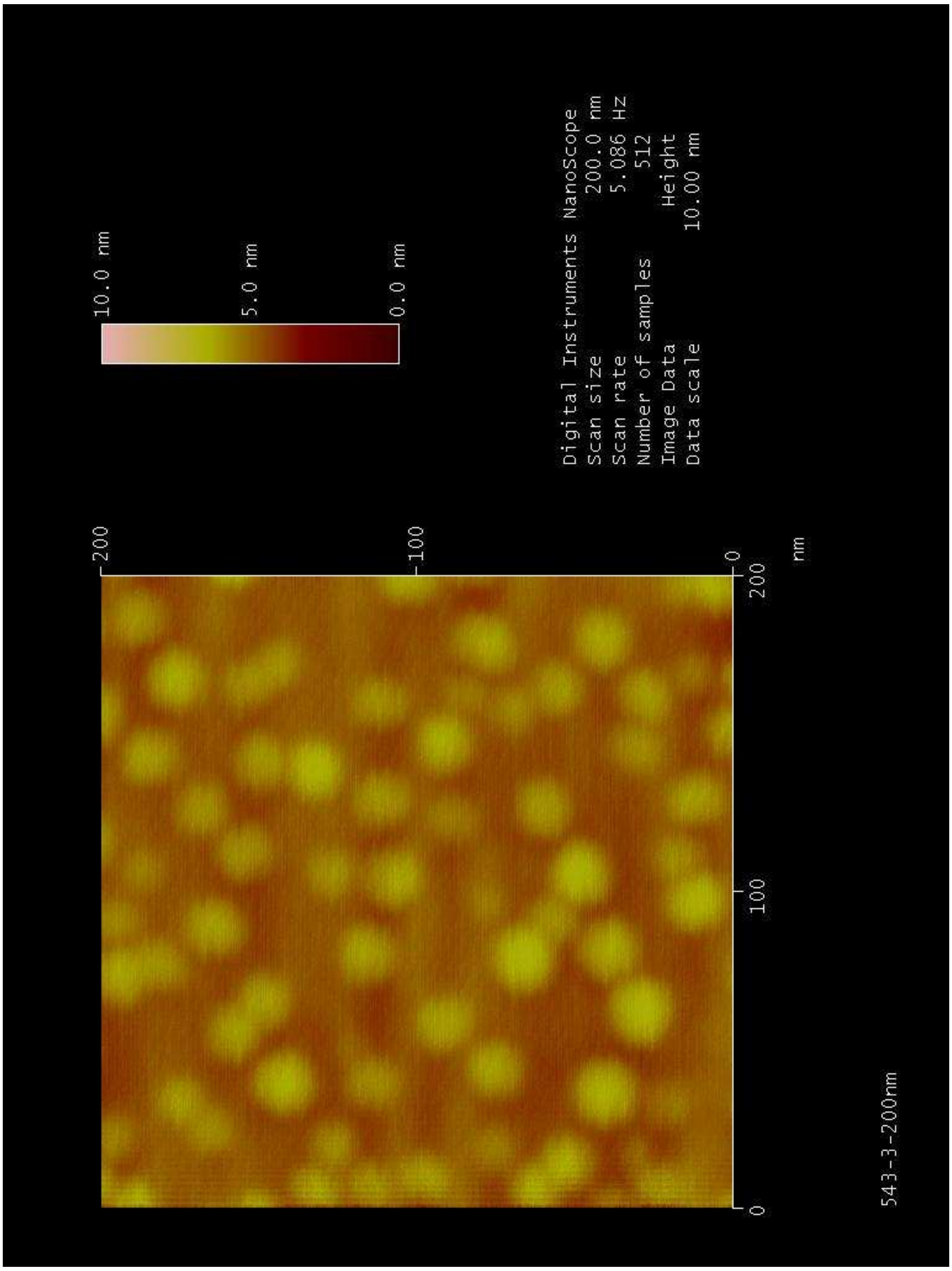
10.0 nm
5.0 nm
0.0 nm
Digital Instruments NanoScope
Scan size 200.0 nm
Scan rate 5.086 Hz
Number of samples 512
Image Data Height
Data scale 10.00 nm
200
100
0
nm
200
100
0
543-3-200nm

A.11 544-1

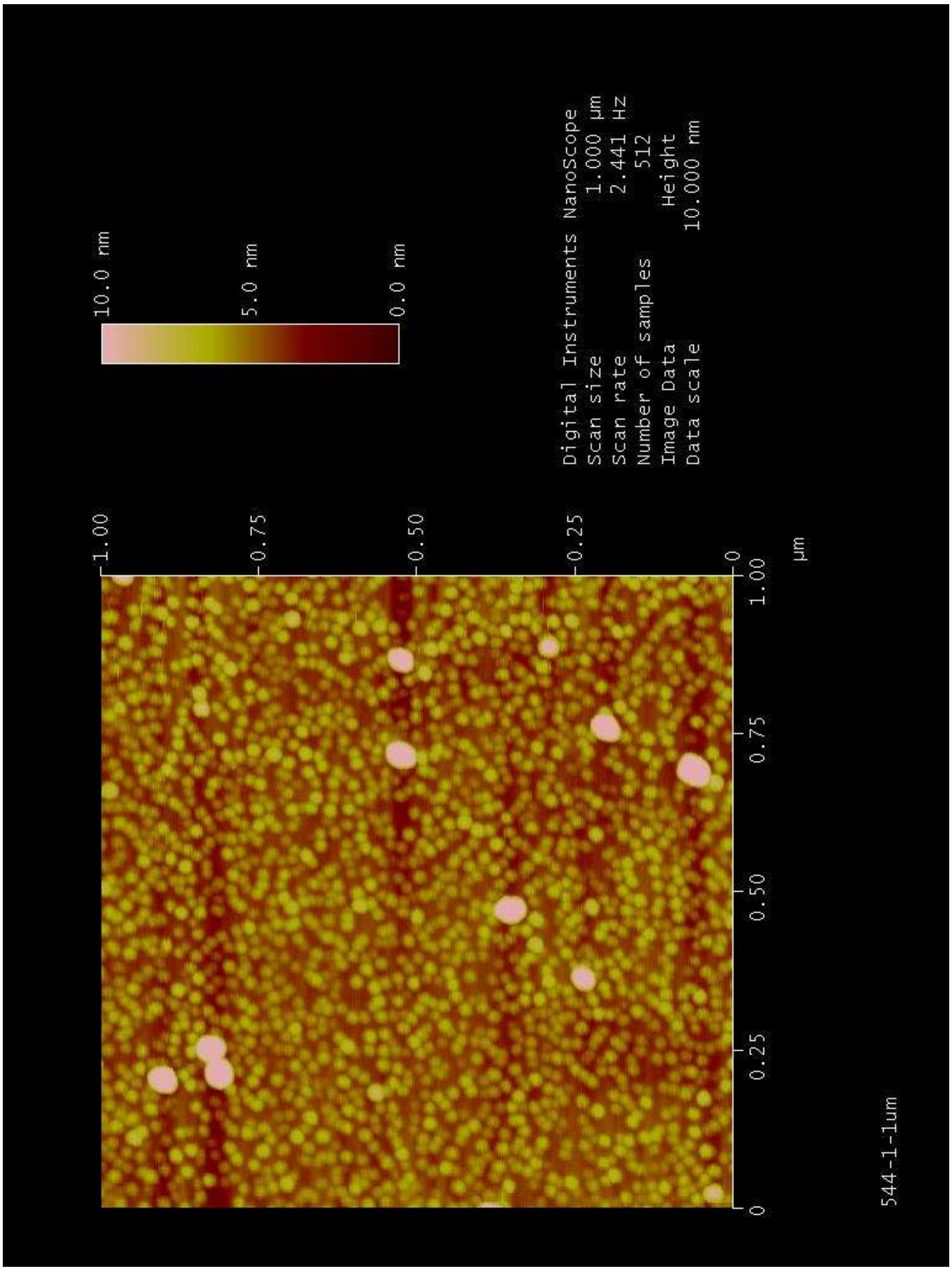
10.0 nm
5.0 nm
0.0 nm
Digital Instruments NanoScope
Scan size 1.000 µm
Scan rate 2.441 Hz
Number of samples 512
Image Data Height
Data scale 10.000 nm
1.00
0.75
0.50
0.25
0
µm
0
0.25
0.50
0.75
1.00
544-1-1um

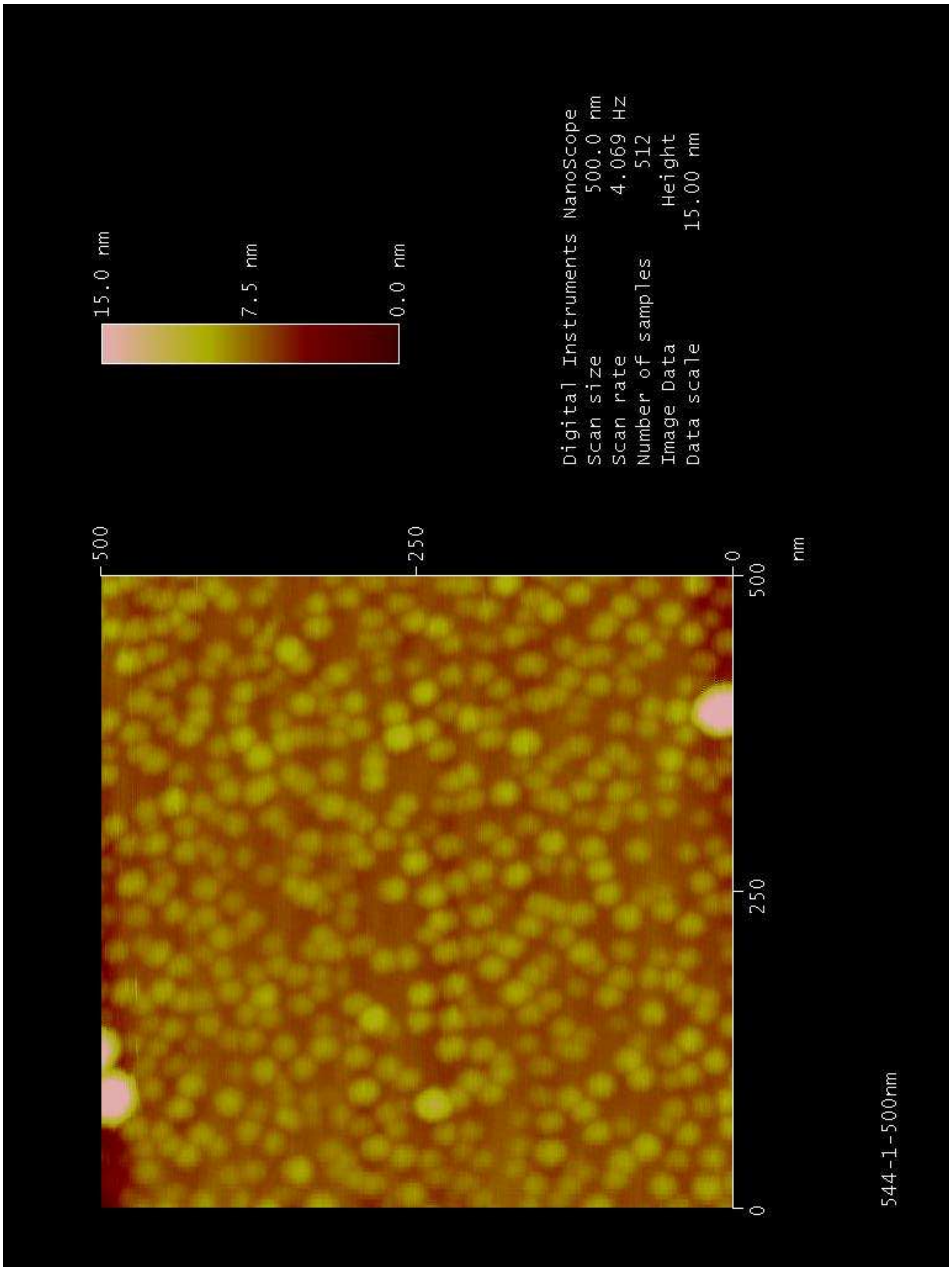
15.0 nm
7.5 nm
0.0 nm
Digital Instruments NanoScope
Scan size 500.0 nm
Scan rate 4.069 Hz
Number of samples 512
Image Data Height
Data scale 15.00 nm
500
250
0
nm
544-1-500nm

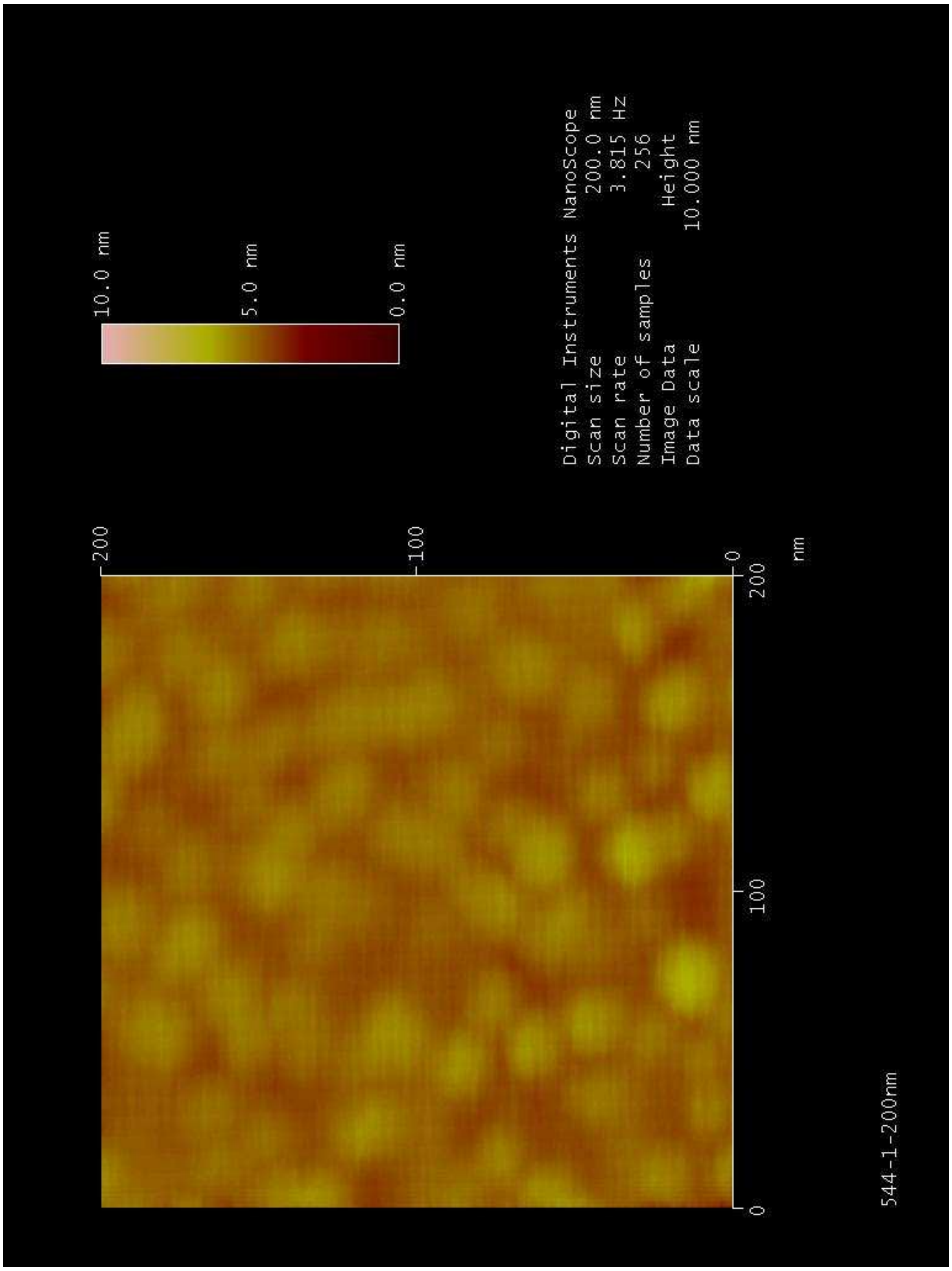
10.0 nm
5.0 nm
0.0 nm
Digital Instruments NanoScope
Scan size 200.0 nm
Scan rate 3.815 Hz
Number of samples 256
Image Data Height
Data scale 10.000 nm
200
100
0
nm
200
100
0
544-1-200nm

A.12 544-2

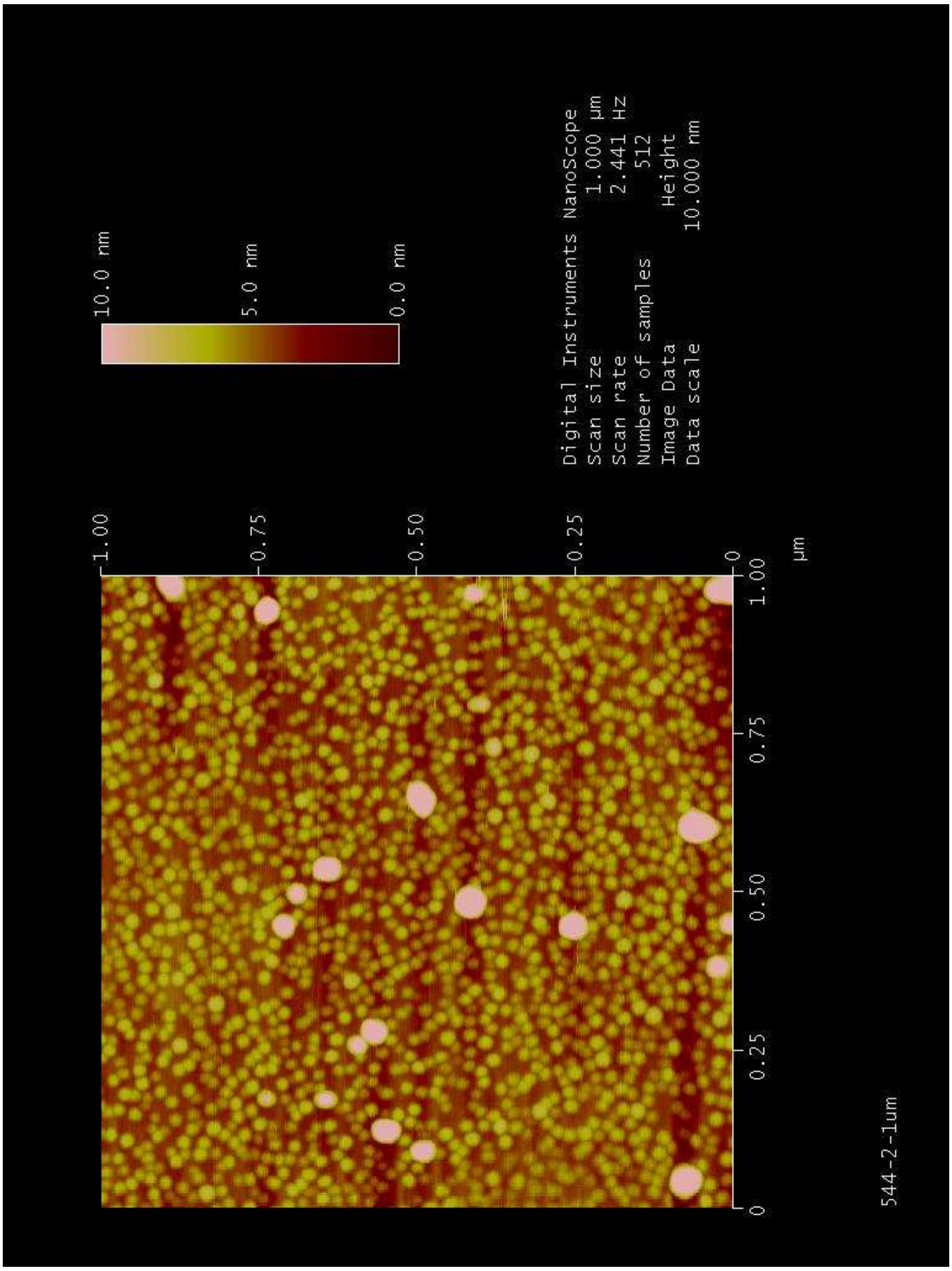
10.0 nm
5.0 nm
0.0 nm
Digital Instruments NanoScope
Scan size 1.000 µm
Scan rate 2.441 Hz
Number of samples 512
Image Data Height
Data scale 10.000 nm
1.00
0.75
0.50
0.25
0
µm
0
0.25
0.50
0.75
1.00
544-2-1um

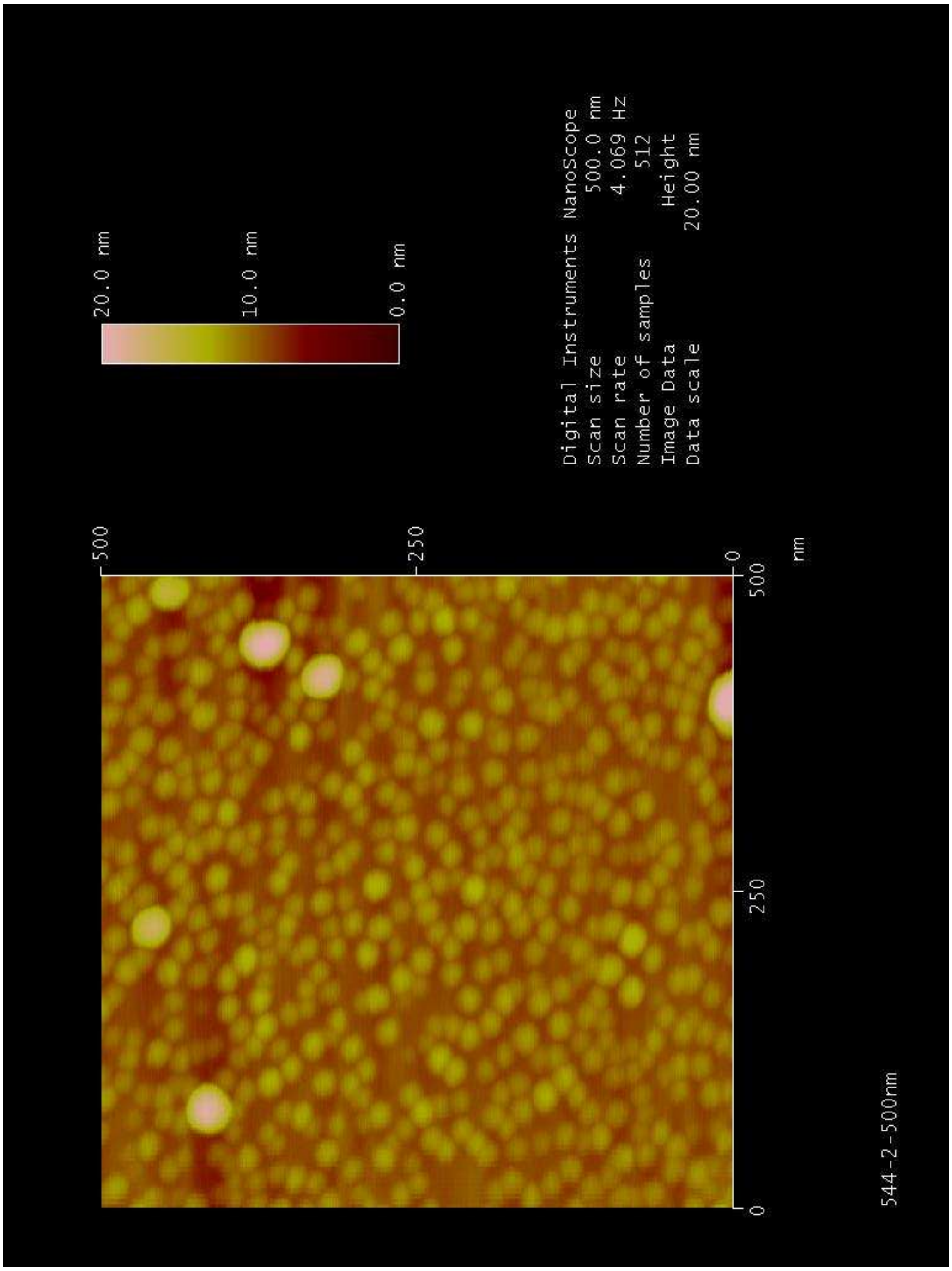

Digital Instruments NanoScope
Scan size 500.0 nm
Scan rate 4.069 Hz
Number of samples 512
Image Data Height
Data scale 20.00 nm

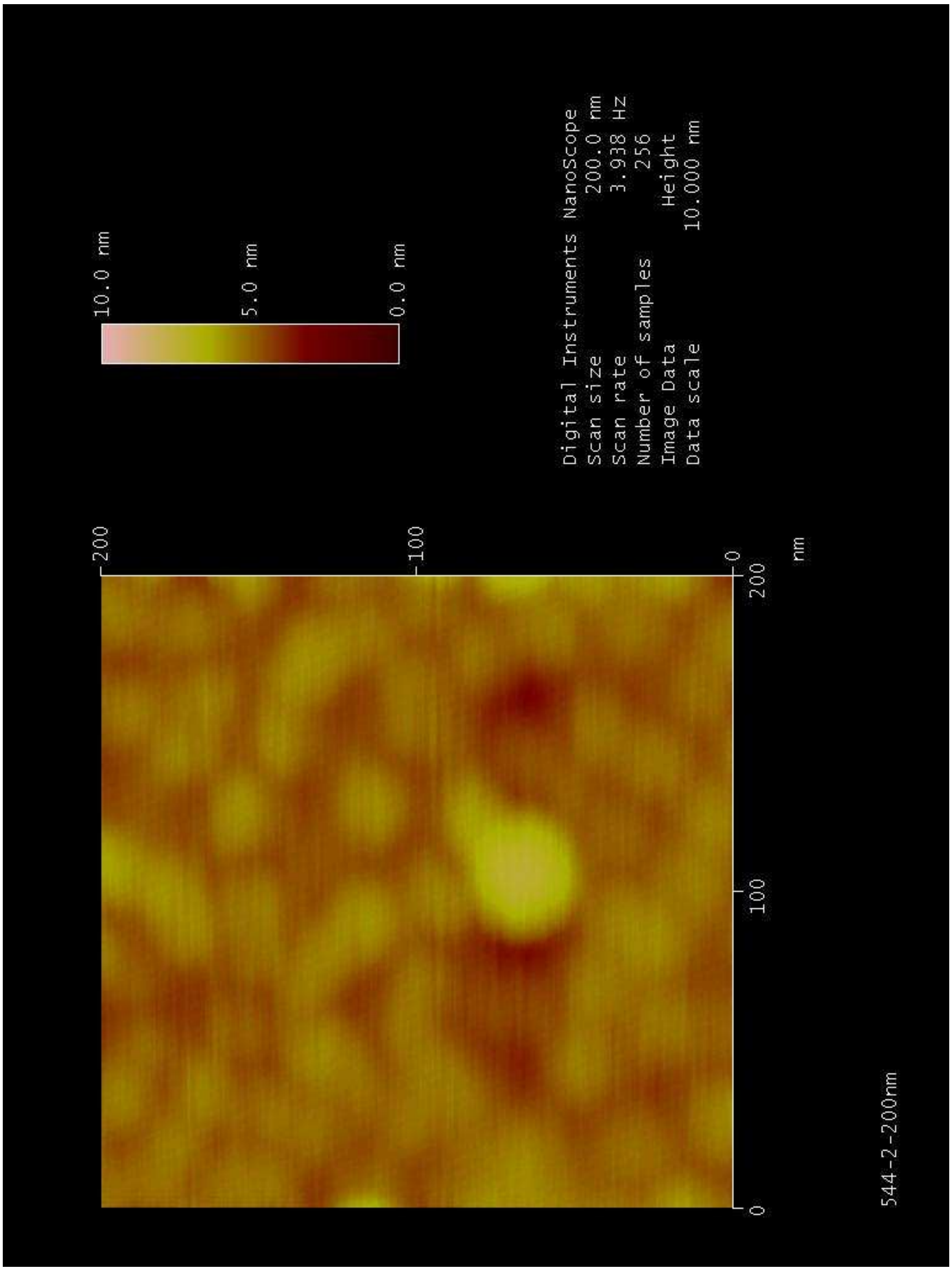
10.0 nm
5.0 nm
0.0 nm
Digital Instruments NanoScope
Scan size 200.0 nm
Scan rate 3.938 Hz
Number of samples 256
Image Data Height
Data scale 10.000 nm
200
100
0
nm
0
100
200
544-2-200nm

A.13 547-1

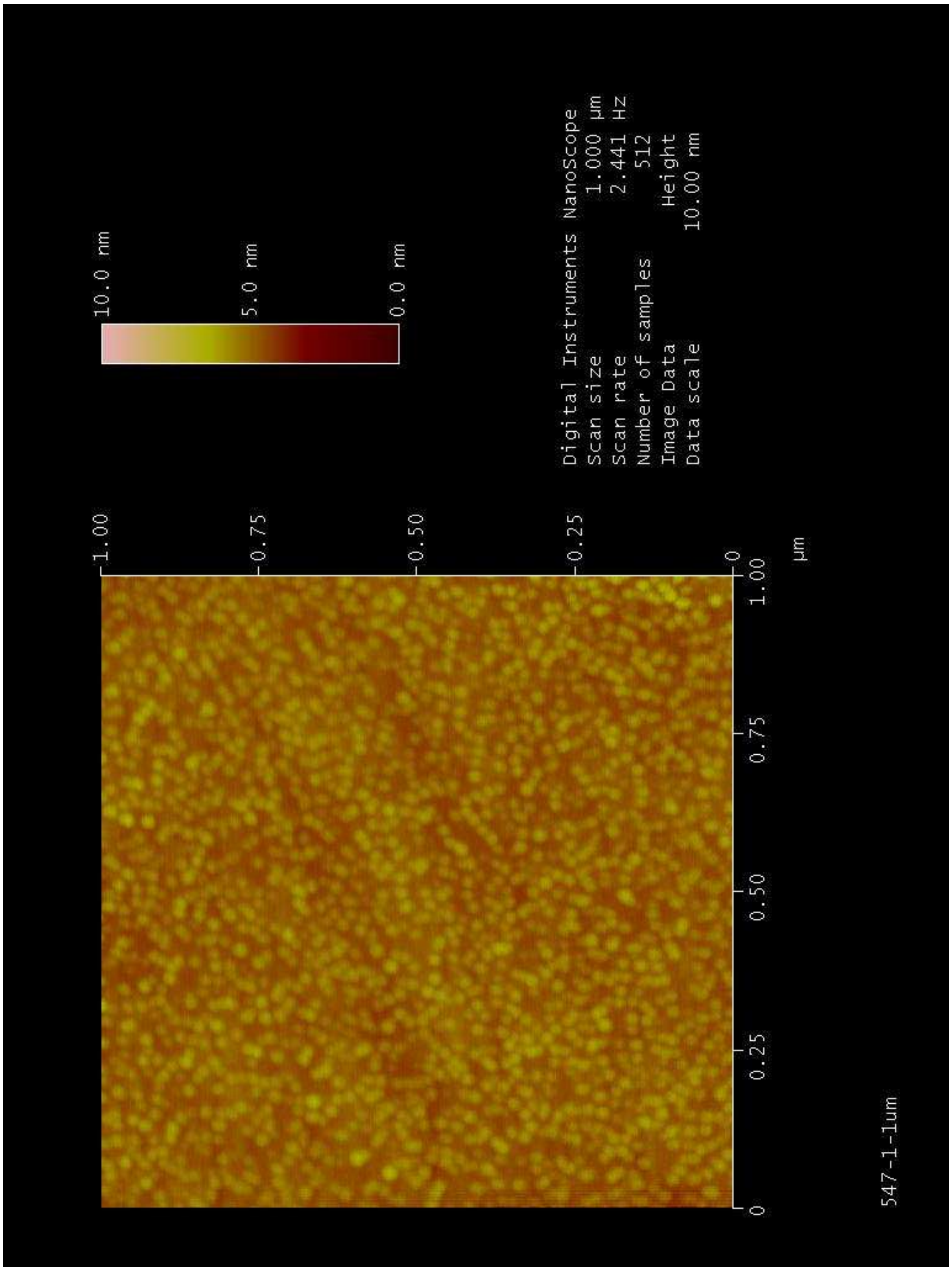
10.0 nm
5.0 nm
0.0 nm
Digital Instruments NanoScope
Scan size 1.000 µm
Scan rate 2.441 Hz
Number of samples 512
Image Data Height
Data scale 10.00 nm
1.00
0.75
0.50
0.25
0
µm
1.00
0.75
0.50
0.25
0
547-1-1um

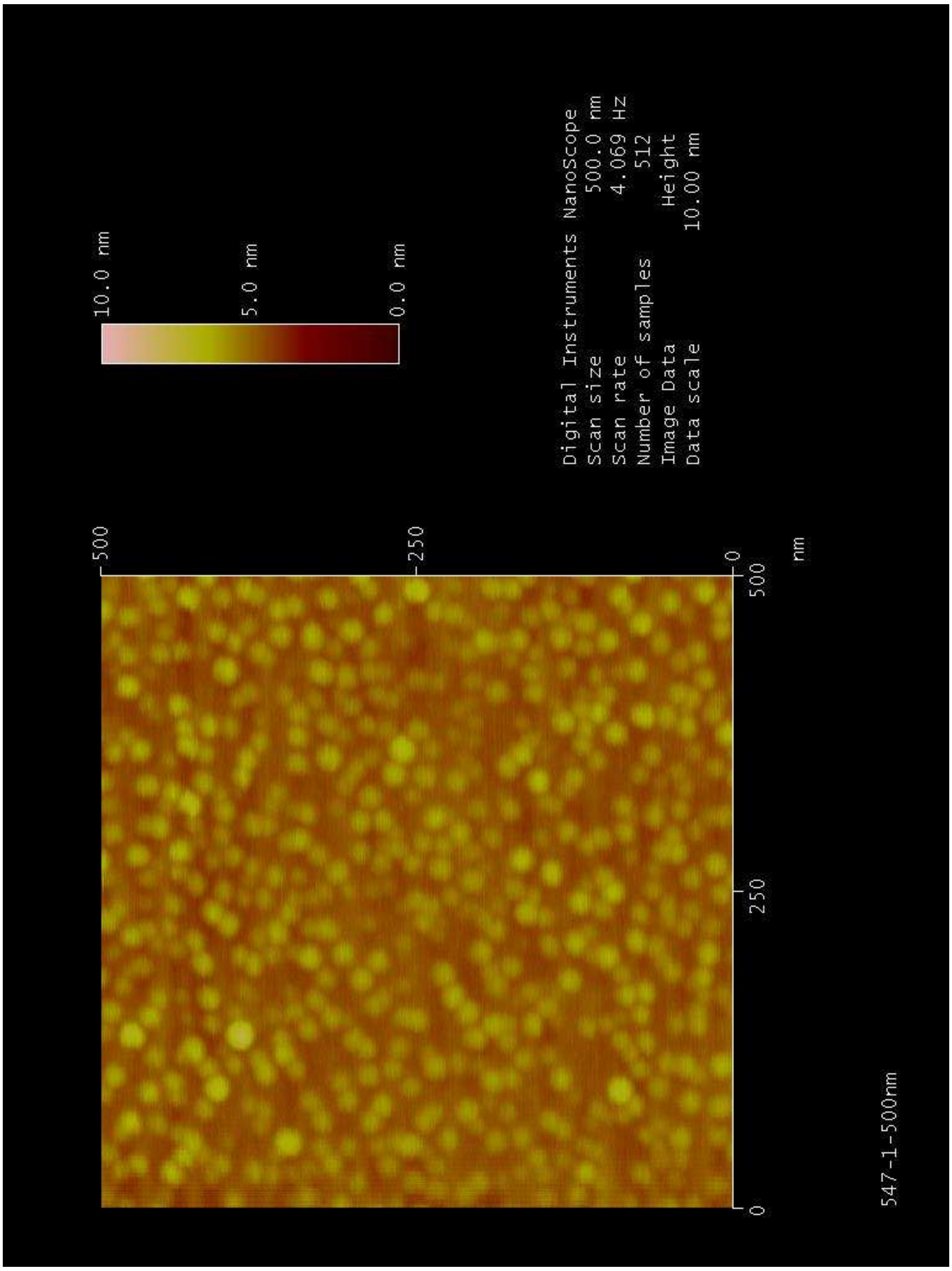
10.0 nm
5.0 nm
0.0 nm
Digital Instruments NanoScope
Scan size 500.0 nm
Scan rate 4.069 Hz
Number of samples 512
Image Data Height
Data scale 10.00 nm
500
250
0
nm
0
250
500
547-1-500nm

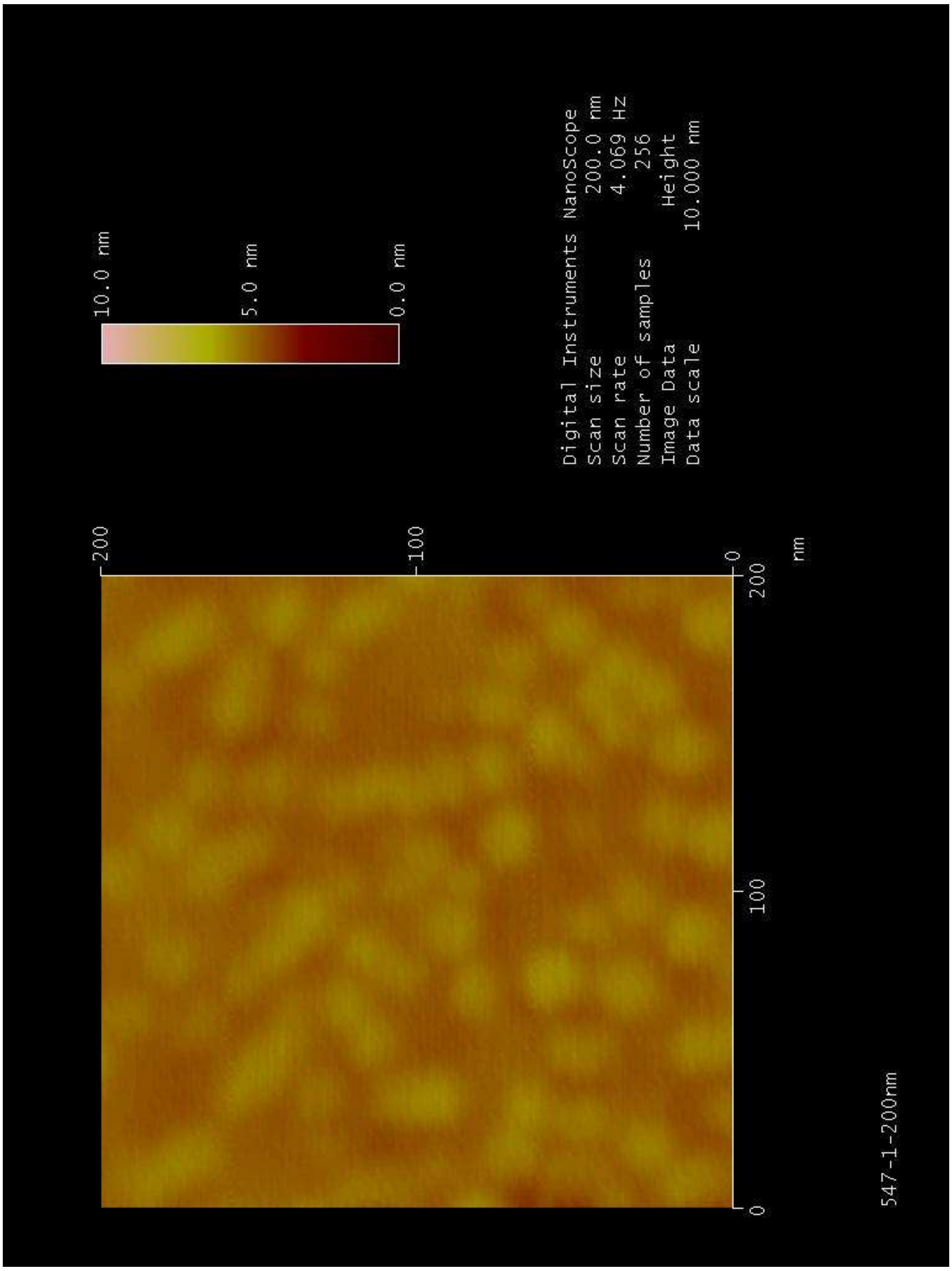
200
100
0
nm
0
100
200
547-1-200nm
10.0 nm
5.0 nm
0.0 nm
Digital Instruments NanoScope
Scan size 200.0 nm
Scan rate 4.069 Hz
Number of samples 256
Image Data Height
Data scale 10.000 nm

A.14 547-2

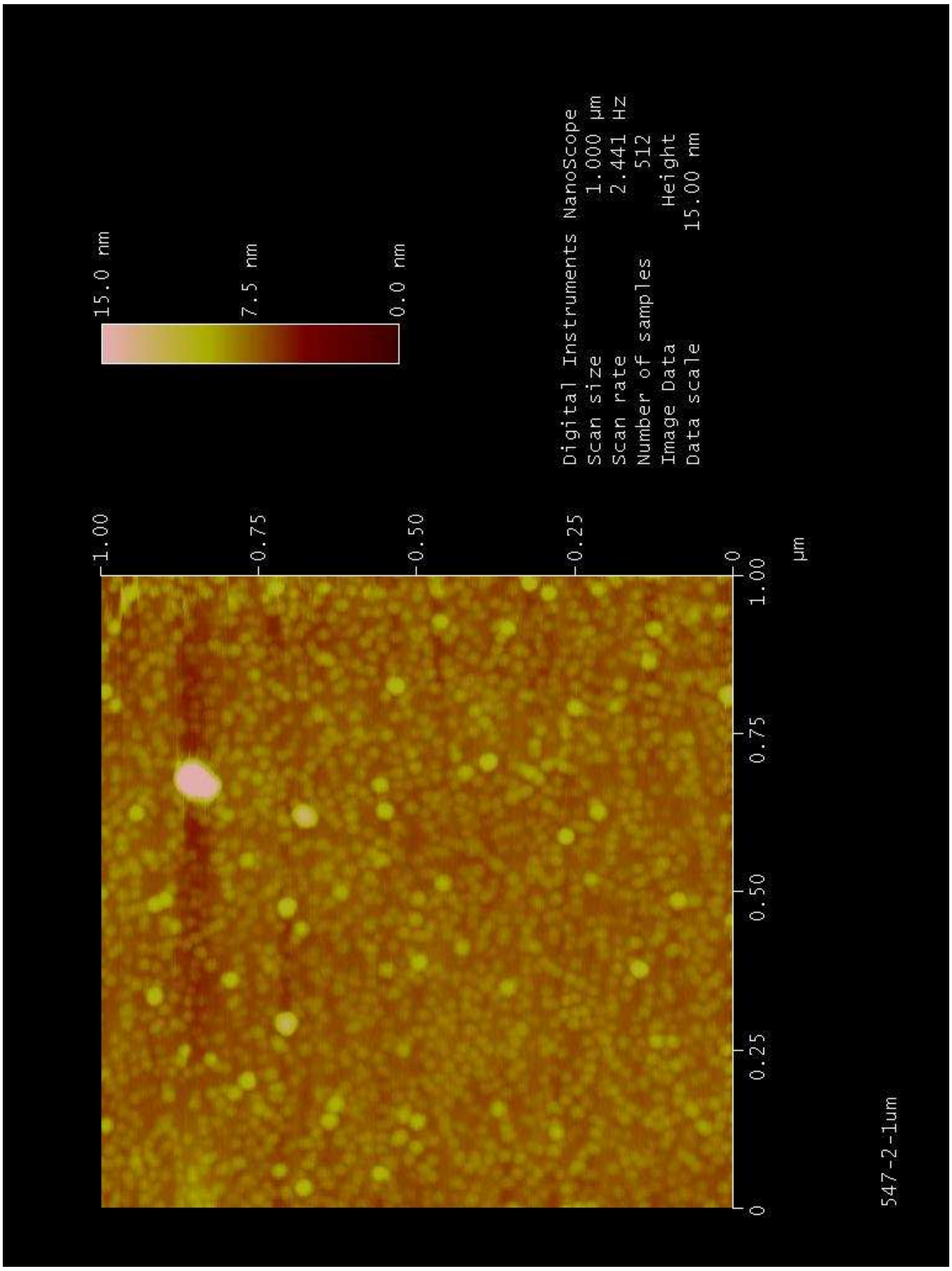
15.0 nm
7.5 nm
0.0 nm
1.00
0.75
0.50
0.25
0
µm
0
0.25
0.50
0.75
1.00
Digital Instruments NanoScope
Scan size 1.000 µm
Scan rate 2.441 Hz
Number of samples 512
Image Data Height
Data scale 15.00 nm
547-2-1um

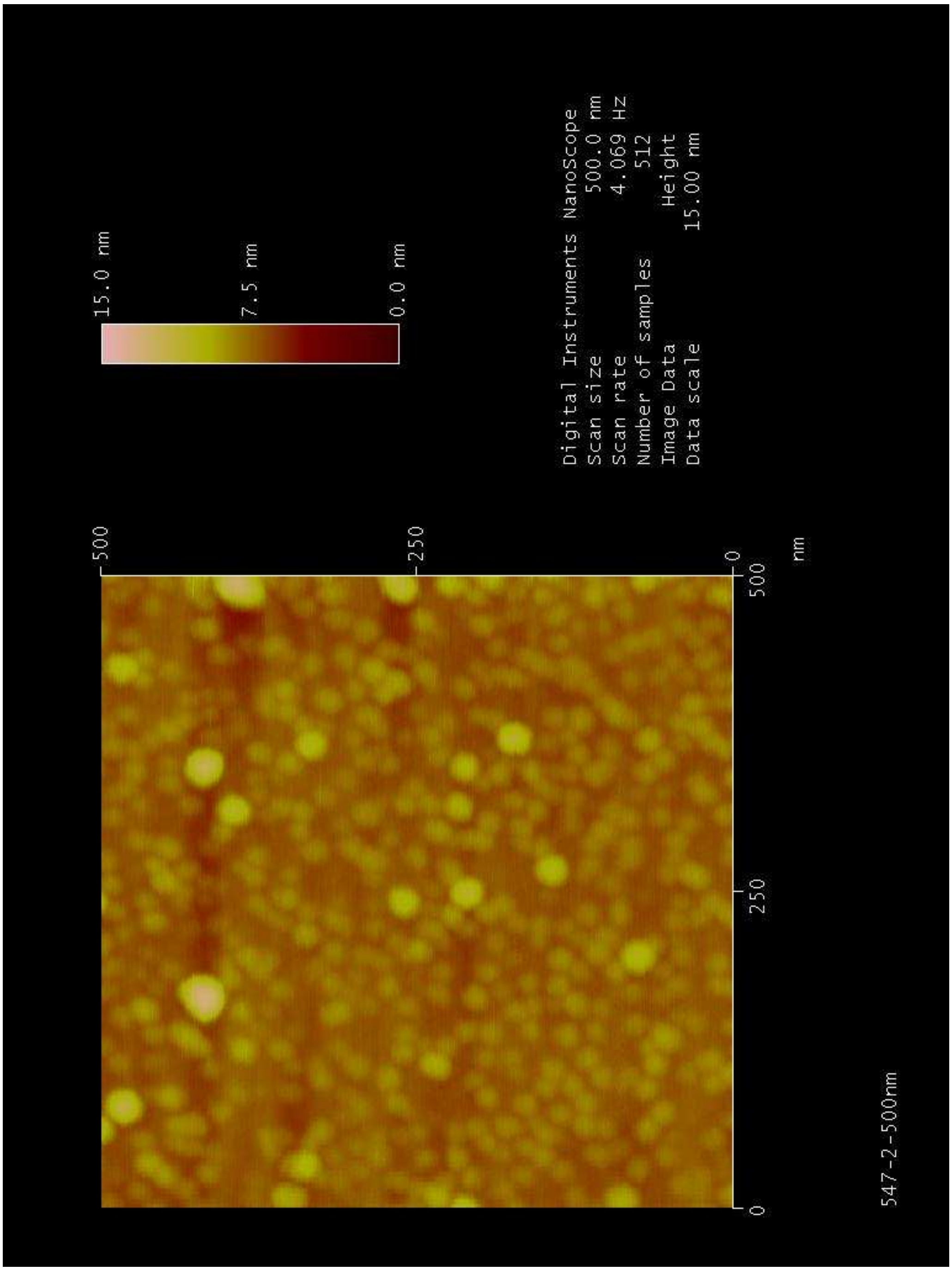
15.0 nm
7.5 nm
0.0 nm
Digital Instruments NanoScope
Scan size 500.0 nm
Scan rate 4.069 Hz
Number of samples 512
Image Data Height
Data scale 15.00 nm
500
250
0
nm
500
250
0
547-2-500nm

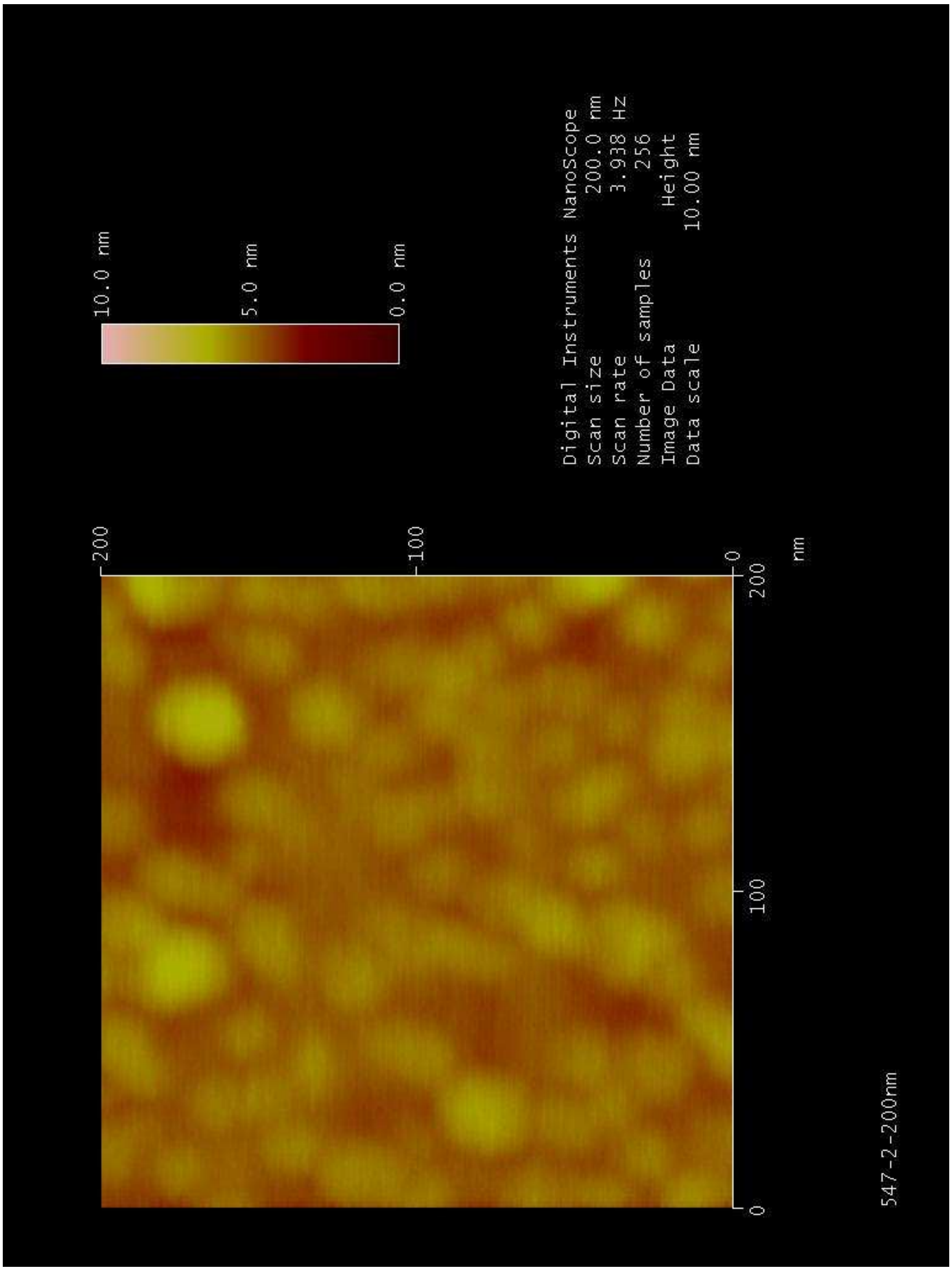

Digital Instruments NanoScope
Scan size 200.0 nm
Scan rate 3.938 Hz
Number of samples 256
Image Data Height
Data scale 10.00 nm

Appendix B

Matlab Codes

B.1 MATLAB code for diameter analysis

```
% LOAD RAW DATA

A=load('raw_data_imageA.txt');
B=load('raw_data_imageB.txt');
C=load('raw_data_imageC.txt');

x=5:0.5:60;




% CREATE THE HISTOGRAM OF DIAMETERS OF IMAGE A
% AND CALCULATE THE FITTING NORMAL DISTRIBUTION

diameter_nmA=2*10^(9)*A(:,3);
mu_diameter_A=mean(diameter_nmA);
sigma_diameter_A=std(diameter_nmA);

[bincounts_diameter_A,binpositions_diameter_A] = hist(diameter_nmA,x);
binwidth_diameter_A = binpositions_diameter_A(2) - binpositions_diameter_A(1);
histarea_diameter_A = binwidth_diameter_A*sum(bincounts_diameter_A);
x_diameter_A = binpositions_diameter_A(1):0.001:binpositions_diameter_A(end);
y_diameter_A = normpdf(x_diameter_A,mu_diameter_A,sigma_diameter_A);




% CREATE THE HISTOGRAM OF DIAMETERS OF IMAGE B
% AND CALCULATE THE FITTING NORMAL DISTRIBUTION

diameter_nmB=2*10^(9)*B(:,3);
mu_diameter_B=mean(diameter_nmB);
sigma_diameter_B=std(diameter_nmB);

[bincounts_diameter_B,binpositions_diameter_B] = hist(diameter_nmB,x);
```

```
binwidth_diameter_B = binpositions_diameter_B(2) - binpositions_diameter_B(1);
histarea_diameter_B = binwidth_diameter_B*sum(bincounts_diameter_B);
x_diameter_B = binpositions_diameter_B(1):0.001:binpositions_diameter_B(end);
y_diameter_B = normpdf(x_diameter_B,mu_diameter_B,sigma_diameter_B);




% PLOT THE HISTOGRAMS OF DIAMETERS OF IMAGE A AND B

subplot(2,2,1)
hist(diameter_nmA,x);
xlabel('Diameter [nm]');
ylabel('Counts [arb.un.]');

subplot(2,2,3)
hist(diameter_nmB,x);
xlabel('Diameter [nm]');
ylabel('Counts [arb.un.]');




% PLOT THE NORMAL DISTRIBUTION OF DIAMETERS OF IMAGE A AND B

subplot(2,2,[2 4])
plot(x_diameter_A,histarea_diameter_A*y_diameter_A,x_diameter_B,histarea_diameter_B*y_diameter_B);
xlabel('Diameter [nm]');
ylabel('Counts [arb.un.]');
title('Normal Distribution Fitting');
```

B.2 MATLAB code for height analysis

```
% LOAD RAW DATA

A=load('raw_data_imageA.txt');
B=load('raw_data_imageB.txt');


x=0:0.3:5;




% CREATE THE HISTOGRAM OF HEIGHTS OF IMAGE A
% AND CALCULATE THE FITTING NORMAL DISTRIBUTION

height_mA=A(:,2)-A(:,1);
height_nmA= 10^(9)*height_mA;
mu_height_A=mean(height_nmA);
sigma_height_A=std(height_nmA);

[bincounts_height_A,binpositions_height_A] = hist(height_nmA,x);
binwidth_height_A = binpositions_height_A(2) - binpositions_height_A(1);
histarea_height_A = binwidth_height_A*sum(bincounts_height_A);
x_height_A = binpositions_height_A(1):0.001:binpositions_height_A(end);
y_height_A = normpdf(x_height_A,mu_height_A,sigma_height_A);




% CREATE THE HISTOGRAM OF HEIGHTS OF IMAGE B
% AND CALCULATE THE FITTING NORMAL DISTRIBUTION

height_mB=B(:,2)-B(:,1);
height_nmB= 10^(9)*height_mB;
mu_height_B=mean(height_nmB);
sigma_height_B=std(height_nmB);

[bincounts_height_B,binpositions_height_B] = hist(height_nmB,x);
binwidth_height_B = binpositions_height_B(2) - binpositions_height_B(1);
histarea_height_B = binwidth_height_B*sum(bincounts_height_B);
x_height_B = binpositions_height_B(1):0.001:binpositions_height_B(end);
y_height_B = normpdf(x_height_B,mu_height_B,sigma_height_B);




% PLOT THE HISTOGRAMS OF HEIGHTS OF IMAGE A AND B

subplot(2,2,1)
hist(height_nmA,x);
xlabel('Height [nm]');
ylabel('Counts [arb.un.]');
```

```
subplot(2,2,3)
hist(height_nmB,x);
xlabel('Height [nm]');
ylabel('Counts [arb.un.]');



% PLOT THE NORMAL DISTRIBUTION OF HEIGHTS OF IMAGE A AND B
subplot(2,2,[2 4])
plot(x_height_A,histarea_height_A*y_height_A,x_height_B,histarea_height_B*y_height_B);
xlabel('Height [nm]');
ylabel('Counts [arb.un.]');
title('Normal Distribution Fitting');
```

B.3 MATLAB code for calculating QDs total volume in MLeq

```
% LOAD RAW DATA

A=load('raw_data_imageA.txt');
B=load('raw_data_imageB.txt');




% SUM OF QDs SINGLE VOLUMES AND CONVERSION IN MLeq FOR IMAGE A

A_sum_volume=sum(A);
ML_eq_A = (10^(27)*A_sum_volume(1,5))/(500^(2)*0.3);




% SUM OF QDs SINGLE VOLUMES AND CONVERSION IN MLeq FOR IMAGE B

B_sum_volume=sum(B);
ML_eq_B = (10^(27)*B_sum_volume(1,5))/(500^(2)*0.3);
```

Bibliography

[1] A. Martí and A. Luque, *Next Generation Photovoltaics, high efficiency through full spectrum utilization.* Institute of Physics, Bristol and Philadelphia, 2004.

[2] M. A. Green, "Photovoltaics: technology overview," *Energy Policy*, vol. 28, no. 14, pp. 989–998, 2000.

[3] ——, "Third generation photovoltaics: solar cells for 2020 and beyond," *Physica E*, vol. 14, pp. 65–70, 2002.

[4] D. M. Chapin, C. S. Fuller, and G. L. Pearson, "A new silicon p-n junction photocell for converting solar radiation into electrical power," *J. Appl. Phys.*, vol. 25, pp. 676–677, 1954.

[5] D. M. Bagnall and M. Boreland, "Photovoltaic technologies," *Energy Policy*, vol. 36, pp. 4390–4396, 2008.

[6] M. A. Green, "Recent developments in photovoltaics," *Solar Energy*, vol. 76, pp. 3–8, 2004.

[7] R. W. Miles, K. M. Hynes, and I. Forbes, "Photovoltaic solar cells: An overview of state-of-the-art cell development and environmental issues," *Progress in Crystal Growth and Characterization of Materials*, vol. 51, pp. 1–42, 2005.

[8] [Online]. Available: www.nrel.gov

[9] L. L. Kazmerski, "Solar photovoltaics r&d at the tipping point: A 2005 technology overview," *Journal of Electron Spectroscopy and Related Phenomena*, vol. 150, pp. 105–135, 2006.

[10] G. Conibeer, "Third-generation photovoltaics," *Materials Today*, vol. 10, pp. 42–50, 2007.

[11] M. A. Green, "Third generation photovoltaics: Ultra-high conversion efficiency at low cost," *Prog.Photovolt: Res. Appl.*, vol. 9, pp. 123–135, 2001.

[12] W. Shockley and H. J. Queisser, "Detailed balanced limit of efficiency of p-n junction solar cell," *J. Appl. Phys.*, vol. 32, pp. 510–519, 1961.

[13] A. Martí and G. L. Araújo, "Limiting efficiencies for photovoltaic energy conversion in multigap systems," *Solar Energy Materials and Solar Cells*, vol. 43, pp. 203–222, 1996.

[14] P. Würfel, "Solar energy conversion with hot electrons from impact ionisation," *Solar Energy Materials and Solar Cells*, vol. 46, pp. 43–52, 1997.

[15] A. Luque and A. Martí, "Increasing the efficiency of ideal solar cells by photon induced transition at intermediate levels," *Phys. Rev. Lett.*, vol. 78, pp. 5014–5017, 1997.

[16] A. Martí, N. López, E. Antolín, E. Cánovas, C. Stanley, C. Farmer, L. Cuadra, and A. Luque, "Novel semiconductor solar cell structure: The quantum dot intermediate band solar cell," *Thin Solid Films*, vol. 511-512, pp. 638–644, 2006.

[17] A. Martí, C. Stanley, and A. Luque, *Nanostructured Material for Solar Energy Conversion.* Elsevier, 2006, ch. 17.

[18] L. Cuadra, A. Luque, and A. Martí, "Present status of intermediate band solar cell research," *Thin Solid Films*, vol. 451-452, pp. 593–599, 2004.

[19] P. Harrison, *Quantum Wells, Wires and Dots: Theoretical and Computational Physics.* Wiley & Sons, 1999.

[20] S. Tomić, N. Harrison, and T. Jones, "Electronic structure of QD arrays: application to intermediate-band solar cells," *Opt. Quant. Electron.*, vol. 40, pp. 313–318, 2008.

[21] A. Martí, L. Cuadra, and A. Luque, "Design constraints of the quantum dot intermediate band solar cell," *Physica E*, vol. 14, pp. 150–157, 2002.

[22] M. Henini, *Handbook of Self Assembled Semiconductor Nanostructures for Novel Devices in Photonics and Electronics.* Elsevier, 2008, ch. 3.

[23] E. Placidi, F.Arciprete, M. Fanfoni, F. Patella, E. Orsini, and A. Balzarotti, "InAs/GaAs(001) epitaxy: kinetic effects in the two-dimensional to three-dimensional transition," *J. Phys.: Condens. Matter*, vol. 19, pp. 1–21, 2007.

[24] A. Cullis, D. Norris, T. Walther, M. Migliorato, and M. Hopkinson, "Stranski-krastanow transition and epitaxial island growth," *Phys. Rev. B*, vol. 66, 2002.

[25] P. Dowben and A. Miller, *Surface Segregation Phenomena.* CRC Press, 1990.

[26] G. Costantini, A. Rastelli, C. Manzano, P.Acosta-Diaz, R. Songmuang, G. Katsaros, O. Schmidt, and K. Kern, "Interplay between thermodynamics and kinetics of InAs/GaAs(001) quantum dots," *Phys. Rev. Lett.*, vol. 96, 2006.

[27] P. Joyce, T. Krzyzewski, G. Bell, and T. Jones, "Surface morphology evolution during the overgrowth of large InAs-GaAs quantum dots," *Appl. Phys. Lett.*, vol. 79, 2001.

[28] F. Ferdos, S. Wang, Y. Wei, A. Larsson, M. Sadeghi, and Q. Zhao, "Influence of a thin GaAs cap layer on structural and optical properties of InAs quantum dots," *Appl. Phys. Lett.*, vol. 81, 2002.

[29] H. Eisele, A. Lenz, R. Heitz, R. Timm, M. Dähne, Y. Temko, T. Suzuki, and K. Jacobi, "Change of InAs/GaAs quantum dot shape and composition during capping," *J. Appl. Phys.*, vol. 104, 2008.

[30] [Online]. Available: http://gwyddion.net/

[31] [Online]. Available: http://gwyddion.net/documentation/

[32] T. Passow, S. Li, P. Feinäugle, T. Vallaitis, J. Leuthold, D. Litvinov, D. Gerthsen, and M. Hetterich, "Systematic investigation into the influence of growth conditions on InAs/GaAs quantum dot properties," *J. Appl. Phys.*, vol. 102, 2007.

[33] D. Zhou, G. Sharma, S. F. Thomassen, T. W. Reenaas, and B. O. Fimland, "Optimization towards high density quantum dots for intermediate band solar cells grown by molecular beam epitaxy," *Appl. Phys. Lett.*, vol. 96, 2010.

[34] N. Cherkashin, M. Maksimov, A. Makarov, V. Shchukin, V. Ustinov, N. Lukovskaya, Y. Musikhin, G. Cirlin, N. Bert, Z. Alferov, N. Ledentsov, and D. Bimberg, "Control over the Parameters of InAs/GaAs Quantum Dot Arrays in the Stranski-Krastanow Growth Mode," *Semiconductors*, vol. 37, pp. 861–865, 2003.

[35] A. L. Barabási, "Self-assembled island formation in heteroepitaxial growth," *Appl. Phys. Lett.*, vol. 70, pp. 2565–2567, 1997.

[36] P. Joyce, T. Krzyzewski, G. Bell, T. Jones, S. Malik, D. Childs, and R. Murray, "Effect of growth rate on the size, composition, and optical properties of InAs/GaAs quantum dots grown by molecular-beam epitaxy," *Phys. Rev. B*, vol. 62, pp. 10 891–10 895, 2000.

[37] C. Chia, Y. Zhang, S. Wong, A. Yong, S. Chow, S. Chua, and J. Guo, "Saturated dot density of InAs/GaAs self-assembled quantum dots grown at high growth rate," *Appl. Phys. Lett.*, vol. 90, 2007.